

ABSTRACT

SHU, XU. Electronic Properties of Epitaxial Graphene: A First Principles Study. (Under the direction of Professor Marco Buongiorno Nardelli).

Since graphene was first isolated using adhesive tape in 2004, it has become a rising star of condensed matter physics, material science and attracted great attentions from physicists and material engineers due to its unique properties such as massless Dirac fermions, high electron mobility and anomalous quantum Hall effect. The Nobel Prize in Physics for 2010 was awarded to Andre Geim and Konstantin Novoselov "for groundbreaking experiments regarding the two-dimensional material graphene". This dissertation summaries my efforts on first-principles studies of the electronic properties of epitaxial graphene from five topics.

The first system investigated is the graphene on carbon face 6H-SiC substrate. By introducing dispersion forces into calculations, the electronic band structure shows n type doped graphene behavior which corrects previous neutral results in literature. Besides 6H-SiC which has been extensively studied, for the first time we have successfully simulated graphene on 3C-SiC(100) and Si(111)-7×7 substrates which are relatively new approaches of fabrication and have advantages on applications. Our results have confirmed the linear dispersion near Dirac point for both cases. As water is always present in the environment of graphene based electronic devices, the influences of water on epitaxial graphene are investigated, where Dirac point shift is observed. As last part of the dissertation, the phonons and Raman scattering of epitaxial graphene on silicon face 6H-SiC and freestanding graphene under uniaxial strain are discussed.

© Copyright 2012 by Shu Xu

All Rights Reserved

Electronic Properties of Epitaxial Graphene: A First Principles Study

by
Shu Xu

A dissertation submitted to the Graduate Faculty of
North Carolina State University
in partial fulfillment of the
requirements for the degree of
Doctor of Philosophy

Physics

Raleigh, North Carolina

2012

APPROVED BY:

Marco Buongiorno Nardelli
Committee Chair

Daniel Dougherty

Ki Wook Kim

Wenchang Lu

DEDICATION

To my paternal grandfather, paternal grandmother, maternal grandfather, maternal
grandmother, father and mother

BIOGRAPHY

EDUCATION

Doctor of Philosophy in Physics	North Carolina State University	2007 – 2012
Bachelor of Science in Physics	Nanjing University, China	2003 - 2007

ACKNOWLEDGMENTS

I would like to thank my advisor, Dr Marco Buogiorno Nardelli, for his guidance in my research. I would also like to thank my committee for their efforts and support.

There have been many people who cooperate with me or provide valuable help. Among them, Jeffery Mullen, Thushari Jayasekara, Sujata Paul, Frisco Rose, Liming Pan, Liping Yu, Dong Wu, Shuming Hu, Yifeng Chen, Rui Dong, Rui Mao, Byoung-Don Kong, Kostyantyn Borysenko, Jiuyang Wang, Shi Guo, Minyi Zhu, Ruoyi Qiu, Jie Jiang, Bikan Tan, Chengbo Han, Yan Li. Thanks so much for your time.

TABLE OF CONTENTS

LIST OF TABLES.....	vii
LIST OF FIGURES.....	viii
Chapter 1 Introduction	1
1.1 Density Functional Theory.....	1
1.1.1 Ab initio method.....	1
1.1.2 Basic Hamiltonian for many-body system	1
1.1.3 The Hohenberg-Kohn theorems	3
1.1.4 Kohn-Sham ansatz.....	5
1.1.5 LDA and GGA functional.....	6
1.1.6 Solving Kohn-Sham equations	7
1.1.7 Structural optimization	8
1.1.8 Phonon and Raman spectra.....	10
1.2 Fundamentals on graphene.....	11
1.2.1 Brief introduction of graphene	11
1.2.2 Graphene lattice.....	12
1.2.3 Band structure and Dirac point.....	14
1.2.4 Doping of graphene	14
1.2.5 Fabrication of graphene	15
Chapter 2 Electronic Properties of Graphene /6H-SiC(0001) interface: A First-principle Study	21
Chapter 3 Electronic Properties of Epitaxial Graphene on 3C-SiC(100) Substrate.....	28
3.1 Experiment background	28
3.2 Reciprocal lattice of graphene/3C-SiC(100).....	28
3.2.1 Graphene/3C-SiC(100) unit cell.....	29
3.3 Methodology	31
3.4 Graphene on unreconstructed 3C-SiC(100).....	33
3.4.1 First graphene layer A on C face 3C-SiC(100).....	33
3.4.2 First graphene layer A on Si face 3C-SiC(100)	34
3.4.3 Turbostratic AA' stacking graphene on C face 3C-SiC(100).....	35

3.4.4	Turbostratic AA' stacking graphene on Si face 3C-SiC(100).....	36
3.5	Graphene on reconstructed 3C-SiC(100)-c(2×2) surface	37
3.5.1	Monolayer graphene layer on the staggered dimer model 3C-SiC(100)-c(2×2)..	38
3.5.2	Monolayer graphene layer on the bridging dimer model 3C-SiC(100)-c(2×2)....	39
3.6	Summary	41
Chapter 4	Electronic Properties of Epitaxial Graphene on Silicon.....	56
4.1	Background	56
4.2	Atomic structure of reconstructed Si(111)-7×7 substrate	57
4.3	Methodology	59
4.4	Band structure of bare Si(111)-7×7 substrate.....	60
4.5	Atomic and band structure of monolayer graphene on Si(111)-7×7 substrate.....	60
4.6	Atomic and band structure of monolayer graphene on unreconstructed Si(111) surface	62
4.7	Origin of ripples on the graphene layer.....	63
4.8	Conclusion.....	64
Chapter 5	Water on Epitaxial Graphene.....	74
5.1	Background	74
5.2	Calculation details	75
5.3	Results and discussions	77
5.4	Conclusion.....	79
Chapter 6	Raman spectra in graphene.....	87
6.1	Raman spectra applications.....	87
6.2	Phonon dispersion of graphene	87
6.3	Raman scattering in graphene	88
6.4	Raman spectra of monolayer graphene under uniaxial strain	89
6.5	Methodology	91
6.6	Linear dependence of G shift with strain	93
6.7	Polarization dependence of G peak.....	94
6.8	Raman spectra of graphene on Si face SiC	94
6.9	Conclusion.....	95

LIST OF TABLES

Table 3.1 Geometries of turbostratic AA' stacking graphene on C face 3C-SiC(100).....	35
Table 3.2 Geometries of turbostratic AA' stacking graphene on Si face 3C-SiC(100).....	36
Table 3.3 C-C bond length of dimer in staggered dimer model 3C-SiC(100)-c(2×2).....	39
Table 3.4 C-C bond length of dimer in bridging dimer model 3C-SiC(100)-c(2×2).....	40
Table 4.1 Optimal geometries of different configurations of graphene on Si(111)-7×7.....	61
Table 4.2 Positions of Dirac point for different configurations of graphene on Si(111)-7×7.	62
Table 5.1 Optimal geometries for circumflex water on graphene/ Si face SiC	77
Table 5.2 Optimal geometries for O-down water on graphene/ Si face SiC.....	77
Table 5.3 Optimal geometries for circumflex water on graphene/ C face SiC	77
Table 5.4 Optimal geometries for O-down water on graphene/ C face SiC	77

LIST OF FIGURES

Figure 1.1 Interacting electrons in real potential	17
Figure 1.2 Non-interacting electrons in effective potential	17
Figure 1.3 Graphene lattice in real space.....	18
Figure 1.4 High symmetric points in Brillouin zone	18
Figure 1.5 Band structure of graphene along high symmetric K path	19
Figure 1.6 3D band structure of graphene and Dirac cone by A. H. Castro Neto	19
Figure 1.7 Dirac cones of n type doped, neutral and p type doped freestanding graphene (I. Gierz et al).....	20
Figure 3.1 LEED image of graphene on 3C-Si(100) (Queghi et al).....	43
Figure 3.2 Crystallographic axes of graphene/3C-SiC(100) determined from LEED (Queghi et al)	43
Figure 3.3 STM topographic image of the graphene layer on cubic SiC substrate	44
Figure 3.4 3C-SiC(100) crystal structure.....	44
Figure 3.5 Schematic diagram of graphene layer on 3C-SiC(100) surface	45
Figure 3.6 Square graphene cell under strain.....	45
Figure 3.7 BZ of graphene supercell on 3C-SiC.....	46
Figure 3.8 Optimized structure of first layer graphene on C face 3C-SiC(100).....	46
Figure 3.9 Band structure of first layer graphene on C face 3C-SiC(100)	47
Figure 3.10 Optimized structure of first layer graphene on Si face 3C-SiC(100)	47
Figure 3.11 Band structure of first layer graphene on Si face 3C-SiC(100).....	48
Figure 3.12 Optimized structure of turbostratic AA' stacking graphene on C face 3C-SiC(100)	48
Figure 3.13 Band structure of turbostratic AA' stacking graphene on C face 3C-SiC(100)...	49
Figure 3.14 Optimized structure of turbostratic AA' stacking graphene on Si face 3C-SiC(100)	49
Figure 3.15 Band structure of turbostratic AA' stacking graphene on Si face 3C-SiC(100) ..	50
Figure 3.16 Surface structure of staggered dimer model 3C-SiC(100)-c(2×2) (J. M. Powers et al in 1991)	51

Figure 3.17 Optimized structure of monolayer graphene on staggered dimer model 3C-SiC(100)-c(2×2).....	51
Figure 3.18 Band structure of monolayer graphene on staggered dimer model 3C-SiC(100)-c(2×2).....	52
Figure 3.19 Surface structure of bridging dimer model 3C-SiC(100)-c(2×2) produced by C ₂ H ₄ exposure (J. M. Powers et al in 1991).....	53
Figure 3.20 Surface structure of bridging dimer model 3C-SiC(100)-c(2×2) produced by Si sublimation (J. M. Powers et al in 1991).....	54
Figure 3.21 Optimized structure of monolayer graphene on bridging dimer model 3C-SiC(100)-c(2×2).....	54
Figure 3.22 Band structure of monolayer graphene on bridging dimer model 3C-SiC(100)-c(2×2).....	55
Figure 4.1 RHEED images acquired along the <110> crystal direction.....	66
Figure 4.2 Crystal structure of Si(111)-7×7 in dimmer-adatom-stacking-fault (DAS) model (Takayanagi et al).....	67
Figure 4.3 Unit cell of Si(111)-7×7 reconstruction in dimmer-adatom-stacking-fault (DAS) model.....	67
Figure 4.4 Three configurations of graphene on Si(111)-7×7 unit cell	68
Figure 4.5 Surface band structure along the G-Q, Q-P, and P-G directions of the two-dimensional BZ (Jose Ortega et al.)	68
Figure 4.6 Surface band structure bare Si(111)-7×7 surface	69
Figure 4.7 Optimal structures of graphene on Si(111)-7×7	70
Figure 4.8 Band structures of graphene on Si(111)-7×7.....	71
Figure 4.9 Optimal structures of graphene on unreconstructed Si(111).....	72
Figure 4.10 Band structures of graphene on unreconstructed Si(111).....	73
Figure 5.1 Crystal structure of water on freestanding graphene.....	80
Figure 5.2 Band structure of water on freestanding graphene near Dirac point.....	81
Figure 5.3 Five water orientations and three sites	81
Figure 5.4 Equilibrium intermolecular separation R_e and energy for different water on	

graphene configurations.....	82
Figure 5.5 Two configurations of water on graphene	82
Figure 5.6 Atomic structure, band structure and charge difference for circumflex water on graphene/ Si face SiC.....	83
Figure 5.7 Atomic structure, band structure and charge difference for O-down water on graphene/ Si face SiC.....	84
Figure 5.8 Atomic structure, band structure and charge difference for circumflex water on graphene/ C face SiC	85
Figure 5.9 Atomic structure, band structure and charge difference for O-down water on graphene/ C face SiC	86
Figure 6.1 Phonon dispersion of monolayer freestanding graphene.....	97
Figure 6.2 Raman spectrum of a graphene edge, showing main Raman features, the D, G and G' bands taken with a laser excitation energy of 2.41 eV.....	98
Figure 6.3 G peak as a function of uniaxial strain	99
Figure 6.4 Positions of G^+ and G^- in experiment	100
Figure 6.5 Directions of incident scattered light and strain	100
Figure 6.6 G peak as a function of uniaxial strain for monolayer freestanding graphene	101
Figure 6.7 Positions of G^+ and G^- and linear fitting	102
Figure 6.8 Polarization dependence of G peak in experiment	103
Figure 6.9 Polarization dependence of G peak from first-principles calculation	104
Figure 6.10 Raman spectrum of graphene on Si face 6H-SiC.....	105

Chapter 1 Introduction

1.1 Density Functional Theory

1.1.1 Ab initio method

In this dissertation, all the physics problems have been investigated using ab initio methods. Ab initio means a method from the basic laws of nature without assumptions of particular model. It calculates materials properties from first principles, solving the fundamental quantum mechanical Schrödinger equation numerically without additional experiment input. It has the advantages of obtaining the exact properties of materials when all the assumptions are sufficiently small. However, due to its high computational cost, we have to build the atomic system as small as possible, up to hundreds of atoms. With the fast growing computer technology, first principles calculations of large system may be possible in the future.

1.1.2 Basic Hamiltonian for many-body system

Density functional theory, first developed in 1960s, is one of the most advanced quantum mechanical modeling method. It is an ab initio method as it describes the electronic

ground state by solving the Schrödinger equation. From microscopic point of view, the matter we investigate is made of numerous nuclei and electrons. It therefore can be described by the fundamental Hamiltonian as in Eq(1.1) for the many-body system of nuclei($\{ R_l \}$) and electrons ($\{ r_i \}$).

$$\hat{H} = -\frac{\hbar^2}{2m_e} \sum_i \nabla_i^2 - \sum_{i,l} \frac{Z_l e^2}{|\mathbf{r}_i - \mathbf{R}_l|} + \frac{1}{2} \sum_{i \neq j} \frac{e^2}{|\mathbf{r}_i - \mathbf{r}_j|} - \sum_l \frac{\hbar^2}{2M_l} \nabla_l^2 + \frac{1}{2} \sum_{l \neq j} \frac{Z_l Z_j e^2}{|\mathbf{R}_l - \mathbf{R}_j|} \quad (1.1)$$

The 1st term is the kinetic energy of the electrons. The 2nd term represents the Coulomb interactions between electrons and nuclei. The 3rd term is the electron-electron interactions. The 4th is the nuclear kinetic energy. Because of the small electron-proton mass ratio $\frac{m_e}{m_p} \approx 5.45 \times 10^{-4}$, this term can be neglected as an excellent approximation for many purposes. It is defined as Born-Oppenheimer or adiabatic approximation¹. The last term is the nuclei-nuclei interactions. This Hamiltonian is theoretically exact but practically impossible to solve mainly because of the complexity of the electron-electron interactions. Time dependent Schrödinger equation in Eq(1.2) is the fundamental law which governs the quantum system.

$$i\hbar \frac{\partial \psi(\{\mathbf{r}_i\}; t)}{\partial t} = \hat{H} \psi(\{\mathbf{r}_i\}; t) \quad (1.2)$$

where $\psi(\{\mathbf{r}_i\}; t)$ is the wavefunction of the many-body system, which determines all the

physical observables. By taking the expectation value of density operator

$$\hat{n}(\mathbf{r}) = \sum_{i=1,N} \delta(\mathbf{r} - \mathbf{r}_i) \quad (1.3)$$

we get the density of particles

$$n(\mathbf{r}) = \frac{\langle \psi | \hat{n}(\mathbf{r}) | \psi \rangle}{\langle \psi | \psi \rangle} \quad (1.4)$$

1.1.3 The Hohenberg-Kohn theorems

The fundamental tenet of density functional theory is that the density of ground state of the many-body system $n_0(\mathbf{r})$ can be viewed as the basic variable. All the information in the wavefunction can be expressed as a unique functional of $n_0(\mathbf{r})$, therefore determining the properties of the whole system².

The Hamiltonian of many-body system in Eq(1.1) can be simplified as

$$\hat{H} = -\frac{1}{2} \sum_i \nabla_i^2 + \sum_i V_{ext}(\mathbf{r}_i) + \frac{1}{2} \sum_{i \neq j} \frac{e^2}{|\mathbf{r}_i - \mathbf{r}_j|} \quad (1.5)$$

where, under the B-O approximation, positions of nuclei can be considered as fixed. The external potential $V_{ext}(\mathbf{r})$ replaces the interactions of nuclei acting on electrons and the nuclei and nuclei-nuclei interactions are ignored because it is irrelevant. Here we adopt

Hartree atomic units $\hbar = m_e = e = \frac{4\pi}{\epsilon_0} = 1$

Hohenberg and Kohn formulated density functional theory as an exact theory of many-body system by giving two theorems:

Theorem I: For any system of interacting particles in an external potential $V_{ext}(\mathbf{r})$, the potential $V_{ext}(\mathbf{r})$ is determined uniquely, by the ground state particle density $n_0(\mathbf{r})$, except for a constant.

Theorem II: A universal functional for the energy $E[n]$ in terms of the density $n(\mathbf{r})$ can be defined, valid for any external potential $V_{ext}(\mathbf{r})$. For any particular $V_{ext}(\mathbf{r})$, the exact ground state energy of the system is the global minimum value of this functional, and the density $n(\mathbf{r})$ that minimizes the functional is the exact ground state density $n_0(\mathbf{r})$.

In other words, there is one - to - one correspondence between the global minimum value of energy $E_{min}[n]$ and the ground state density $n_0(\mathbf{r})$. The process of minimizing the functional $E[n]$ is to find the ground state density $n_0(\mathbf{r})$. The Hohenberg-Kohn theorem provides a revolutionary approach to formulate DFT as an exact theory of many-body system. However, because the functional is very complicated and non-analytic except for the simple cases such as single hydrogen atom, Hohenberg-Kohn theorem still does not provide useful and practical solutions.

1.1.4 Kohn-Sham ansatz

The Hamiltonian in Eq(1.5) describes the system of many interacting electrons in the real potential of nuclei as in Figure (1.1). The corresponding Schrödinger equation could not be solved because of the complexity of interacting effect. Instead of solving the interacting system problem directly, in 1965 Kohn and Sham proposed a new approach which replaced the original problem³. This is called Kohn-Sham ansatz, which converts the problem into another problem involving non-interacting electrons in an effect potential as in Figure (1.2). The ansatz is based on the assumption that the exact ground state density of the original interacting system can be represented by the same density of the auxiliary system of non-interacting electrons, called “non – interacting – V - representability”.

The effective Hamiltonian is

$$\hat{H}_{KS}^{\sigma} = -\frac{1}{2}\nabla^2 + V_{KS}^{\sigma}(\mathbf{r}) \quad (1.6)$$

where the effective potential

$$V_{KS}^{\sigma}(\mathbf{r}) = V_{ext}(\mathbf{r}) + V_{Hartree}(\mathbf{r}) + V_{xc}^{\sigma}(\mathbf{r}) \quad (1.7)$$

In Eq(1.7) $V_{ext}(\mathbf{r})$ is the external potential due to nuclei, $V_{Hartree}(\mathbf{r})$ is defined as the classical Coulomb interaction potential of the electron interacting with itself, and $V_{xc}^{\sigma}(\mathbf{r})$ is the exchange-correlation potential due to the difficult effects of many-body system.

This corresponds to the exchange-correlation functional $E_{xc}[n]$.

1.1.5 LDA and GGA functional

The advantage of recasting Hohenberg-Kohn functional in Kohn-Sham form is that by separating the non-interacting electron kinetic energy and long range classical Coulomb energy, $E_{xc}[n]$ remained can be approximated as a local or nearly local functional of electron density.

Local Density Approximation (LDA) is the most fundamental form of exchange-correlation functional. In LDA, $E_{xc}[n]$ is calculated as an integral over all space with exchange-correlation energy density the same as homogeneous electron gas at each point because solid can be viewed as close to the limit of homogeneous gas and the exchange-correlation is essentially local. Generalized-gradient approximation (GGA) functional is an improvement over LDA which depends both on the magnitude of electron density $n(\mathbf{r})$ and the gradient of the density $|\nabla n(\mathbf{r})|$.

1.1.6 Solving Kohn-Sham equations

The Kohn-Sham equation combined with LDA exchange-correlation functional provides a framework for solving the exact density and energy of ground state. A set of Schrödinger-like equations in Eq(1.8) must be solved subject to the condition that the electron density $n(\mathbf{r})$ and Kohn-Sham potential $V_{KS}^\sigma(\mathbf{r})$ are consistent.

$$\left[-\frac{1}{2}\nabla^2 + V_{KS}^\sigma(\mathbf{r}) \right] \psi_i^\sigma(\mathbf{r}) = \epsilon_i^\sigma \psi_i^\sigma(\mathbf{r}) \quad (1.8)$$

$$n(r) = \sum_s \sum_{i=1,N} |\Psi_i^s(\mathbf{r})|^2 \quad (1.9)$$

The numerical solution involves a self-consistent process. The flow is this:

Given an initial trial potential V_i , we solve the Schrödinger-like Eq(1.8) and apply Eq(1.9) to get the electron density n_i . By plugging it back to Eq(1.7) with specific LDA functional, we get V_{i+1} . Iteratively we have n_{i+1} . Then we compare the difference between n_i and n_{i+1} with a preset threshold and decide if it is converged or not. If not, more steps of iterations are needed until convergence has achieved.

The actual computation is implemented by the pw.x code in Quantum ESPRESSO⁵.

After Kohn-Sham equations are solved, we get a basis of plain waves for the ground state.

Using the basis, other properties of the system such as energies, forces and stresses can be achieved.

1.1.7 Structural optimization

The purpose of structural optimization is to obtain the relaxed geometric structure in ground state. The values of lattice constant and positions of atoms in the lattice basis given in textbook, literature and experiment are not necessarily stable in the practical computational environment due to the different approximations of exchange-correlation functional used. Therefore prior to performing the electronic properties calculation, an accurate structural optimization is always crucial. The optimization process involves both determining the equilibrium lattice constant and the positions of atoms relative to the crystal basis. The energy of the crystal structure as a function of lattice constant is the most fundamental properties of condensed matter. Near the equilibrium lattice constant, the function can be fitted by a parabola. The lattice constant which minimizes the total energy locally determines the equilibrium structure which is most stable and has zero pressure on the lattice. In some cases, to simulate the system in experiment, the lattice

constant should match experimental data as the strain may exist in the system. For example, in Chapter 2, the graphene cell is stretched out under an 8% strain in experiment.

The accurate calculation of relaxed position for each atom in the unit cell is also important as it determines the characteristics of bonding between nuclei. This essentially involves force calculations. Within the Born-Oppenheimer approximation that the moving of nuclei can be ignored when calculating electron density, the Hellmann-Feynman theorem⁶ gives the expression of force

$$\mathbf{F}_I = -\frac{\partial E}{\partial \mathbf{R}_I} = -\int d\mathbf{r} \cdot n(\mathbf{r}) \frac{\partial V_{ext}(\mathbf{r})}{\partial \mathbf{R}_I} - \frac{\partial E_{II}}{\partial \mathbf{R}_I} \quad (1.10)$$

The force is a function of only electron density.

For an initial configuration, a self-consistent single-point calculation is performed and the forces acting on each atom in three directions are obtained. If these forces are greater than the minimum tolerance, the atoms are moved in the direction of the forces. This procedure is repeated until a relaxed structure, with vanishing forces (within the numerical tolerance) is achieved.

1.1.8 Phonon and Raman spectra

Phonon is a quantum of vibrational energy in a crystal lattice or solid. The solution for all the vibrational states is the set of independent oscillators described by the classic Hessian in Eq(1.11)

$$\det \left| \frac{1}{\sqrt{M_I M_J}} \frac{\partial^2 E(\mathbf{R})}{\partial \mathbf{R}_I \partial \mathbf{R}_J} - \omega^2 \right| = 0 \quad (1.11)$$

The partial derivative term can be converted into the second derivative of the energy with respect to the amplitude of a lattice distortion of definite wave vector by Fourier transform. By applying density functional perturbation theory, the derivatives of energy can be expressed as density linear response function and therefore directly solved⁷. The phonon dispersion curve can be also obtained by solving phonon frequency in each q point.

Raman spectroscopy is a spectroscopic technique used to study vibrational modes in the crystal. The incident laser light interacts with the phonon and is scattered, resulting in the energy of the laser photons being shifted up or down. The frequency shift gives information of phonons. The first order Raman scattering has the same frequency of phonons. Its intensity can be computed directly from the results of DFT calculations.

Within the Placzek approximation⁸, Raman intensity has the expression

$$I^{\nu} \propto \left| \mathbf{e}_i \cdot \overleftrightarrow{\mathbf{A}}^{\nu} \cdot \mathbf{e}_s \right|^2 \frac{1}{\omega_{\nu}} (n_{\nu} + 1) \quad (1.12)$$

where \mathbf{e}_i \mathbf{e}_s are the polarization vectors of incident and scattered light, respectively.

$$n_{\nu} = [\exp(\hbar\omega_{\nu} / k_B T) - 1]^{-1} \quad (1.13)$$

$$A_{lm}^{\nu} = \sum_{k\gamma} \frac{\partial^3 \epsilon^{el}}{\partial E_l \partial E_m \partial u_{k\gamma}} \frac{w_{k\gamma}^{\nu}}{\sqrt{M_{\gamma}}} \quad (1.14)$$

A_{lm}^{ν} is the Raman tensor which can be achieved by linear response calculation as it contains finite derivative of energy term. Using the strategy provides by Michele Lazzeri and Francesco Mauri⁹, the Raman spectra of intensity vs. frequency can be obtained by a phonon calculation by quantum ESPRESSO followed by the post processing code.

1.2 Fundamentals on graphene

1.2.1 Brief introduction of graphene

Graphene, essentially a single atomic layer of graphite, has become a rising star of condensed matter physics, material science and attracted great attentions from scientists

and engineers since it was first isolated in 2004. The Nobel Prize in Physics for 2010 was awarded to Andre Geim and Konstantin Novoselov at the University of Manchester "for groundbreaking experiments regarding the two-dimensional material graphene". Although it just became available for experimental inspection in recent years, the charming properties of graphene have been an object of theoretical physicists since 1946 when P. R. Wallace first calculated its unique band structure¹⁰. In fact the pencil debris contains flakes of graphite among which individual graphene layers could exist because the stacks of graphene layers are weakly coupled by van der Waals forces. However, scientists did not expect the existence of graphene in free state as Landau and Peierls argued the 2D crystal were thermodynamically unstable until Andre Geim's group isolated individual graphene planes by Scotch tape in 2004. Therefore graphene is relatively easy to make but difficult to find. Graphene has extraordinary and unique properties such as massless Dirac fermions, high electron mobility and anomalous quantum Hall effect as compared to its counterpart in semiconductor.

1.2.2 Graphene lattice

Graphene is a one-atom-thick two-dimensional (2D) honeycomb sheet made out of carbon atoms arranged in hexagonal structure. It consists of two interpenetrating

triangular sublattices. Thus the primitive cell has two carbon atoms, designated A and B in Figure 1.1. In the graphene plane, each carbon atom forms strong σ bond with three nearest neighbors with angles of 120° . The C-C bond length is around 1.42 \AA . As a result of sp^2 hybridization, σ bond is formed by valence electrons of $2s$, $2p_x$, $2p_y$ orbitals. The half-filled $2p_z$ orbital perpendicular to the graphene plane forms a weak π bond with other $2p_z$ orbital.

The vectors of primitive cell are

$$\mathbf{a}_1 = a\hat{x} \quad (1.15)$$

$$\mathbf{a}_2 = -\frac{1}{2}a\hat{x} + \frac{\sqrt{3}}{2}a\hat{y} \quad (1.16)$$

with an angle of 120° in-between.

To apply Fourier transform equations in Eq(1.18) and Eq(1.19), here we play a trick by inducing a virtual vector of unit length in the third dimension

$$\mathbf{a}_1 = a\hat{z} \quad (1.17)$$

$$\mathbf{b}_1 = 2\pi \frac{\mathbf{a}_2 \times \mathbf{a}_3}{\mathbf{a}_1 \cdot \mathbf{a}_2 \times \mathbf{a}_3} \quad (1.18)$$

$$\mathbf{b}_2 = 2\pi \frac{\mathbf{a}_3 \times \mathbf{a}_1}{\mathbf{a}_1 \cdot \mathbf{a}_2 \times \mathbf{a}_3} \quad (1.19)$$

We get the primitive vectors in reciprocal lattice.

$$\mathbf{b}_1 = \frac{2\pi}{3a} \hat{\mathbf{x}} + \frac{2\sqrt{3}\pi}{3a} \hat{\mathbf{y}} \quad (1.20)$$

$$\mathbf{b}_2 = \frac{4\pi}{3a} \hat{\mathbf{x}} \quad (1.21)$$

with an angle of 60° in-between.

The Brillion zone is also a hexagon due to symmetry as plotted in Figure 1.4.

1.2.3 Band structure and Dirac point

Figure 1.5 shows the electronic band structure of neutral graphene calculated by DFT. At K point, the corner of BZ, the fully occupied valence π band and the fully empty conduction π^* touch each other with zero band gap. The Fermi level, often referred as zero energy, comes through the band crossing. K is called Dirac point or Dirac cone in 3D band structure as plotted by A. H. Castro Neto¹¹ in Figure 1.6. Around the Dirac point, the energy E has linear relation with k. The linear dispersion relation near Dirac point is one of the most distinguished electronic properties of graphene.

1.2.4 Doping of graphene

In the ideal situation, the graphene is neutral. The valence π band is completely filled with valence electrons while the conduction π^* band is completely empty. The Dirac point

falls exactly on the Fermi level as in Figure 1.7b. In Figure 1.7a case, if the substrate or adsorbent donates electrons to graphene layer, the π^* band is partially filled; therefore the Fermi level comes across the conduction band. This makes graphene n type doped. In Figure 1.7c, graphene is p type doped. If electron charges transfer from graphene layer to the substrate or adsorbent, the valence π band is not fully occupied. The Fermi level falls below the Dirac point.

1.2.5 Fabrication of graphene

Three major ways have been developed to fabricate graphene. Although this is not what the computational physics dissertation should focus on, a brief introduction here can help understand the motivations we have for the simulations. The exfoliated graphene is the first method used by Novoselov et al ¹² in 2004 to peel layers of graphene flakes from weakly bound graphite. The number of graphene layers can be determined by Raman spectroscopy. The exfoliated graphene can be further processed to create sample of suspended graphene which can be considered as freestanding graphene where the fundamental Dirac fermions properties are expected. However, the size of graphene produced in this method is small and it is not good for mass production. Later on the epitaxial growth of graphene technique arose. As a main route, epitaxial graphene growth

on hexagonal SiC developed by de Heer ¹³ has the advantage of making large scale graphene in high quality. Also, it is good for mass production and since the graphene is supported on the substrate, it is easy for processing. Because graphene is in contact with the SiC, the interactions between graphene layer and substrate always exist. The influence on the electronic properties of graphene by the interface interactions is interesting to investigate. The dissertation will be focusing on this promising method. Last but not the least; chemical vapor deposition is a recently developed way to grow graphene layers¹⁴.

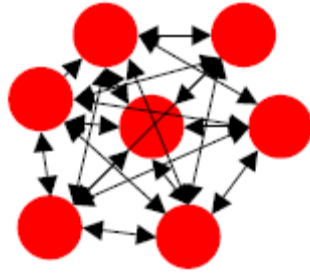


Figure 1.1 Interacting electrons in real potential

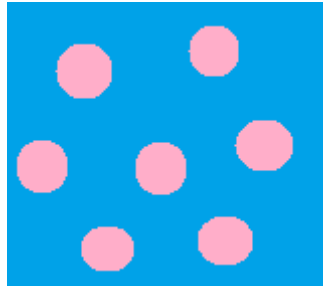


Figure 1.2 Non-interacting electrons in effective potential

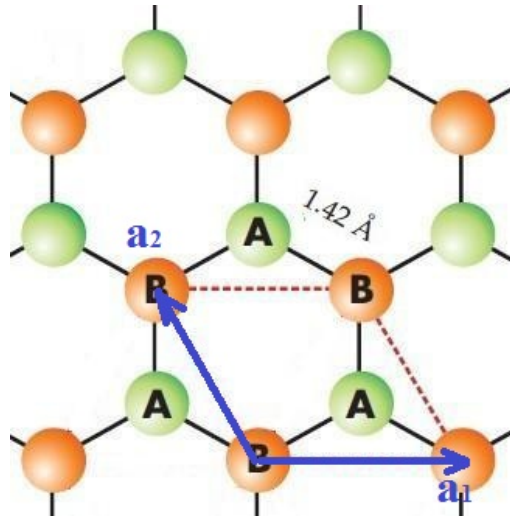


Figure 1.3 Graphene lattice in real space

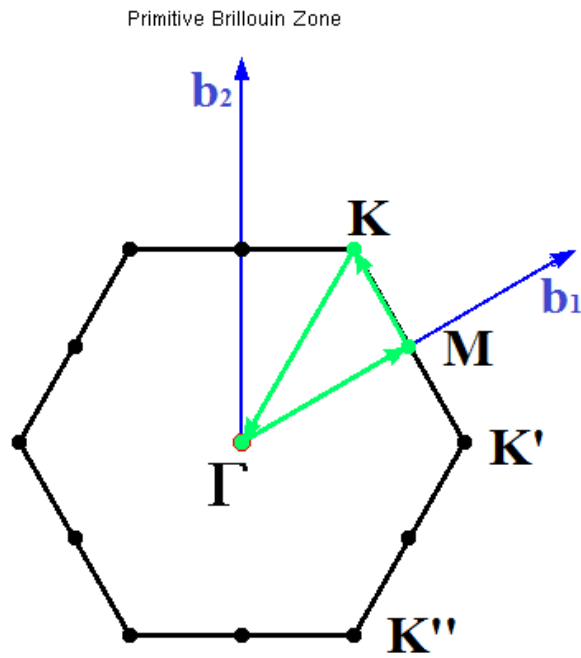


Figure 1.4 High symmetric points in Brillouin zone

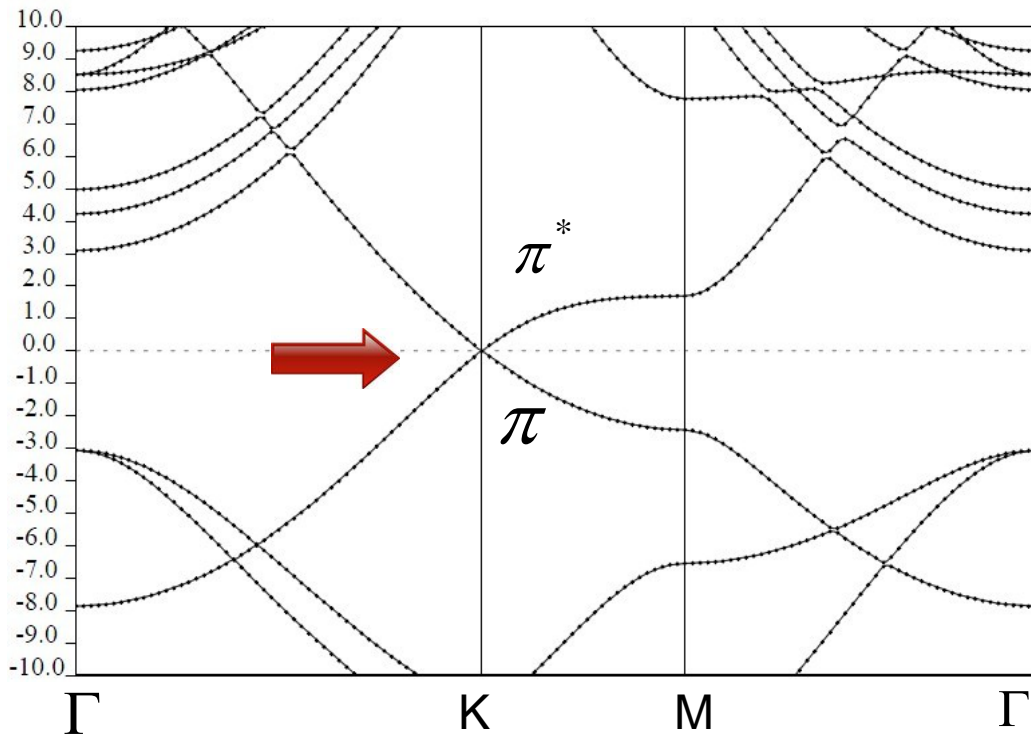


Figure 1.5 Band structure of graphene along high symmetric K path

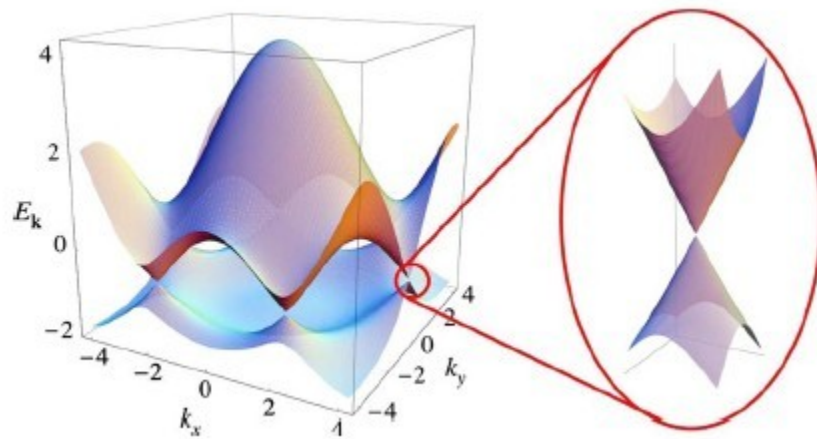


Figure 1.6 3D band structure of graphene and Dirac cone by A. H. Castro Neto¹⁵

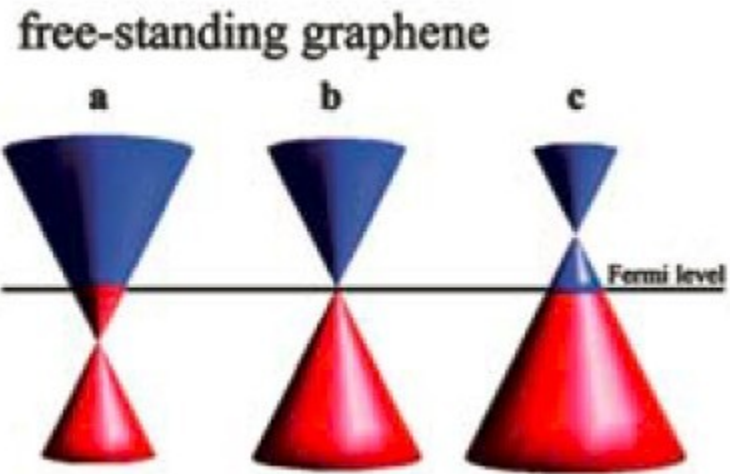


Figure 1.7 Dirac cones of n type doped, neutral and p type doped freestanding graphene
(I. Gierz et al)

Chapter 2 Electronic Properties of Graphene /6H-SiC(000 $\bar{1}$) interface: A First-principle Study

Electronic properties of the graphene/6H-SiC(000 $\bar{1}$) interface: A first-principles studyThushari Jayasekera,^{1,*} Shu Xu,¹ K. W. Kim,² and M. Buongiorno Nardelli^{1,3}¹*Department of Physics, North Carolina State University, Raleigh, North Carolina 27695-8202, USA*²*Department of Electrical and Computer Engineering, North Carolina State University, Raleigh, North Carolina 27695-7911, USA*³*Computer Science and Mathematics Division, Oak Ridge National Laboratory, Oak Ridge, Tennessee 37831, USA*

(Received 3 February 2011; revised manuscript received 21 April 2011; published 27 July 2011)

Using calculations from first principles, we show how the structural and electronic properties of epitaxial graphene on 6H-SiC(000 $\bar{1}$) are determined by the geometry and the chemical functionalization of the interface region. We also demonstrate that these properties can be correctly captured only if a proper treatment of the van der Waals interactions is included in the theoretical description based on density functional theory. Our results reproduce the experimentally observed *n*-type doping of monolayer epitaxial graphene and prove the possibility of opening a sizable (150 meV) energy gap in the bilayer case under special growth conditions. Depending on the details of the bonding at the interface, we are able to interpret recent experimental observations and provide a clear insight into the mechanisms of charge transfer and interface stability.

DOI: [10.1103/PhysRevB.84.035442](https://doi.org/10.1103/PhysRevB.84.035442)

PACS number(s): 73.22.Pr, 61.48.Gh, 71.15.Mb, 81.05.ue

I. INTRODUCTION

Although epitaxial graphene was first synthesized in 1975,¹ the first demonstration of its use in lithographically patterned devices in 2004² dramatically revamped the interest in this material and has paved the way to potential new classes of applications for innovative nanoelectronics.^{3,4} Advances in the understanding of epitaxial growth of graphene on SiC, which is the substrate of choice for microchip design, have the potential to revolutionize the semiconductor road map for future decades.^{5,6}

Epitaxial graphene on SiC is obtained by the sublimation of Si atoms either from the (0001) surface (Si-face) or from the (000 $\bar{1}$) surface (C-face) of 6H- or 4H-SiC polytypes. Si sublimation is achieved by annealing the SiC sample in ultrahigh vacuum (UHV) conditions or at moderate vacuum conditions in the presence of a background gas such as Ar.^{7,8}

The growth of epitaxial graphene on the Si-terminated face (0001) is characterized by the presence of an intermediate carbon layer (the “buffer layer”) that screens most of the effect of the substrate.^{9–11} On the C-terminated face, the situation can be quite different depending on the conditions of growth: Hass *et al.*^{12,13} have reported a strongly interacting first C-layer, i.e., a buffer layer on C-face, which is similar to the observation made on the graphene/SiC(0001) interface. On the other hand, a weakly bound or decoupled graphene layer is reported by many other groups.^{14–16} Moreover, different growth conditions can lead to different graphitic stacking sequences in multilayered samples: *AA*,¹⁵ *AB*,¹⁷ and, most frequently, misoriented (turbostratic)¹⁸ layers have been observed. Such structural differences are paralleled by an equally broad spread in the electronic structure characteristics: de Heer *et al.* reported that C-face epitaxial graphene is *n*-doped with the Dirac point approximately 300 meV below the Fermi level,⁷ while Emtsev *et al.* reported this value to be 200 meV.^{19,20} *p*-doped epitaxial graphene on the C-face has also been reported.^{21–23} Although some of these observations might be biased by uncontrollable ambient conditions, a deeper understanding of the interplay between structure and properties of the graphene/SiC(000 $\bar{1}$) interface is of paramount importance.

While the electronic and structural properties of the graphene/SiC(0001) interface have been the subject of many theoretical investigations,^{9,11} very few studies have been devoted to the understanding of the properties of the graphene/SiC(000 $\bar{1}$) system^{10,24} and the results are not always in agreement with the available experimental observations. Here, we use calculations from first principles based on density functional theory (DFT) to study the graphene on SiC(000 $\bar{1}$) surface. One common limitation of the DFT calculations is the inability to describe the long-range van der Waals (vdW) forces, which is an essential component of the interaction in layered systems. In this paper, we demonstrate that only by taking vdW interactions into account, one can correctly describe not only the geometry, but also the electronic structure of epitaxial graphene on the SiC(000 $\bar{1}$) surface.

The paper is organized as follows. In Sec. II, we discuss the geometry of the interface and give the technical details of our calculations; in Sec. III A, we discuss the importance of the inclusion of dispersion forces in determining correctly the electronic and structural properties of the graphene/SiC system; in Sec. III B, we elaborate on the structural and electronic modifications induced by a change in the interfacial chemistry; and in Sec. III C, we discuss the case of bilayer graphene. We conclude with some final remarks in Sec. IV.

II. METHODOLOGY

On the Si-terminated surface of SiC, a thermal annealing process results in a $\sqrt{3} \times \sqrt{3}R \cos(30^\circ)$ (*R3*) surface reconstruction followed by a $6\sqrt{3} \times 6\sqrt{3}R \cos(30^\circ)$ (*6R3*) reconstruction. Since the periodic unit cell for the *6R3* structure is large and computationally expensive to simulate, the *R3* model has been used for most calculations irrespective of the residual 7% mismatch between the *R3* cell of SiC and the 2×2 cell of graphene. This model correctly reproduces the experimental observations for graphene on SiC(0001), such as the presence of a strongly bonded buffer layer and an electron-doped first graphene layer.^{9,11} Even though the *R3* model is compatible with the C-face termination of SiC, it does not seem to correctly reproduce the experimentally observed

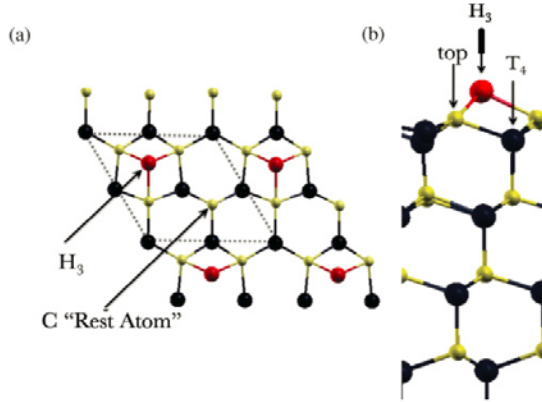


FIG. 1. (Color online) (a) Top view and (b) side view of the $(2 \times 2)_C$ reconstructed model for the SiC(0001) surface with a Si adatom in the $H3$ position. (b) shows all three possible high-symmetry positions $T4$, $H3$, and top for the Si adatom. Red (darker gray) atoms are Si adatoms, black atoms are Si in SiC bulk, and yellow (light gray) atoms are C in SiC bulk. The $(2 \times 2)_C$ unit cell is depicted by the dashed lines in the top view (a).

reconstructed structures either for the geometry or for their electronic properties.¹⁰ STM data show that the sublimation on the C-face starts with a 3×3 surface reconstruction, which later evolves into a $(2 \times 2)_C$ reconstruction.¹⁴ In order to follow the experimental observation, we have adapted the atomistic model proposed by Seubert *et al.*²⁵ and later used by Magaud *et al.*²⁴ for investigating the C-face epitaxial graphene. In the $(2 \times 2)_C$ reconstructed model proposed by Seubert *et al.*, three out of the four surface C atoms are bonded to a Si adatom. There are three high-symmetry positions that a Si adatom can bind to the C atoms on the open surface [Fig. 1(b)]: $H3$, the threefold coordinated hollow site; $T4$, a position directly on top of a Si atom in the layer underneath; and top , an adatom directly binds to a single C atom on the open surface. The top position only saturates one dangling bond, and it is clearly unfavorable. Between $H3$ and $T4$, $H3$ is found to be energetically more stable. In the $H3$ adatom configuration, there are still two unsaturated dangling bonds, one on the Si adatom and the other on the unbound C atom, “the rest atom” (see Fig. 1). On the reconstructed SiC(0001) surface, the difference in electronegativity between Si and C induces a charge transfer from the Si adatom to the C rest atom, which is responsible for the surface states observed in the band structure of the combined graphene/SiC system and the pinning of the Fermi energy at the interface [see Sec. III B and Fig. 4(a) for a more detailed discussion]. To minimize residual strain due to lattice mismatch between graphene and the SiC surface, a 5×5 graphene cell is overlaid on a 4×4 SiC cell with $(2 \times 2)_C$ surface reconstruction. This geometry reduces the lattice strain to less than $\sim 1\%$.

All the calculations are performed in the framework of DFT as it is implemented in the quantum-ESPRESSO package.²⁶ We have used a $3 \times 3 \times 1$ Monkhorst-Pack grid for Brillouin zone integration, 20–24 Å vacuum region to separate the slabs, and the geometries have been optimized to forces less than

0.025 eV/Å. In our choice of exchange and correlation functionals, we used both the local density approximation (LDA) (with 65 Ry energy cutoff for the plane-wave expansion) and the generalized gradient approximation (GGA) in the Perdew-Burke-Ernzerhof (PBE) form (40 Ry energy cutoff).²⁷ It is well known that local or semilocal approximations for the exchange and correlation energy (either LDA or GGA) in DFT fail to account for vdW interactions completely and that the quantitative agreement that one sometimes finds in the description of the bonding in layered systems (such as in graphite) using LDA is due to a fortuitous cancellation of errors that can not be taken as systematically correct for any graphene-based systems. We have included vdW interactions in our calculations for the GGA exchange and correlation functional using an empirical potential of the form $C_6 R^{-6}$ added to the regular density functional energy [GGA(D)] as proposed by Grimme *et al.*²⁸ and recently implemented by Barone *et al.*²⁹ in the quantum-ESPRESSO code. Magaud *et al.* have investigated the properties of the C-face epitaxial graphene with the same model within GGA approximation, with no vdW interactions.²⁴ In this paper, we demonstrate the importance of vdW interactions in these loosely bound layered systems.

III. RESULTS AND DISCUSSION

A. Effect of long-range dispersion forces on the geometry and the electronic structure of the interface

In order to quantify the effect of the inclusion of vdW forces on the interface structure and electronic characteristics, we optimized the geometry of the graphene/SiC system using LDA, GGA, and GGA(D). Table I summarizes the geometrical parameters of the optimized geometries in the three cases, while the corresponding electronic bands are presented in Fig. 2. In GGA, the average distance between the Si adatom and the graphene layer is ~ 3.29 Å, whereas this distance is 2.64 Å in LDA and 2.61 Å in GGA(D). LDA and GGA(D) give remarkably similar results, an indication that the cancellation of errors in LDA is indeed reproducing the more accurate GGA(D) results. The same similarity is observed in the electronic band structure [shown in Figs. 2(a) and 2(c)]. Both LDA and GGA(D) produce an electron-doped graphene layer with the Dirac point lying ~ 0.35 eV below the Fermi level. In contrast, GGA results in a neutral graphene layer [Fig. 2(b)] that is in agreement with previous calculations.²⁴ The ripples in the C layer (reported in Table I) are not strong enough to destroy the π orbital network in the graphene layer in any of the three systems.

TABLE I. Comparison of the geometries (average vertical distance between the Si adatom and the graphene layer d_{average} and the resultant ripple width) with different exchange and correlation (XC) functionals for LDA, GGA, and GGA(D).

XC functional	d_{average}	Ripple width
LDA	2.64 Å	0.16 Å
GGA	3.29 Å	0.04 Å
GGA(D)	2.61 Å	0.27 Å

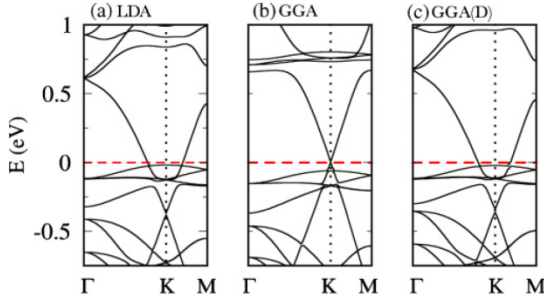


FIG. 2. (Color online) The electronic band structures (along Γ KM path) of epitaxial graphene on the C face of SiC in the Si adatom surface reconstructed model, calculated with (a) LDA, (b) GGA, and (c) GGA(D). Fermi level is set to 0 eV.

According to the results shown in Fig. 2(c), there is no evidence for the presence of a strongly bound layer or a buffer layer. In fact, the first C layer on the (000 $\bar{1}$) surface shows graphenic properties in contrast to the buffer layer on the Si face, and epitaxial graphene on SiC(000 $\bar{1}$) is electron doped as the experiments suggested. The n -doped behavior is hidden when the vdW interactions are not included in the calculation.²⁴ The electronic bands near the Fermi level are identified as dangling bond states of the C rest atoms [see Fig. 4(a)]. Si adatom dangling bond states are empty and lie around 1 eV above the Fermi level.

B. Effect of interfacial chemistry

The existence of dangling bond states at the interface suggests the possibility of passivation induced by external chemical species during the growth process. We have considered two prototypical cases: a *half-passivated* and a *fully passivated* interface. Only the C rest atoms are passivated in the *half-passivated* interface, leaving a dangling bond on the Si adatoms. The C rest atom-passivated system is 4.9 meV (per C atom in the graphene layer) more favorable than the Si-adatom-passivated system. Both the Si adatoms and the C rest atoms are passivated with H in the *fully passivated* system. The differences among the three configurations are striking: In the unpassivated interface, the graphene layer maintains its individuality although it becomes n -doped; in the half-passivated system, the graphene-Si adatom interaction is so strong that the graphene binds strongly with the substrate, giving rise to a buffer layer similar to what happens for the growth on the Si-terminated face; finally, the fully passivated

TABLE II. Comparison of the geometries (the average vertical distance d_{average} , between the Si adatom and the graphene layer and the resultant ripple width) for different interfacial configurations.

System	d_{average}	Ripple width
Unpassivated	2.61 Å	0.27 Å
Half-passivated	2.28 Å	0.50 Å
Full passivated	3.83 Å	0.10 Å

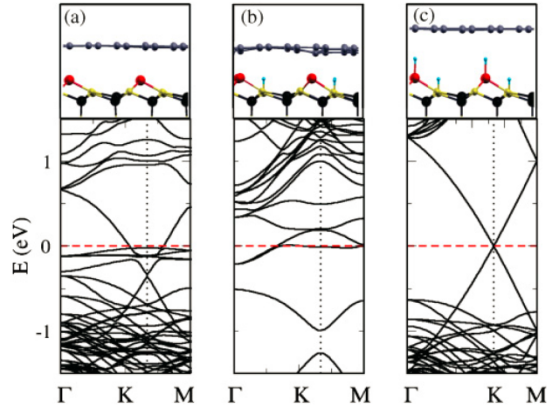


FIG. 3. (Color online) The electronic band structures (along Γ KM path) of graphene on the C face of SiC with different interfacial passivation: (a) unpassivated, (b) half-passivated, and (c) fully passivated. The upper panel shows the atomic configuration of the three interface configurations. Fermi level is set to 0 eV.

system shows a completely decoupled graphene layer with the ideal Dirac band dispersion.

Our results are summarized in Fig. 3, and the parameters describing the three optimized geometries are tabulated in Table II. In the half-passivated case, the passivation of the C rest atom prevents the Si-C charge transfer that occurs in the unpassivated interface. Thus, the Si dangling bond states become half-occupied and interact strongly with the C atoms of the graphene layers. The average distance between the Si adatoms and the graphene layer shortens considerably, ~ 2.28 Å, and the graphene layer shows a higher degree of vertical deformation with an average ripple width of 0.5 Å. Since the graphene layer now lies closer to the substrate, the interaction between the Si adatoms and the C atoms disrupts the sp^2 hybridization of the π orbital network and the linear band dispersion at the Dirac point [Fig. 4(b)]. Once the interface is fully passivated with H, the graphene layer effectively decouples from the substrate with a separation of 3.8 Å (with a negligible 0.1 Å ripple width), and therefore shows neutral graphene characteristics as shown in Fig. 4(c).

These results can, in part, explain the wide range of variation of the electronic properties observed during growth of graphene on the C-face. In particular, depending on the

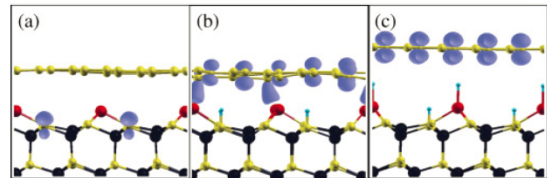


FIG. 4. (Color online) The electron density of the states localized on the interface at the Dirac point for (a) unpassivated, (b) half-passivated, and (c) fully passivated systems. Blue isosurfaces correspond to 0.15×10^{-3} electrons.

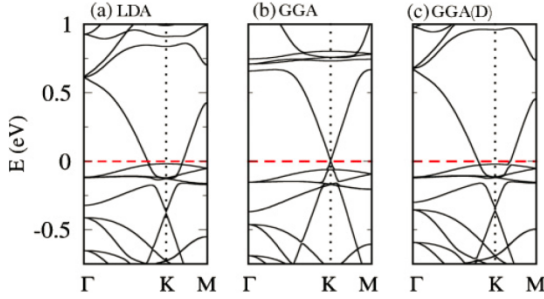


FIG. 2. (Color online) The electronic band structures (along Γ KM path) of epitaxial graphene on the C face of SiC in the Si adatom surface reconstructed model, calculated with (a) LDA, (b) GGA, and (c) GGA(D). Fermi level is set to 0 eV.

According to the results shown in Fig. 2(c), there is no evidence for the presence of a strongly bound layer or a buffer layer. In fact, the first C layer on the $(000\bar{1})$ surface shows graphenic properties in contrast to the buffer layer on the Si face, and epitaxial graphene on SiC $(000\bar{1})$ is electron doped as the experiments suggested. The n -doped behavior is hidden when the vdW interactions are not included in the calculation.²⁴ The electronic bands near the Fermi level are identified as dangling bond states of the C rest atoms [see Fig. 4(a)]. Si adatom dangling bond states are empty and lie around 1 eV above the Fermi level.

B. Effect of interfacial chemistry

The existence of dangling bond states at the interface suggests the possibility of passivation induced by external chemical species during the growth process. We have considered two prototypical cases: a *half-passivated* and a *fully passivated* interface. Only the C rest atoms are passivated in the *half-passivated* interface, leaving a dangling bond on the Si adatoms. The C rest atom-passivated system is 4.9 meV (per C atom in the graphene layer) more favorable than the Si-adatom-passivated system. Both the Si adatoms and the C rest atoms are passivated with H in the *fully passivated* system. The differences among the three configurations are striking: In the unpassivated interface, the graphene layer maintains its individuality although it becomes n -doped; in the half-passivated system, the graphene-Si adatom interaction is so strong that the graphene binds strongly with the substrate, giving rise to a buffer layer similar to what happens for the growth on the Si-terminated face; finally, the fully passivated

TABLE II. Comparison of the geometries (the average vertical distance d_{average} , between the Si adatom and the graphene layer and the resultant ripple width) for different interfacial configurations.

System	d_{average}	Ripple width
Unpassivated	2.61 Å	0.27 Å
Half-passivated	2.28 Å	0.50 Å
Full passivated	3.83 Å	0.10 Å

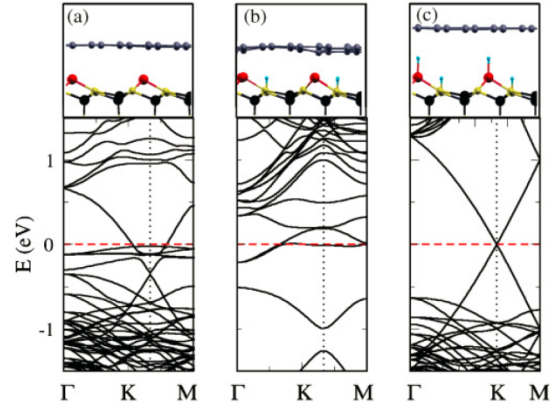


FIG. 3. (Color online) The electronic band structures (along Γ KM path) of graphene on the C face of SiC with different interfacial passivation: (a) unpassivated, (b) half-passivated, and (c) fully passivated. The upper panel shows the atomic configuration of the three interface configurations. Fermi level is set to 0 eV.

system shows a completely decoupled graphene layer with the ideal Dirac band dispersion.

Our results are summarized in Fig. 3, and the parameters describing the three optimized geometries are tabulated in Table II. In the half-passivated case, the passivation of the C rest atom prevents the Si-C charge transfer that occurs in the unpassivated interface. Thus, the Si dangling bond states become half-occupied and interact strongly with the C atoms of the graphene layers. The average distance between the Si adatoms and the graphene layer shortens considerably, ~ 2.28 Å, and the graphene layer shows a higher degree of vertical deformation with an average ripple width of 0.5 Å. Since the graphene layer now lies closer to the substrate, the interaction between the Si adatoms and the C atoms disrupts the sp^2 hybridization of the π orbital network and the linear band dispersion at the Dirac point [Fig. 4(b)]. Once the interface is fully passivated with H, the graphene layer effectively decouples from the substrate with a separation of 3.8 Å (with a negligible 0.1 Å ripple width), and therefore shows neutral graphene characteristics as shown in Fig. 4(c).

These results can, in part, explain the wide range of variation of the electronic properties observed during growth of graphene on the C-face. In particular, depending on the

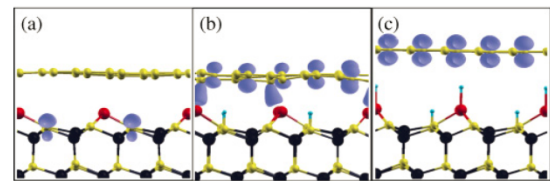


FIG. 4. (Color online) The electron density of the states localized on the interface at the Dirac point for (a) unpassivated, (b) half-passivated, and (c) fully passivated systems. Blue isosurfaces correspond to 0.15×10^{-3} electrons.

TABLE III. Vertical distance between the first graphene layer and the Si adatoms Δ_0 and between the first and second C layers Δ_1 for different passivations and stacking sequences.

System	Δ_0	Δ_1
Unpassivated (<i>AA</i>)	2.62 Å	3.47 Å
Unpassivated (<i>AB</i>)	2.60 Å	3.23 Å
Half-Passivated (<i>AA</i>)	2.26 Å	3.41 Å
Half-Passivated (<i>AB</i>)	2.27 Å	3.25 Å
Full Passivated (<i>AA</i>)	3.86 Å	3.46 Å
Full Passivated (<i>AB</i>)	3.86 Å	3.24 Å

experimental conditions, passivation might occur and give rise to samples that can, in turn, be neutral or *n*-doped, and with a geometry that can vary between fully decoupled or completely distorted by interface bonds (buffer layer).

C. Bilayer graphene on SiC(000 $\bar{1}$)

The effect of the inclusion of vdW forces in the calculations is even more pronounced in the case of bilayer graphene, where the intralayer interactions of the two graphene planes add to the stability of the interface. When more than one layer of graphene is grown on SiC(000 $\bar{1}$), the stacking of the layers can also vary depending on the growth conditions: the observation of islands of Bernal stacking (*AB*),¹⁷ *AA* stacking,¹⁵ and of distorted (turbostratic)¹⁸ sequences have been reported in the literature. While it is important to investigate the properties of turbostratic stacking sequences,^{31,32} in this paper we focus on the comparison between *AA* and *AB* geometries. Only little has been done on the theoretical side on more than one C layer on the SiC(000 $\bar{1}$) surface, and indeed we are aware of only few studies where different hexagonal stacking sequences have been characterized on the unrealistic *R3* reconstruction.^{10,15} Table III compares the interlayer distance Δ_1 and the Si adatom/first-C-layer distance Δ_0 for various interface configurations. Similar to the monolayer case, the shortest Si adatom-graphene distance and the higher ripple width are found in the half-passivated system, where the strong interaction between the Si dangling bond state and the first graphene layer determine the geometrical structure.

Of course, different geometries induce different electronic behaviors. In Fig. 5, we display the calculated energy bands for unpassivated [(a) *AB* stacking, (b) *AA* stacking], half-passivated [(c) *AB* stacking, (d) *AA* stacking], and fully passivated [(e) *AB* stacking, (f) *AA* stacking] interfaces and we analyze the effect of the layer ordering on the electronic properties of the systems. In both the unpassivated and fully passivated cases, we observe a marked distinction between the *AB* and *AA* stacking, although the difference in their relative stability is negligible (in all configurations, the *AB* stacking is energetically slightly more favorable by a few meV/C atom).

In the ideal suspended graphene geometry, the *AB* stacking causes a symmetry breaking that induces an inequivalence of the C atoms in the benzene rings. This inequivalence is responsible for the opening of a small energy gap. On the other hand, in the *AA* stacking sequence, this symmetry breaking does not take place and the two graphene planes are effectively independent and display a typical double Dirac cone structure.³⁰

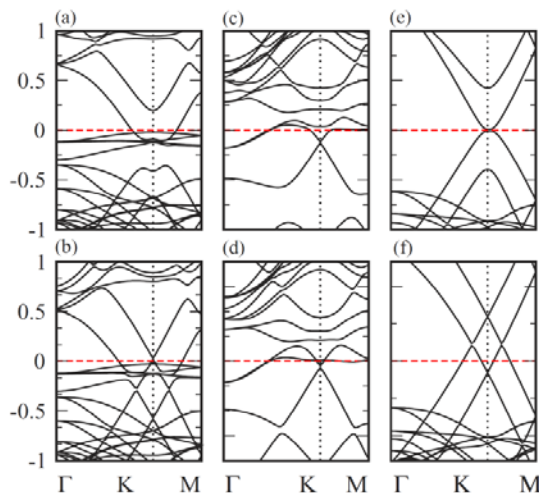


FIG. 5. (Color online) Electronic band structures (along ΓKM path) of graphene bilayers on the (2×2) , SiC(000 $\bar{1}$) surface with (a), (b) unpassivated, (c), (d) half-passivated, and (e), (f) full-passivated interface. The upper [(a), (c), (e)] and lower [(b), (d), (f)] panels show the electronic bands for *AB* and *AA* stackings, respectively.

When grown epitaxially on SiC(000 $\bar{1}$), the bilayer maintains some of its ideal characteristics. This is better observed in the case of the fully passivated interface, where the degree of decoupling between the bilayer and the substrate makes the system behave almost as in the ideal case. The *AB* geometry [Fig. 5(e)] displays a small energy gap (of the order of a few meV), while the *AA* system [Fig. 5(f)] shows evidence of the double Dirac cone structure. It is important to note, though, that the Fermi energy is lower than the Dirac point energy, so that the bilayer is effectively *p*-doped.

The situation changes drastically in the unpassivated case: The *AB* bilayer [Fig. 5(a)] electronic structure displays a large (~ 150 meV) energy gap that is induced by the fact that the first graphene layers screen only partially the effect of the substrate on the second layer, thus, enhancing the intralayer interaction and the symmetry breaking between the two inequivalent Dirac points of the two layers. The system is still *n* type with the Fermi level pinned by the C rest atom interface states. On the contrary, in the *AA* stacking sequence [Fig. 5(b)], the electronic bands show a higher degree of decoupling and display the typical double crossing of the Dirac cones, with only a negligible band-gap opening. Finally, in the half-passivated system [Figs. 5(c) and 5(d)], the top layer behaves effectively as a single graphene layer on a C buffer, a situation that reminds again of the Si-face growth geometry. In both layer orderings, the graphene is *n* type.

IV. CONCLUSIONS

In summary, we have investigated the properties of epitaxial graphene on SiC(000 $\bar{1}$) surface with the Si adatom reconstructed model of Seubert *et al.* and we have demonstrated

the importance of the inclusion of van der Waals interactions in determining the correct equilibrium geometries and their electronic properties. Our analysis of interfacial chemistry and passivation of the interface shows how the n -type behavior of the system and the relative band alignment between SiC and graphene can be varied, and provides an insight into the reason why experimental observations can give different results depending on the sample growth or other environmental conditions.³³

ACKNOWLEDGMENTS

This work was supported, in part, by the DARPA/HRL CERA, the FCRP FENA programs, and NSF. M.B.N. wishes to acknowledge partial support from the Office of Basic Energy Sciences, US Department of Energy at Oak Ridge National Laboratory, under Contract No. DE-AC05-00OR22725 with UT-Battelle, LLC. Calculations have been performed at NCCS-ORNL and HPC-NCSU.

*thusharij@gmail.com

¹A. J. VanBommel, J. E. Crombeen, and A. VanTooren, *Surf. Sci.* **48**, 463 (1975).

²C. Berger, Z. Song, T. Li, X. Li, A. Y. Ogbazghi, R. Feng, Z. Dai, A. N. Marchenkov, E. H. Conrad, P. N. First, and W. A. de Heer, *J. Phys. Chem. B* **108**, 19912 (2004).

³K. S. Novoselov, A. K. Geim, S. V. Morozov, D. Jiang, Y. Zhang, S. V. Dubonos, I. V. Grigorieva, and A. A. Firsov, *Science* **306**, 666 (2004).

⁴Y. Zhang, Y. W. Tan, H. L. Stormer, and P. Kim, *Nature (London)* **438**, 201 (2005).

⁵W. A. de Heer, C. Berger, X. Wu, P. N. First, E. H. Conrad, X. Li, T. Li, M. Sprinkle, J. Hass, M. L. Sadowski, M. Potemski, and G. Martinez, *Solid State Commun.* **143**, 92 (2007).

⁶K. S. Novoselov, A. K. Geim, S. V. Morozov, D. Jiang, M. I. Katsnelson, I. V. Grigorieva, S. V. Dubonos, and A. A. Firsov, *Nature (London)* **438**, 197 (2005).

⁷W. A. de Heer, C. Berger, X. Wu, M. Sprinkle, Y. Hu, M. Ruan, J. A. Storscio, P. N. First, R. Haddon, B. Piot, C. Faugeras, M. Potemski, and J. S. Moon, *J. Phys. D: Appl. Phys.* **43**, 374007 (2010).

⁸Luxmi, N. Srivastava, G. He, R. M. Feenstra, and P. J. Fisher, *Phys. Rev. B* **82**, 235406 (2010).

⁹A. Mattausch and O. Pankratov, *Phys. Rev. Lett.* **99**, 076802 (2007).

¹⁰F. Varchon, R. Feng, J. Hass, X. Li, B. N. Nguyen, C. Naud, P. Mallet, J. Y. Veuillen, C. Berger, E. H. Conrad, and L. Magaud, *Phys. Rev. Lett.* **99**, 126805 (2007).

¹¹T. Jayasekera, B. D. Kong, K. W. Kim, and M. Buongiorno Nardelli, *Phys. Rev. Lett.* **104**, 146801 (2010).

¹²J. Hass, W. A. de Heer, and E. H. Conrad, *J. Phys. Condens. Matter* **20**, 323202 (2008).

¹³C. Berger, X. Wu, P. N. First, E. H. Conrad, X. Li, M. Sprinkle, J. Hass, F. Varchon, L. Magaud, M. Sadowski, M. Potemski, G. Martinez, and W. A. de Heer, *Adv. Solid State Phys.* **47**, 145 (2008).

¹⁴F. Hiebel, P. Mallet, F. Varchon, L. Magaud, and J. Y. Veuillen, *Phys. Rev. B* **78**, 153412 (2008).

¹⁵J. Borysiuk, K. Soltys, and J. Piechota, e-print [arXiv:1006.1040](https://arxiv.org/abs/1006.1040).

¹⁶M. Sprinkle, D. Siegel, Y. Hu, J. Hicks, A. Tejada, A. Taleb Ibrahim, P. LeFevre, F. Bertran, S. Vizzini, H. Enriquez, S. Chiang, P. Soukiassian, C. Berger, W. A. de Heer, A. Lanzara, and E. H. Conrad, *Phys. Rev. Lett.* **103**, 226803 (2009).

¹⁷M. Orlita, C. Faugeras, J. Borysiuk, J. M. Baranowski, W. Strupinski, M. Sprinkle, C. Berger, W. A. de Heer, D. M. Basko, G. Martinez, and M. Potemski, *Phys. Rev. B* **83**, 125302 (2011).

¹⁸J. Hass, F. Varchon, J. E. Millán-Otoya, M. Sprinkle, N. Sharma, W. A. de Heer, C. Berger, P. N. First, L. Magaud, and E. H. Conrad, *Phys. Rev. Lett.* **100**, 125504 (2008).

¹⁹K. V. Emtsev, F. Speck, Th. Seyller, L. Ley, and J. D. Riley, *Phys. Rev. B* **77**, 155303 (2008).

²⁰C. Berger, Z. Song, X. Li, X. Wu, N. Brown, C. Naud, D. Mayou, T. Li, J. Hass, A. N. Marchenkov, E. H. Conrad, P. N. First, and W. A. de Heer, *Science* **312**, 1191 (2006).

²¹Y. M. Lin, C. Dimitrakopoulos, D. B. Farmer, S. J. Han, Y. Q. Wu, W. J. Zhu, D. K. Gaskill, J. L. Tedesco, R. L. Myerd-Ward, C. R. Eddy Jr., A. Grill, and P. Avouris, *Appl. Phys. Lett.* **97**, 112107 (2010).

²²D. L. Miller, K. D. Kubista, G. M. Rutter, M. Ruan, W. A. de Heer, P. N. First, and J. A. Storscio, *Science* **324**, 924 (2009).

²³T. Hofmann, A. Boosalis, B. Kuhne, C. M. Herzinger, J. A. Woollam, D. K. Gaskill, J. L. Tedesco, and M. Schubert, *Appl. Phys. Lett.* **98**, 041906 (2011).

²⁴L. Magaud, F. Hiebel, F. Varchon, P. Mallet, and J. Y. Veuillen, *Phys. Rev. B* **79**, 161405 (2009).

²⁵A. Seubert, J. Bernhardt, M. Nerding, U. Starke, and K. Heinz, *Surf. Sci.* **45**, 454 (2000).

²⁶Paolo Giannozzi *et al.*, *J. Phys. Condens. Matter* **21**, 395502 (2009).

²⁷For GGA, we used C.pbe-rrkjus.UPF, H.pbe-rrkjus.UPF, and Si.pbe-n-van.UPF pseudopotentials for C, H, and Si, respectively. For LDA, C.pz-vbc.UPF, H.pz-vbc.UPF, and Si.pz-vbc.UPF pseudopotentials were used.

²⁸S. Grimme, *J. Comput. Chem.* **25**, 1463 (2004).

²⁹V. Barone, M. Casarin, D. Forrer, M. Pavone, M. Sambri, and A. Vittadini, *J. Comput. Chem.* **30**, 934 (2009).

³⁰E. J. Mele, *Phys. Rev. B* **81**, 161405 (2010).

³¹O. Pankratov, S. Hensel, and M. Bockstedte, *Phys. Rev. B* **82**, 121416 (2010).

³²M. Chen, W. Sun, G-C. Guo, and L. He, *Phys. Status Solidi B* **248**, 1690 (2011).

³³A. N. Sidorov *et al.* (unpublished).

Chapter 3 Electronic Properties of Epitaxial Graphene on 3C-SiC(100) Substrate

3.1 Experiment background

Queghi et al ¹⁶ have recently reported the structure of epitaxial graphene on 3C-SiC(100)/Si(100) wafers as the LEED image in Figure 3.1. The Micro-Raman spectroscopy indicates the characteristics of few layer graphene on the cubic 3C-SiC(100) substrate. In the meantime, Victor Yu et al ¹⁷ have demonstrated the feasibility of graphene synthesis on commercially available cubic SiC/Si substrate of diameter greater than 300 mm. This newly invented epitaxial growth of graphene on cubic SiC substrate has the advantage of being compatible with current Si processing technology and the ability to produce large scale (wafer size) graphene.

3.2 Reciprocal lattice of graphene/3C-SiC(100)

The LEED pattern obtained in Figure 3.1 can be used to study the atomic structure of the interface as it represents the reciprocal lattice. The dots shown by black square boxes come from the contribution of the cubic 3C-SiC(100) lattice. The dots shown by blue and

red arrows come from the hexagonal lattices of graphene. The angle between graphene domain axis and the square SiC lattice axis is either 15° or -15° , respectively as in Figure 3.2.

Using the STM topographic image of the graphene layer on cubic SiC substrate obtained as in Figure 3.3, Victor Yu et al¹⁸ determined the orientation of the graphene overlayer shown in black arrows with respect to cubic SiC substrate shown in white arrow by fast Fourier transformation (FFT). There is also a 15° angle between crystallographic axes of graphene and SiC substrate, which agrees with observations of Ouerghi et al.

3.2.1 Graphene/3C-SiC(100) unit cell

The unit cell of bulk 3C-SiC is a zincblende lattice as in Figure 3.4a where the C (yellow) atoms is a FCC lattice while Si atoms (blue) is also a FCC shifted by a quarter length along the diagonal line of the cubic. Figure 3.4b shows the top view from [100] direction, which is the ideal unreconstructed (1×1) surface with a superimposed 2×2 unit cell. By applying the fast Fourier transform (FFT) with the data of LEED in Figure 3.1, we get the lattice of graphene on 3C-SiC(100) system in real space. In this case, the graphene lattice is still hexagonal and 3C-SiC(100) is still square in real space but rotated by 90°

simultaneously with respect to their unit cell in reciprocal space. Therefore the angle between graphene lattice and 3C-SiC(100) lattice remains $\pm 15^\circ$ as the scheme given by Ouerghi et al as in Figure 3.5 which shows the lattice of graphene with two orientations on top of the square SiC lattice in real space.

A commensurate unit cell of graphene/3C-SiC(100) must be constructed before DFT calculations can be performed. By observing scheme in Figure 3.5 we find that the four C atoms pointed by green arrows are nearly right above the Si atoms from the SiC at first glance. It appears this rotated graphene cell with 4 C atoms on the corner pointed by green arrows is commensurate with the 4×4 3C-SiC(100) supercell. This gives us a clue to construct the unit cell that is sufficient small and realistic for doing DFT calculations. However, after isolating the cell from the periodic graphene lattice, we get a cell in rhombus shape rather than a standard square as in Figure 3.6a. The left bottom angle is $\sim 87.8^\circ$. Since this angle is very close to a right angle, we think there is a possibility that the interactions from the corners of the 4×4 3C-SiC(100) supercell makes the graphene compressed in the diagonal direction thereby forming a standard square as in Figure 3.6b (we name it layer A). If this does not happen naturally, this assumption can be used as an approximation which helps construct the unit cell small enough for practical simulation. Otherwise if we keep the theoretical geometry restrict, the commensurate unit cell would

too large. Therefore it is too expensive or even impossible to perform calculations. To make this square unit cell, a 2.8% compressive strain needs to be applied along the diagonal direction (shown by red arrows in Figure 3.6b). This strained graphene layer A corresponds to the blue dots in reciprocal space as in Figure 3.2 b. By rotating layer A by 90° we get graphene layer A' as in Figure 3.6 c which corresponds to the Figure 3.2a in reciprocal space. As claimed by F Varchon et al ¹⁹, even a “coherent match” geometry of graphene/6H-SiC with 8% strain has no qualitative effect on a freestanding graphene electronic structure (it will only change the Dirac electron velocity). Therefore we believe the 2.8% strain is reasonably small that the electronic characteristics of graphene will be preserved.

In experiments, both graphene layers with $+15^\circ$ and -15° with respect to the square SiC axes are detected by LEED image, probably because in a single domain, graphene layers with two orientations are present ²⁰. This phenomenon is similar to the turbostratic stacking bilayer graphene grown on C face 6H-SiC where a moiré pattern exists²¹.

3.3 Methodology

All the calculations are performed using Quantum ESPRESSO²² code package based on density functional theory. We have used a $4 \times 4 \times 1$ Monkhorst-Pack K grid in the Brillouin

zone. The vacuum space between the two periodic slabs is around 15 Å. Generalized gradient approximation (GGA) and ultrasoft pseudopotentials are used. For the substrate with two graphitic carbon layers, van de Waals force is included to compute the atomic distance between layers more precisely. The plane wave energy cutoff is set to be 25 Ry. Tests have been performed in advance to guarantee convergence. Residual forces in the relaxed structure are small than 0.025 eV/Å.

Due to the minor strain, graphene BZ is slightly distorted as the symmetry breaks. A lot of patience is needed to produce the correct BZ plot. Once lattice vector a_1 , a_2 are computed (they are slightly different in length), Eq(1.18) (1.19) should be strictly applied to guarantee the accurate b_1 and b_2 . With b_1 and b_2 , BZ can be precisely plotted. All high symmetric points K and M become nonequivalent as designated with K_1, K_2, K_3 and M_1, M_2, M_3 . As in Figure 3.7a and 3.7b represent the BZ of graphene layer A and A' in Figure 3.6b and 3.6c, respectively. K paths $G-K_1-M_1$, $G-K_2-M_2$, $G-K_3-M_3$ represent three possible K paths along high symmetric points. For each combination, we calculate the band structures along three nonequivalent paths labeled as $P_1-K_1-Q_1$, $P_2-K_2-Q_2$ and $P_3-K_3-Q_3$. (P is middle point of GK, Q is middle point of KM)

3.4 Graphene on unreconstructed 3C-SiC(100)

In the process of fabrication, samples are exposed to a series of annealing cycles with increasing temperature²³. Ideal unreconstructed surface along with different types of reconstructed surfaces are detected by LEED. It is unknown on which surface graphene behavior is observed. Therefore we start our investigations with the simple unreconstructed surface as suggested by the schematics given by both experimental groups. Besides, it is also unclear whether a carbon terminated or silicon terminated face of 3C-SiC(100) is used for graphene synthesis. Therefore, we list results from possible combinations containing two terminations of substrate both C and Si faces with turbostratic AA' stacking, up to two graphitic carbon layers.

3.4.1 First graphene layer A on C face 3C-SiC(100)

We put the first graphene layer A about 2 Å above the C terminated 3C-SiC(100) and perform structural optimization. After the relaxation, we find the graphene layer is distorted with a big ripple width of 0.69 Å and covalently bound to the C atoms on the SiC surface as in Figure 3.8. The average distance Δ_0 between graphene layer and C atoms on surface is 1.86 Å.

We find only flat surface band around the Fermi level in the band structure as in Figure 3.9. No linear dispersion appears at K because the strong interaction between substrate and graphene breaks the π bond.

3.4.2 First graphene layer A on Si face 3C-SiC(100)

On the Si face, the relaxed distance Δ_0 between graphene layer and Si atoms on surface is larger $\sim 2.47 \text{ \AA}$ as in Figure 3.10. The graphene is more seriously distorted with a huge ripple width of 1.31 \AA . Several C atoms in graphene layer are bound to the Si from the surface. The band structure as in Figure 3.10 is similar with the C face case with only flat bands around Fermi level. The huge vertical distortion plays a main role in breaking the π bond of graphene.

The first layer graphene on the both C and Si faces of 3C-SiC(100) serves as a buffer layer, which is similar to the graphene on 6H-SiC(0001) case²⁴ where the first graphene layer is also covalently bound to the Si atoms on the substrate .

3.4.3 Turbostratic AA' stacking graphene on C face 3C-SiC(100)

We optimized the atomic structure as in Figure 3.12 with second graphene layer A' on top of the first graphene layer A and got an optimal average distance of $\Delta_1 \sim 3.38 \text{ \AA}$. To clarify, here AA' does not mean bilayer graphene. We use AA' to represent the orientation of the 2nd graphene layer with respect to the first graphene layer which is the buffer layer. A means the 1st layer while A' mean the 2nd layer. The band structure show the graphenelike dispersion is recovered when the second graphene layer stacks. This top A' graphene plane is n type doped with the Dirac point shifted by 145 meV below the Fermi level. This can be compared with two graphitic C layers on the hexagonal 6H-SiC(0001) substrate where the second graphene layer is also n doped with Dirac point shifted by 400 meV. In fact the first graphene layer acts as a buffer layer which screens the effect from the 3C-SiC(100) substrate and makes the second graphene layer well isolated thereby showing n type doped graphene behavior.

Table 3.1 Geometries of turbostratic AA' stacking graphene on C face 3C-SiC(100)

Δ_0	Δ_1	Ripple 1L	Ripple 2L
1.71 \AA	3.38 \AA	0.76 \AA	0.04 \AA

3.4.4 Turbostratic AA' stacking graphene on Si face 3C-SiC(100)

On the Si polar face, a graphene plane with same orientation A' is added on and relaxed. Surprisingly, p type doped graphene dispersion is found with Dirac point shifted by 67 meV above the Fermi level. For the first time, p type doped graphene plain is calculated to be existent among the studies of few layer graphene on all kinds of SiC polytypes without extrinsic impurities that are widely used as doping sources. On the study of graphene on hexagonal 6H-SiC substrate, only n type doped graphene behavior is observed on both Si and C terminations²⁵.

Our investigation on the graphene on unreconstructed 3C-SiC(100) substrate has potential applications for industry because it can be utilized to fabricate graphene with n or p doping effect on different terminations of the same substrate solely via purely charge transfer.

Table 3.2 Geometries of turbostratic AA' stacking graphene on Si face 3C-SiC(100)

Δ_0	Δ_1	Ripple 1L	Ripple 2L
2.62 Å	3.51 Å	1.15 Å	0.19 Å

3.5 Graphene on reconstructed 3C-SiC(100)-c(2×2) surface

Our DFT calculations of second layer graphene on the cubic 3C-SiC(100) give band structures with the characteristics of p or n type doped single layer graphene, which is in partial agreement with A Querghi et al and Vicor Yu Aristov et al experiments results²⁶ where n type doped graphene on 3C-SiC(100) substrate is observed. However, it is concluded by A Querghi et al using XPS spectra²⁷ that the first graphene layer grows on top of 3C-SiC(100) without buffer layer based on binding energy analysis, which conflicts with our calculations. Therefore further study needs to be carried out to interpret this phenomenon. As we mentioned, in the annealing cycles, other phases of the substrate such as reconstructed Si-rich 3×2, C-terminated c(2×2) exist besides unreconstructed surface²⁸. It is highly possible that some of the measurements have been done on the reconstructed surface instead of the ideal 3C-SiC(100) surface as we did in our previous calculations. We thereby choose one of the most stable reconstructions, the C rich 3C-SiC(100)-c(2×2) surface as it is perfectly commensurate with our constructed square graphene cell.

3.5.1 Monolayer graphene layer on the staggered dimer model 3C-SiC(100)-c(2×2)

There are two theoretical models of C rich 3C-SiC(100)-c(2×2). Staggered dimer model was first proposed by Bermudez and Kaplan²⁹. As shown in Figure 3.16 carbon dimers arranged in staggered rows in form the adlayer. The dimer was initially assumed to have a C-C single bond with length of 1.54 Å (as in a typical saturated hydrocarbon) due to sp³ hybridization. Peter Käckel et al³⁰ , however, argued that carbon dimers are formed with a C=C double bond with length of 1.38 Å only slightly larger than the value 1.31 Å reported for aromatic carbon systems using DFT in 1996. We reproduced the carbon dimer bond length of 1.385 Å by relaxing the staggered dimer model with Quantum ESPRESSO and confirmed the predictions by Peter Käckel et al. Our result is listed in Table 3.3 in comparison with the other groups.

The band structure in Figure 3.17 shows p type doped graphene behavior with Dirac point shifted by 169 meV. It is much deeper p doped than the previous two graphene layers on Si face 3C-SiC case. The optimized structure has an average distance of ~ 3.08 Å between C dimer and graphene plane, which is greater than Δ_0 (1.86 Å) of first layer graphene on unreconstructed C face 3C-SiC and small than the layer spacing in

graphite³¹ (3.354 Å). The intermediate spacing value of 3.08 Å is appropriate for a weak interaction between graphene layer and C dimers on the substrate so charge transfer from graphene plane to the substrate can happen. If the spacing is too small, the strong interface interactions break the π bond and make the graphene characteristics disappear. If the spacing is too large, interactions become so weak that graphene becomes completely decoupled from substrate and stays neutral.

Table 3.3 C-C bond length of dimer in staggered dimer model 3C-SiC(100)-c(2×2)

	Bermudez Kaplan	Peter Käckel DFT	Our DFT
C-C bond length	1.54 Å	1.38 Å	1.385 Å

3.5.2 Monolayer graphene layer on the bridging dimer model 3C-SiC(100)-c(2×2)

The other model capable of explaining the c(2×2) reconstruction was first proposed by J.M. Powers et al in 1991³². This model also involves carbon dimers. As in Figure 3.19, each C of the dimer is bound to the Si underlayer, which forms a “bridge” and it is so called “bridging dimer” model. Depending on how the substrate is prepared, bridging model is divided into two slightly different submodels: (1) C₂H₄ exposure in Figure 3.19

and (2) Si sublimation in Figure 3.20. Unlike $c(2\times 2)$ produced by C_2H_4 exposure where the second layer Si atoms remains fixed, in $c(2\times 2)$ produced by Si sublimation, Si atoms in second layer shift a little bit and tend to form weak Si dimer bonds. The C_2H_4 exposure submodel gives a C-C bond length of 1.25 Å while the weak Si dimer in Si sublimation submodel results in a C-C bond length of 1.31 Å, which suggests sp^2 hybridization. This implies the C dimer is double bonded and there is one dangling electron on each carbon. However, our DFT structural optimization of the two different submodels end with basically the same geometric structure with C-C bond length of 1.23 Å. Again it is supported by DFT results of Peter Käckel et al that the C-C is more likely a triple bond.

Table 3.4 C-C bond length of dimer in bridging dimer model 3C-SiC(100)- $c(2\times 2)$

	C_2H_4 exposure Powers	Si sublimation Powers	Peter Käckel DFT	Our DFT
C-C bond length	1.25 Å	1.31 Å	1.23 Å	1.23 Å

The optimized structure in Figure 3.21 results in a spacing of 3.09 Å basically the same value with the stagger model. The band structure in Figure 3.22 shows a similar p type doped graphene with linear dispersion on Dirac point which falls 128 meV above Fermi level.

The strong interaction between carbon dimer with double or triple bond contributes to the p type rather than n type doping of graphene as it eliminates the dangling bond on the C adatom. In previous studies of graphene on both Si face and C face 6H-SiC, there are dangling bonds on Si atoms on the interface. The excess electrons transfers to the graphene layer, which makes it n type doped. In staggered model, each dimer C is bonded to the center and corner Si with σ bond, and there is double bond between dimer, where all four valence electrons form covalent bonds and no dangling bond exists. In bridging dimer model, similarly with one σ bond and a triple bond for each dimer carbon, no dangling bond survives. In both case, charge transfers from graphene layer to the substrate, which makes graphene p type doped. Although we have demonstrated monolayer graphene shows graphenelike linear dispersion on Dirac point without buffer layer, in experiment, only n type doped graphene is found. Calculations of other reconstructed surface needs to be examined in the future to see if it is in total agreement with experiment results.

3.6 Summary

We performed the ab initio calculations for the graphene on cubic 3C-SiC(100) and its reconstructed 3C-SiC(100)-c(2 \times 2) surfaces for the first time. On unreconstructed surface,

first graphene layer is covalently bonded and serves as a buffer layer. Both n and p type graphene behaviors were found for second graphene layers on C and Si faces, respectively, which has a potential application on industry. However, as it is claimed no interface layer was detected in experiment. We continued our study on the reconstructed surface. Our band structures of monolayer graphene on the reconstructed 3C-SiC(100)-c(2x2) for different models show p type doped graphene behavior without buffer layer. Although only n type was found in experiment, our p type result is also interesting as it rarely appears on epitaxial graphene on SiC without extrinsic impurity and worth further studies.

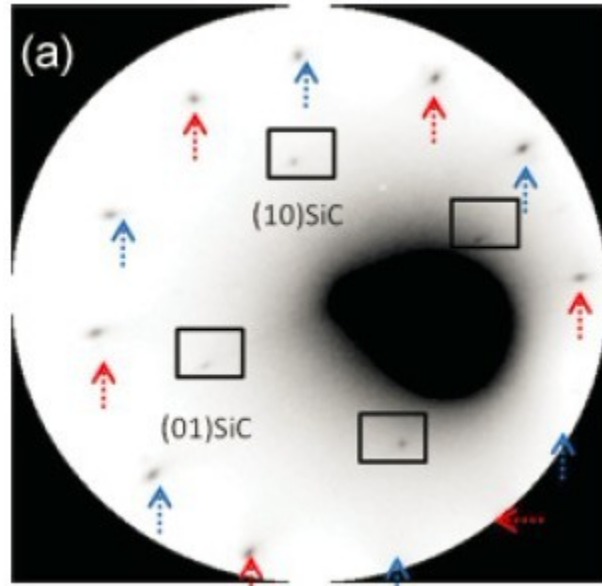


Figure 3.1 LEED image of graphene on 3C-Si(100) (Queghi et al ³³)

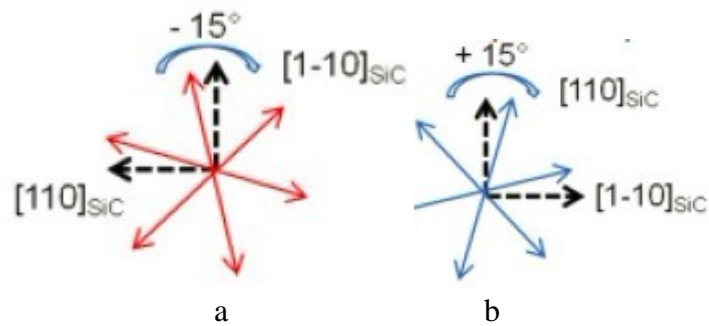


Figure 3.2 Crystallographic axes of graphene/3C-SiC(100) determined from LEED (Queghi et al)

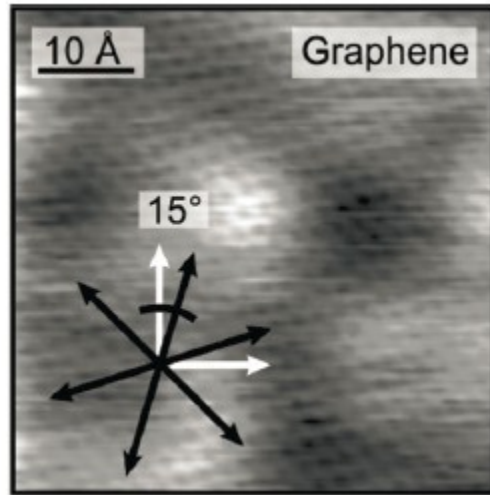


Figure 3.3 STM topographic image of the graphene layer on cubic SiC substrate
(Victor Yu et al ³⁴)

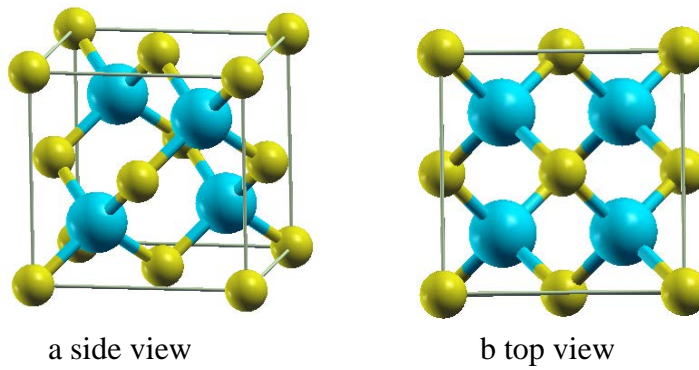


Figure 3.4 3C-SiC(100) crystal structure

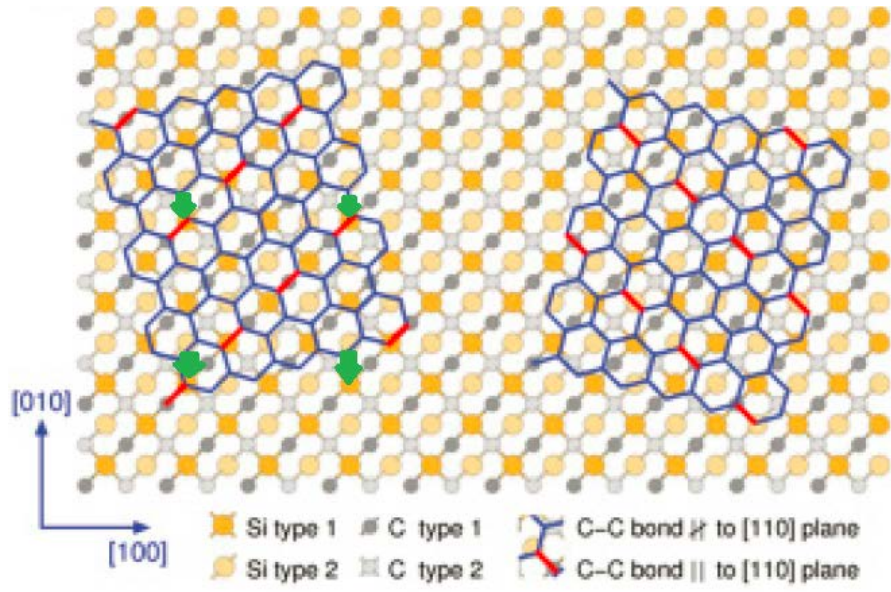


Figure 3.5 Schematic diagram of graphene layer on 3C-SiC(100) surface
 (Queghi et al ³⁵)

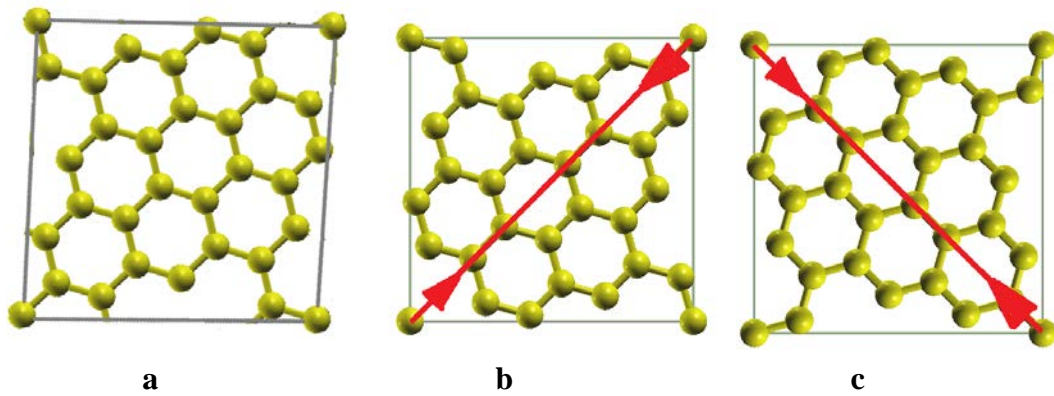


Figure 3.6 Square graphene cell under strain

- a rhombus graphene cell without strain
- b square graphene cell with diagonal strain
- c graphene cell in b rotated by 90°

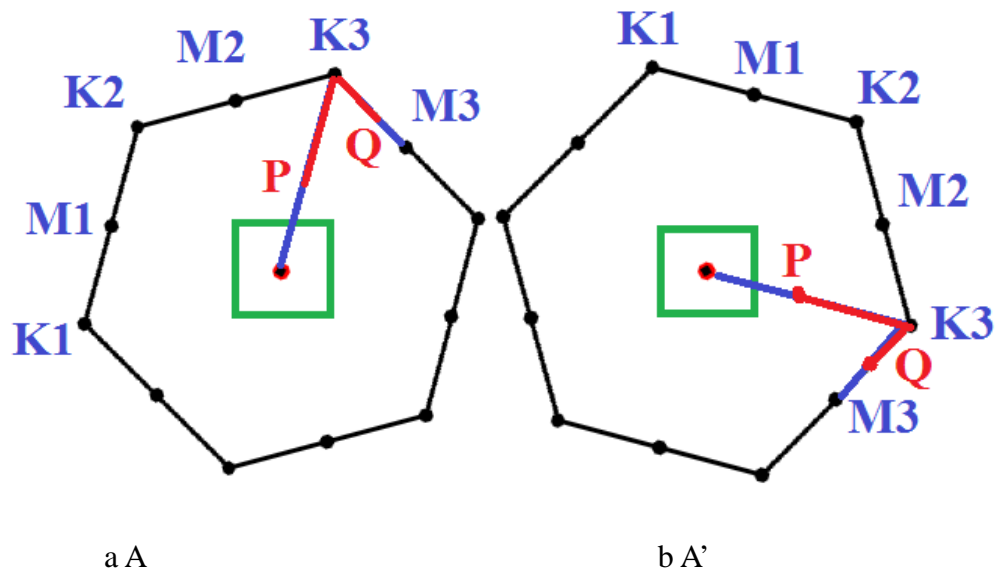


Figure 3.7 BZ of graphene supercell on 3C-SiC

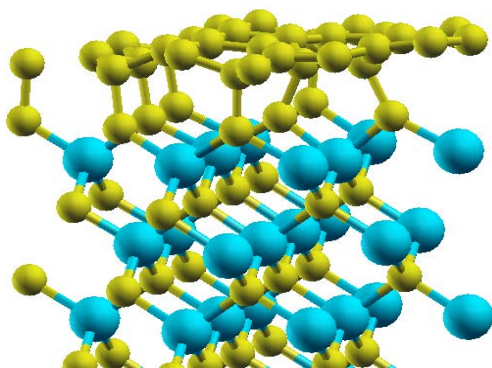


Figure 3.8 Optimized structure of first layer graphene on C face 3C-SiC(100)

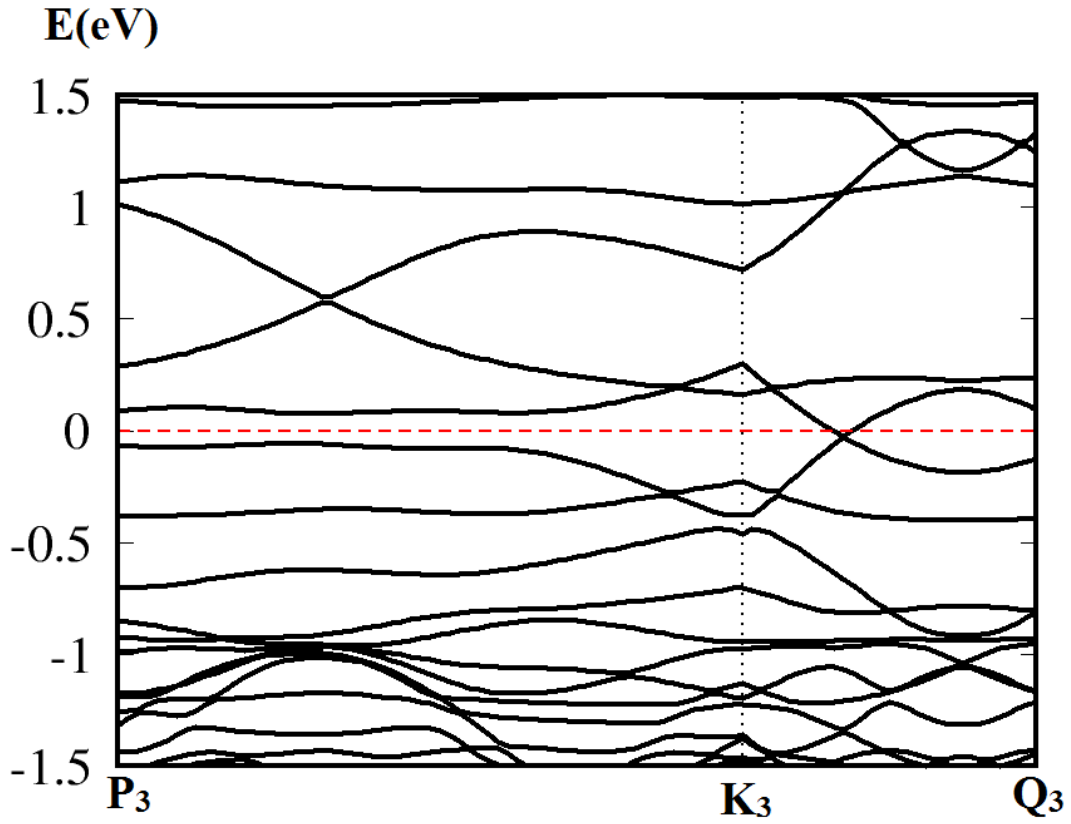


Figure 3.9 Band structure of first layer graphene on C face 3C-SiC(100)

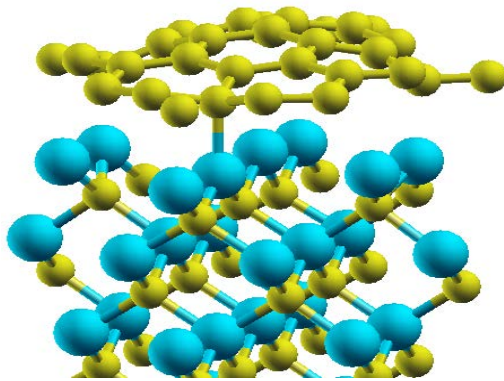


Figure 3.10 Optimized structure of first layer graphene on Si face 3C-SiC(100)

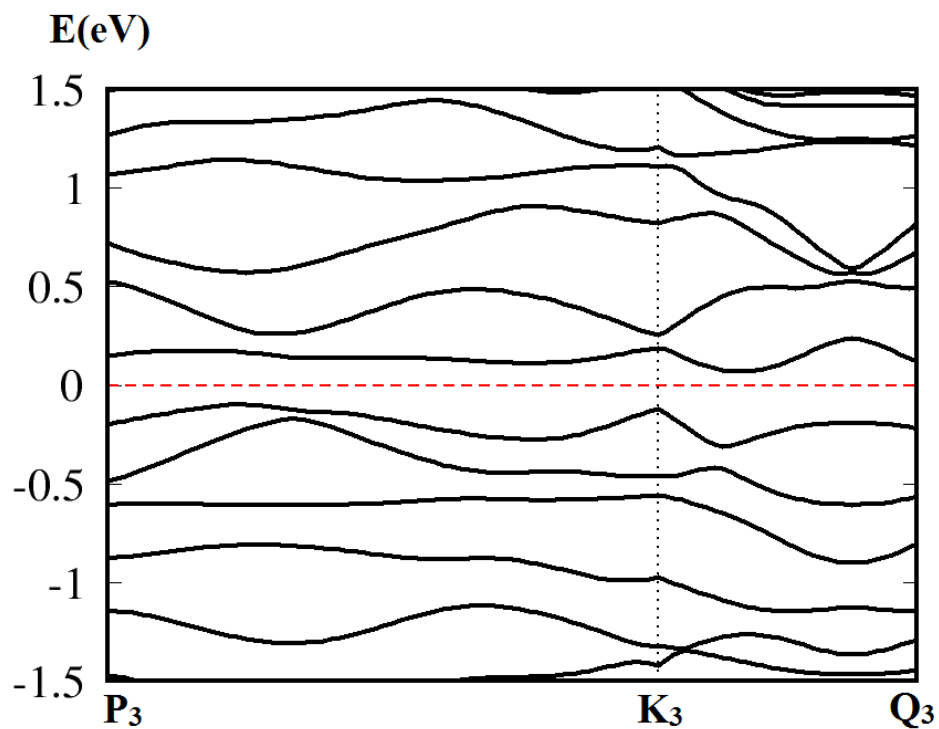


Figure 3.11 Band structure of first layer graphene on Si face 3C-SiC(100)

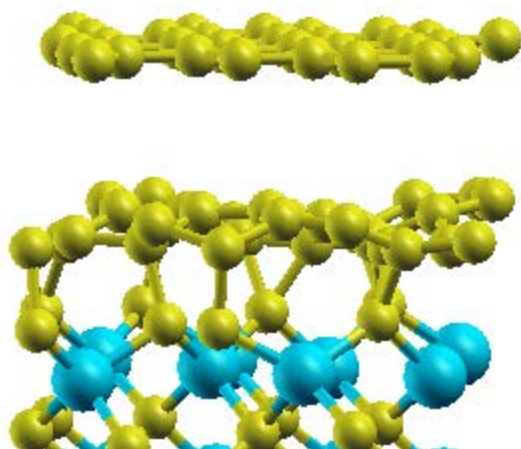


Figure 3.12 Optimized structure of turbostratic AA' stacking graphene on C face 3C-SiC(100)

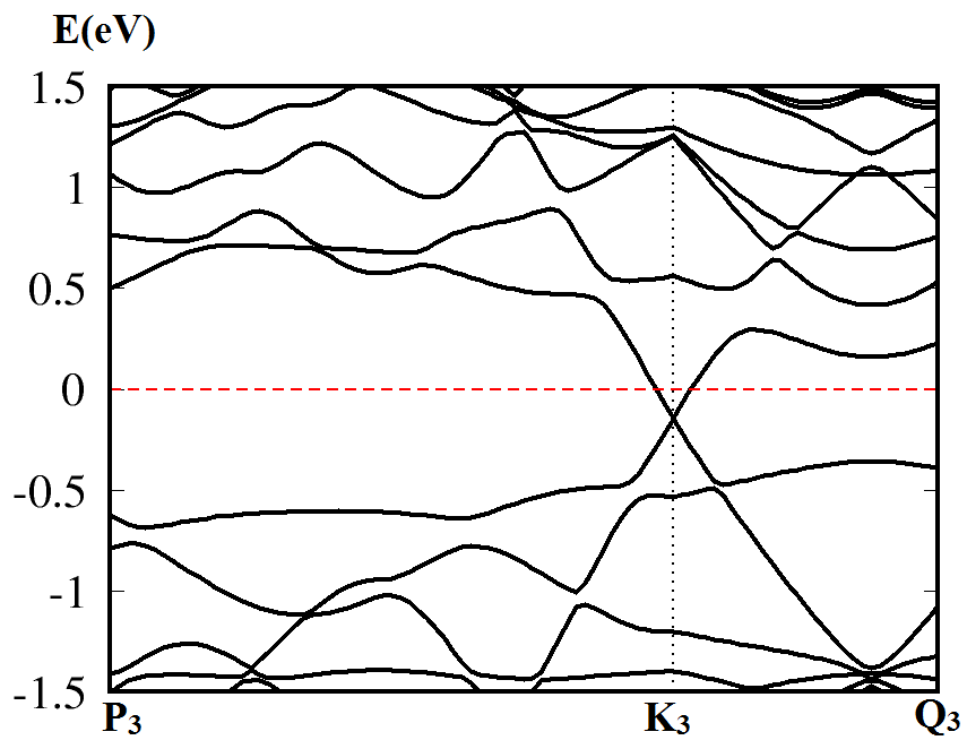


Figure 3.13 Band structure of turbostratic AA' stacking graphene on C face 3C-SiC(100)

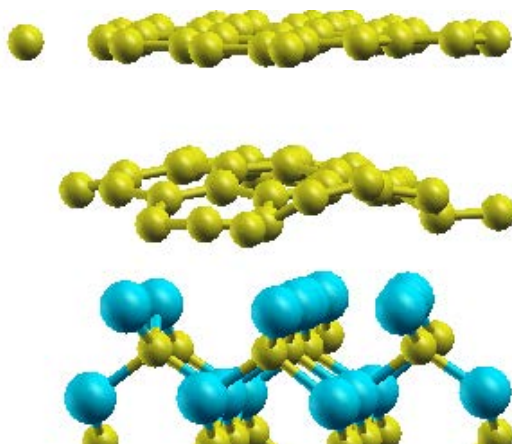


Figure 3.14 Optimized structure of turbostratic AA' stacking graphene on Si face 3C-SiC(100)

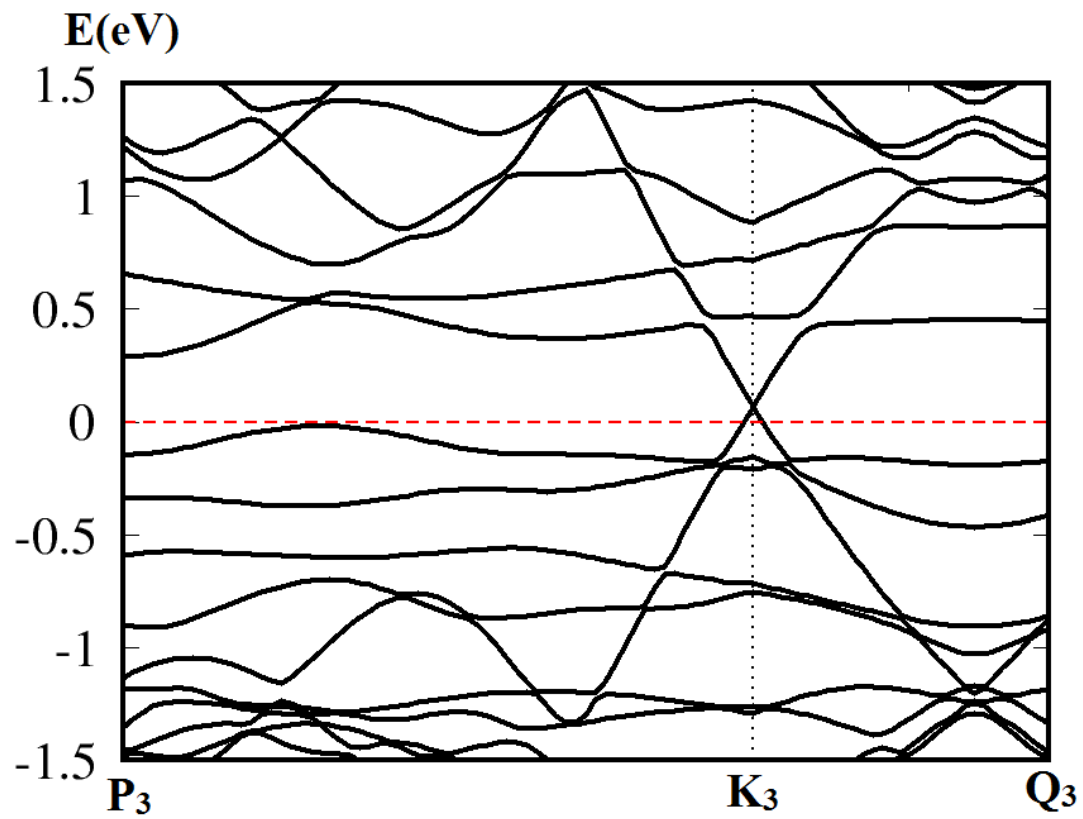


Figure 3.15 Band structure of turbostratic AA' stacking graphene on Si face 3C-SiC(100)

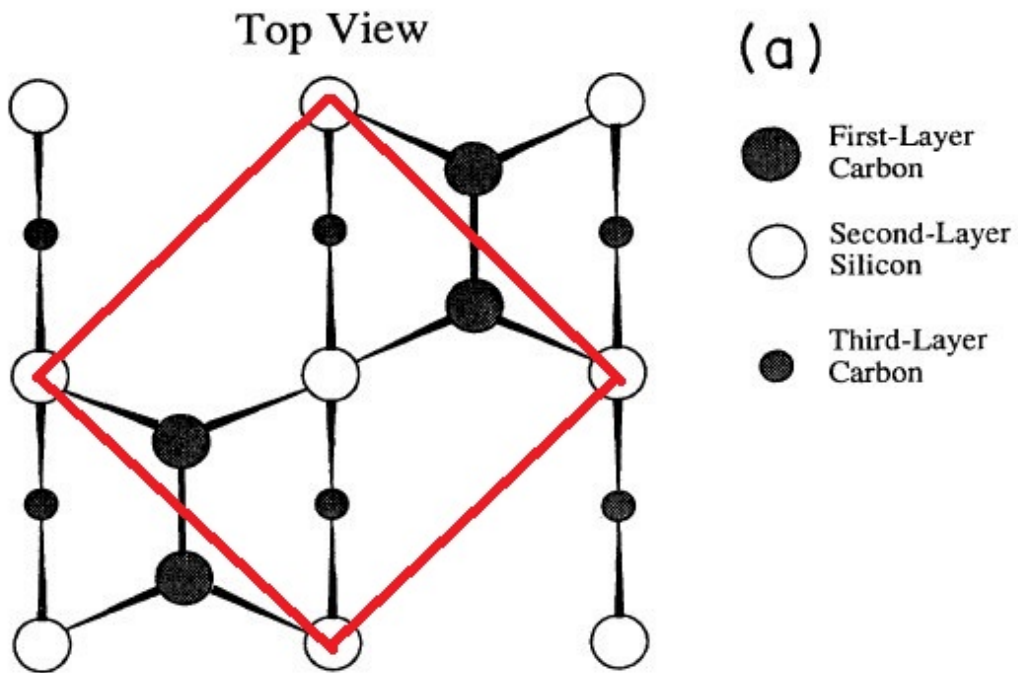


Figure 3.16 Surface structure of staggered dimer model 3C-SiC(100)-c(2×2) (J. M. Powers et al in 1991³⁶)

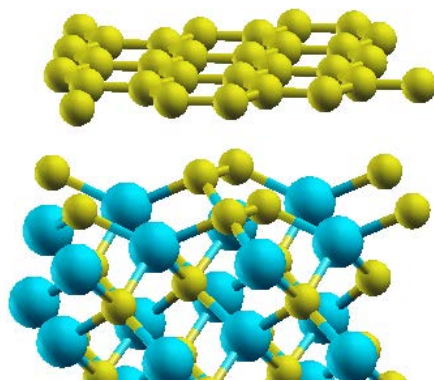


Figure 3.17 Optimized structure of monolayer graphene on staggered dimer model 3C-SiC(100)-c(2×2)

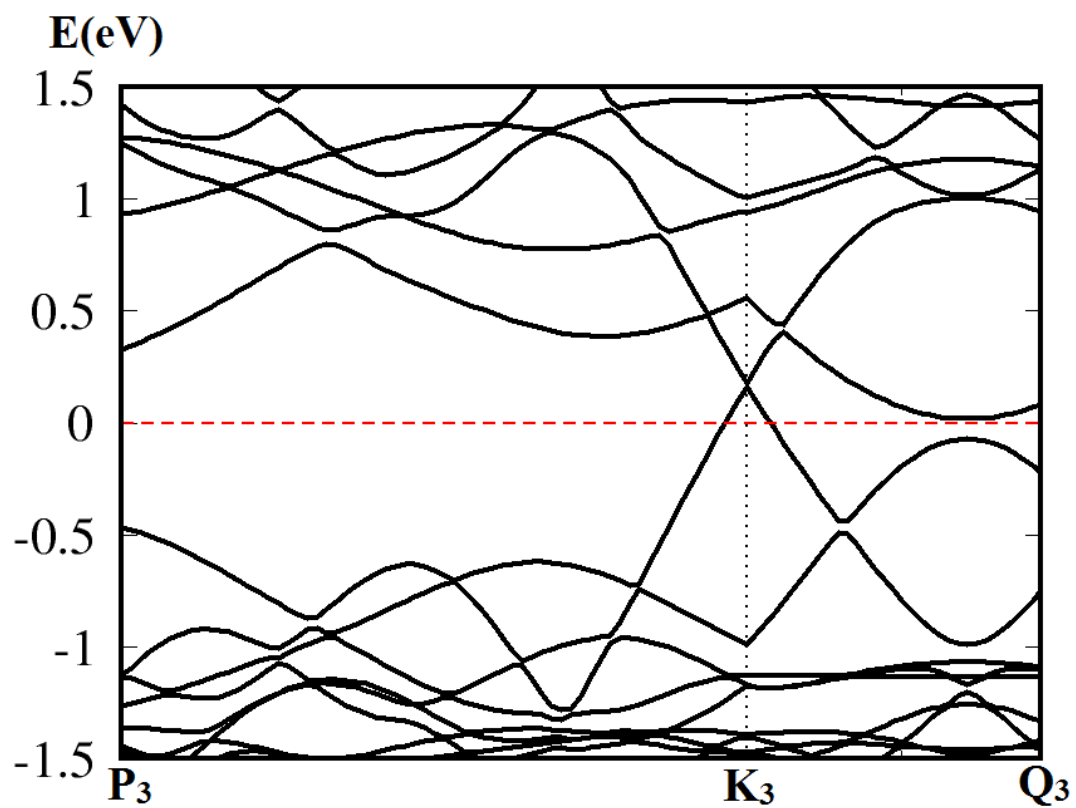


Figure 3.18 Band structure of monolayer graphene on staggered dimer model
3C-SiC(100)-c(2x2)

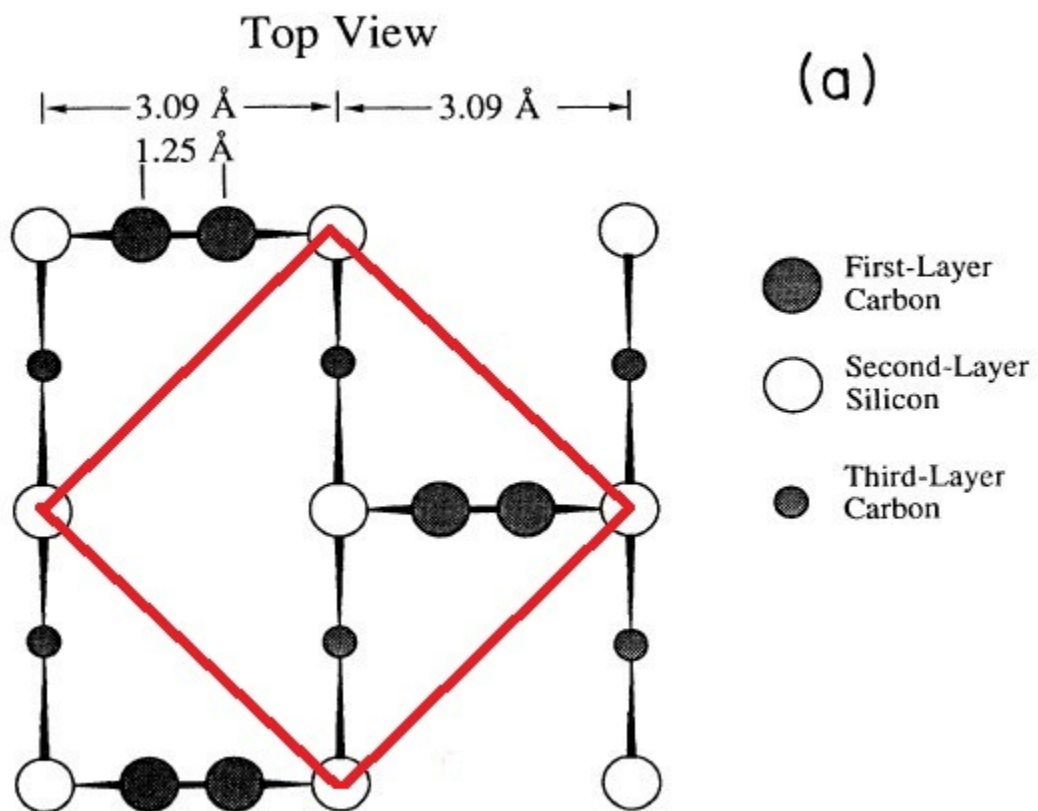


Figure 3.19 Surface structure of bridging dimer model 3C-SiC(100)-c(2×2) produced by C₂H₄ exposure (J. M. Powers et al in 1991)

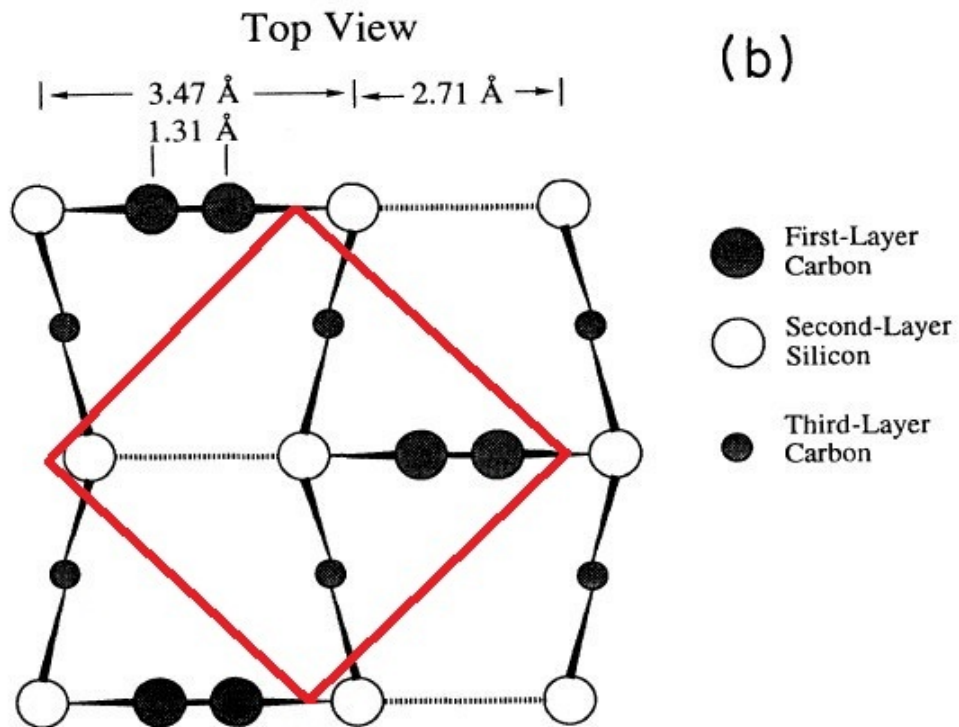


Figure 3.20 Surface structure of bridging dimer model 3C-SiC(100)-c(2×2) produced by Si sublimation (J. M. Powers et al in 1991)

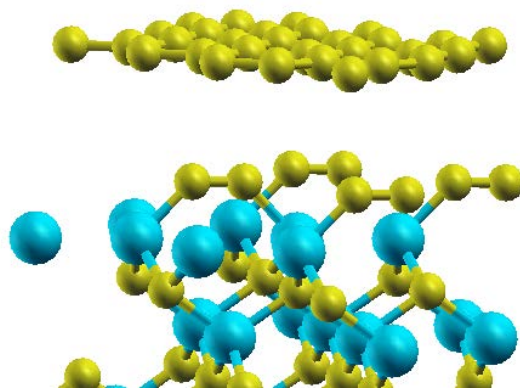


Figure 3.21 Optimized structure of monolayer graphene on bridging dimer model 3C-SiC(100)-c(2×2)

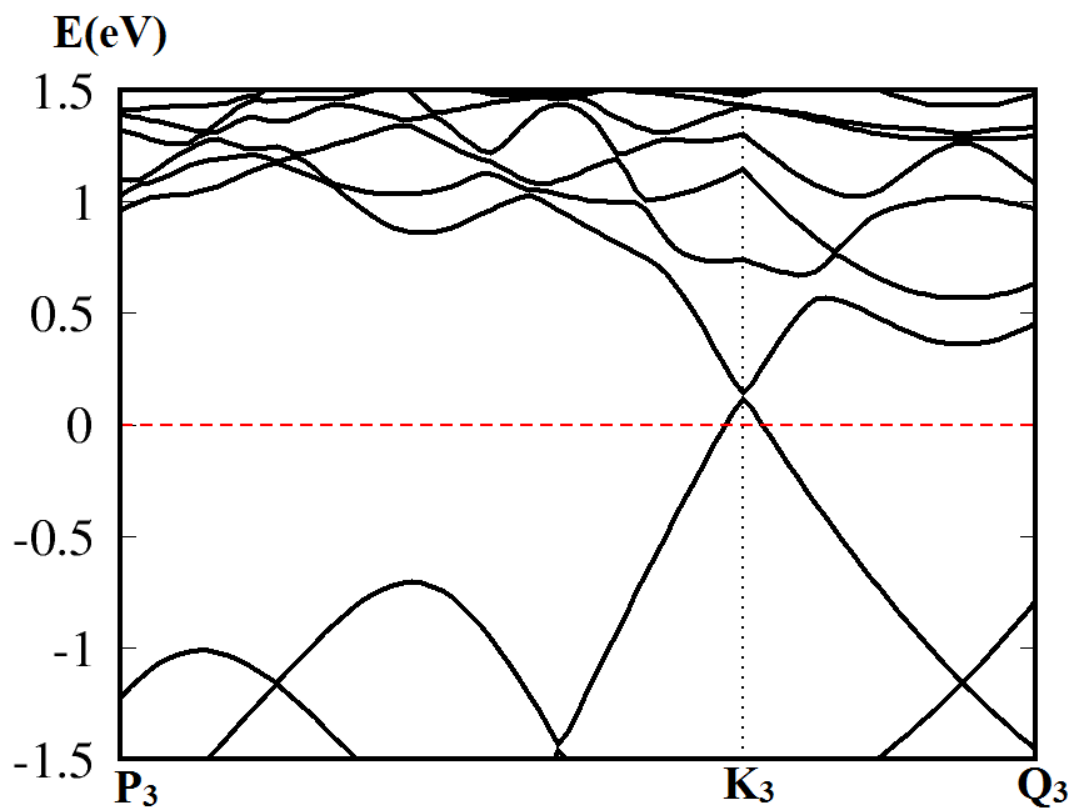


Figure 3.22 Band structure of monolayer graphene on bridging dimer model
3C-SiC(100)-c(2×2)

Chapter 4 Electronic Properties of Epitaxial Graphene on Silicon

4.1 Background

Graphene, with its outstanding properties such as nanoscale two dimensional nature, high carrier mobility and massless fermion dispersion, is one of the promising candidates of new generation nanoelectronics. Since graphene first prepared via micromechanical exfoliation by Geim et al in 2004³⁷, various fabrication methods have been developed. Epitaxial graphene growth on SiC strategy has the advantage not only in making large size (wafer size) graphene but also good for mass production and easy for further processing because of the insulating substrate. Epitaxial graphene on both Si and C faces of 6H-SiC has been extensively studied. The first carbon layer on 6H-SiC(0001) (Si face) acts as a buffer layer which covalently bonded to the substrate while the second carbon layer shows an n type doped graphene behavior. Investigation of graphene on 6H-SiC(000 $\bar{1}$) (C face), on the other hand, reveals a $(2\times 2)_c$ reconstructed surface. The single graphene layer on top has n type doped graphene-like band. Recently graphene grown on Si substrate has attracted interests from scientists since this method can be integrated into the conventional Si technology more easily and it has the ability to scale up graphene wafer size significantly. This fabrication can be achieved either via solid

source molecular beam or growth of the template layer such as 3C-SiC³⁸. In 2009 J. Hackley et al³⁹ reported the graphitic carbon growth directly on silicon using solid source molecular beam epitaxy. El-Shazly et al⁴⁰ also produced graphene on silicon by the thermal annealing of graphite in vacuum. A theoretical study is needed to investigate the geometric and electronic structure of graphene on Si and how the substrate interacts with the graphene sheet. In this chapter, we use ab initio method to study the graphene layer directly grown on reconstructed Si(111)-7×7 substrate and compare it with C layer on unreconstructed Si(111) surface.

Our results show that the first carbon layer on Si(111)-7×7 has a deep n doped graphene-like band, similarly to the graphene on 6H-SiC(000-1) case where there is no buffer layer. On the contrary, C on Si(111) is seriously distorted with ripple height more than 1 Å and no graphene-like band structure is found.

4.2 Atomic structure of reconstructed Si(111)-7×7 substrate

Investigations on the atomic structure of the Si surface is the first step to perform ab initio calculations and crucial to understand the interfacial interactions between substrate and graphene. A clean Si(111)-7×7 reconstruction is consistently observed as a starting surface in the process of graphitic carbon growth on silicon⁴¹ shown on the RHEED

image in Figure 4.1a. We therefore adopt reconstructed Si(111)-7×7 in dimer-adatom-stacking-fault (DAS) model as the substrate. (Figure 4.2) The Si(111)-7×7 reconstruction was one of the most complicated structures in surface science. Firstly proposed by Lander and Morrison in 1963, the surface model has evolved for 25 years until the current accepted DAS model was proposed by Takayanagi et al⁴² in 1985. In Figure 4.3, the lattice constant a of reconstructed Si(111)-7×7 is 26.95 Å which is essentially 7 times of Si(111) 1×1 cell. Along the edges of subunit there are 9 dimers in purple, which transforms the hexagons into pentagons. Silicon atoms in a dimer are double bonded. On top layer there are 12 adatoms in yellow. Each one is bonded to 3 atoms below and has one dangling bond. 6 atoms on the middle layer (formed by blue atoms) which are not bonded to the adatoms are called rest atoms. Each of the rest atoms has a dangling bond too. Also, in the big hole on the corner, one atom is missing which contributes another dangling bond for the atom on the lower layer. Together, 19 atoms count for 19 dangling bonds on the reconstructed surface. The stacking sequence of Si(111)-7×7 in the left triangular subunit is faulted (a/C) while the other half is normal (aB).

The dimension of graphene cell on Si(111)-7×7 substrate in experiment has not been reported yet. To commensurate with the substrate, we have done a few tests and found an

11×11 graphene cell has a minimal mismatch of 0.54% with the substrate, which results in a minor biaxial compressive strain. According to F Varchon et al⁴³ and our experience in doing graphene/3C-SiC(100) research in Chapter 3, such a small mismatch will not alter electronic properties of graphene much and a simulation of high accuracy is guaranteed. Also, the position of C atoms in graphene layer relative to the substrate might be arbitrary. We thus choose three different configurations with certain symmetry as illustrated on Figure 4.4.

4.3 Methodology

Theoretical calculations are performed using Quantum ESPRESSO package based on density functional theory (DFT). To better describe the vdW force for this layered system, we have used GGA(D)⁴⁴ which incorporates London dispersion forces with a 25 Ry energy cutoff. Although the system is large and computational cost is high, we build two additional Si bilayers under surface to let it show bulk effect rather than merely a thin film. A vacuum span of $\sim 12 \text{ \AA}$ is used to separate the slabs. Only Γ point of BZ is calculated since the system is so large that BZ is too small. However, the convergence is tested to be ensured. The geometry has been optimized to force less than 0.025 eV/ \AA .

4.4 Band structure of bare Si(111)-7×7 substrate

Before putting the graphene layer on top, we optimize the bare Si(111)-7×7 substrate first and compare its band structure with previous results by Jose Ortega et al⁴⁵. Figure 4.5 shows the band structure calculated by plane-wave LDA method. As shown in the inset the K path goes from Γ (center of BZ) to Q, halfway towards the corner, then it turns to the neighboring corner and turns back to Γ from the midpoint P. Each segment length in their plotting seems not be proportional to the real length in reciprocal space. We plot the band structure along the same K path with the correct length. The relative energy gap of bands is very similar and the general trend of bands is alike if we ignore the length ratio difference. This comparison of electronic structure guarantees that our construction of the complicated Si(111)-7×7 surface is consistent with the DAS model in literature.

4.5 Atomic and band structure of monolayer graphene on Si(111)-7×7 substrate

We place a single flat 11×11 graphene with C atoms on three different locations mentioned previously on the DAS model Si(111)-7×7 substrate and let the whole system relax. The initial distance between the graphene layer and Si adatoms from substrate is set

to be 2 Å. The optimization ends up with a bigger C and adatom mean distance Δ_0 of ~ 2.9 Å and a ripple with width up to ~ 0.6 Å is detected. The optimal geometries of three different configurations of C positions are shown in Figure 4.7 with layer spacing and ripple width in Table 4.1.

Table 4.1 Optimal geometries of different configurations of graphene on Si(111)-7×7

Configuration	Δ_0 (Å)	Ripple width (Å)
A	2.89	0.59
B	2.85	0.49
C	2.95	0.36

The band structures in Figure 4.8 are plotted along Γ -K-M in the BZ of the substrate. As K of graphene BZ coincides with K of substrate BZ, Figure 4.8 exhibits the behavior of epitaxial graphene near Dirac point. We find a clear band crossing with linear dispersion near K. Single layer graphene on Si(111)-7×7 substrate is deep n-type doped with Dirac point shifted by ~ 480 meV below Fermi level. The position of Dirac point varies slightly depending on the configurations as in Table 4.2 but the overall effect is the same. The interactions between the graphene and substrate are weak and make the graphene properties preserved. The $E_F - E_D$ value is bigger than the graphene on C face SiC case which is about 350 meV⁴⁶. The n-type doping is due to charge transfer from the substrate to graphene layer. Compared with graphene on C face SiC, because there are more dangling bonds per unit area, more charge transfers to graphene layer from

substrate per 1×1 graphene cell, which makes the graphene more n type doped. Our results are consistent with experiments of J. Hackley's group ⁴⁷ where the Raman measurement of carbon films grown on Si(111)- 7×7 shows D and G phonon modes which is the characteristic of graphene.

Table 4.2 Positions of Dirac point for different configurations of graphene on Si(111)- 7×7

configurations	$E_F - E_D$ (meV)
A	472
B	487
C	461

4.6 Atomic and band structure of monolayer graphene on unreconstructed Si(111) surface

To compare the results of single carbon layer grown on Si(111)- 7×7 surface, we investigated the single C layer on unreconstructed 7×7 cell of Si(111) with the same cell dimensions. The relaxation ends up with the distorted carbon layer as in Figure 4.9. Depending on the configurations of C plane, some parts where C atoms are initially closer to Si atoms are pulled towards the substrate while other parts where C atoms are initially far away are pushed away. The ripples have the height of 1.54 Å (Config. A) 1.26 Å (Config. B) 1.76 Å (Config. C) and width of ~ 27 Å. Unlike graphene on Si(111)- 7×7 ,

band structure plotted on unreconstructed Si as in Figure 4.10 shows numerous flat bands around Fermi level which come from surface states and no Dirac point is observed. The huge horizontal displacements of C atoms break the π bonds of ideal graphene and thereby making graphene characteristics completely disappear.

4.7 Origin of ripples on the graphene layer

We notice that the ripple of graphene on Si(111)- 7×7 is bigger than graphene on SiC previously studied and try to find explanations for this. The intrinsic asymmetric properties of the substrate contribute to the big ripple. As we previously described in Chapter 4.2, that the left triangular subunit is faulted while the other half is normal, the asymmetry of two halves of the substrate makes the surface uneven. As a result the optimal positions of the adatoms for the faulted half are higher than the normal half by approximately 0.1 Å. This induces a small wrinkle on the graphene layer because the left half is slightly higher than the right half. Also previous study shows that compressive strain on the graphene layer may induce significant ripple. To further confirm this, we construct a pseudo model with no strain on graphene for comparison. We keep the 1.42 Å C-C bond length of the optimal freestanding 11×11 graphene cell and increase the cell dimension of Si(111)- 7×7 cell to commensurate with it. After the structure is optimized,

we find the layer distance to be 2.89 Å, almost the same as the actual model with strain, while the ripple height becomes 0.37 Å, decreased by 37%. This demonstrates the compressive strain on graphene layer partially contributes to the ripple. The major contribution of ripple may come from the interaction between the substrate and the C layer. In summary, the asymmetric nature of substrate, compressive strain on graphene and the weak interactions on the interface are three factors that have great influences on the ripple length of graphene on Si(111)-7×7.

4.8 Conclusion

In conclusion, we performed ab initio calculation on monolayer graphene on Si(111)-7×7 and compared it with graphene on unreconstructed Si(111) surface. Our results show that the monolayer graphene grown on Si(111)-7×7 has deep n type doped graphenelike linear dispersion. The graphene layer also displays a great ripple with height up to 0.6 Å due to the asymmetric substrate, compressive strain and interfacial interactions. On the contrary, serious distortion is found on graphene layer grown on unreconstructed Si(111) as the strong interfacial interactions breaks the π bonds of ideal graphene. Thus no characteristics of electronic properties exist. This confirms with the experiments that Si(111)-7×7 is a more promising substrate than unreconstructed Si(111) for epitaxial

growth of graphene.

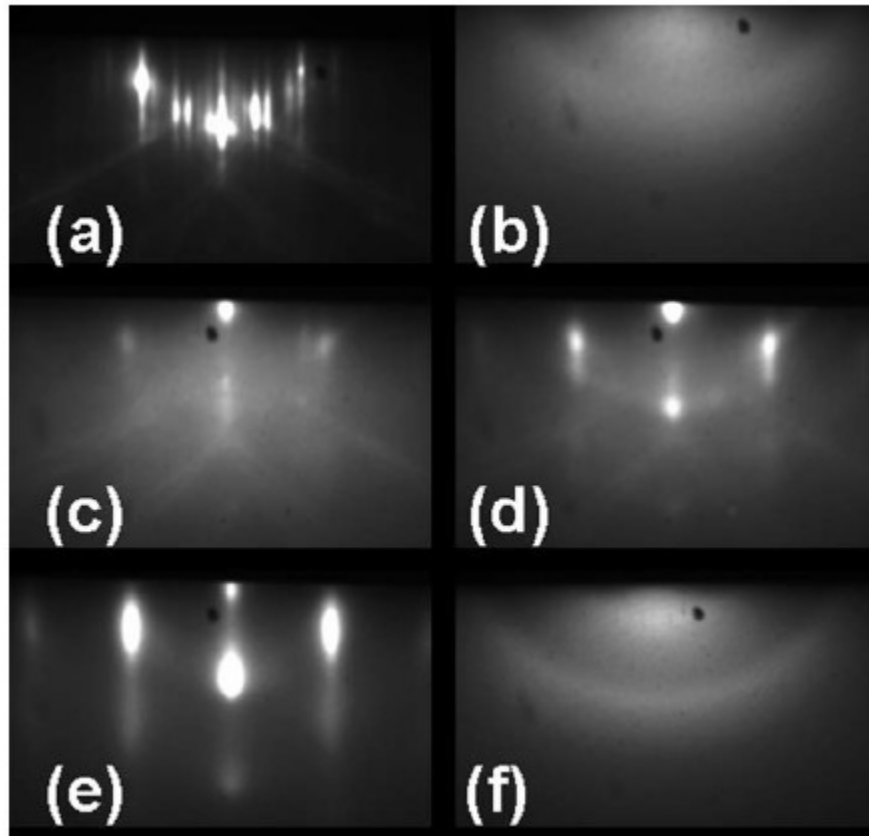


Figure 4.1 RHEED images acquired along the $\langle 110 \rangle$ crystal direction

(a) Si(111) 7×7 reconstruction of the starting surface following growth of the Si buffer layer; (b) *a*-C buffer layer at 560 °C; after carbon growth at 600 °C (c), 660 °C (d), and 700 °C (e) showing the formation of SiC; (f) broad rings indicate the polycrystalline structure of *g*-C after growth at 830 °C. (J. Hackley et al in 2009)

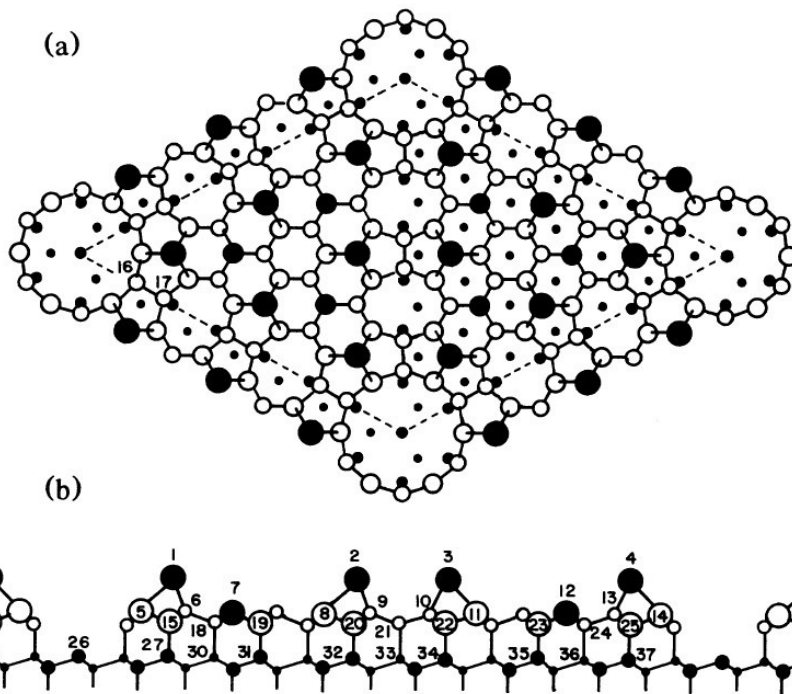


Figure 4.2 Crystal structure of Si(111)-7x7 in dimmer-atom-stacking-fault (DAS) model (Takayanagi et al⁴⁸)

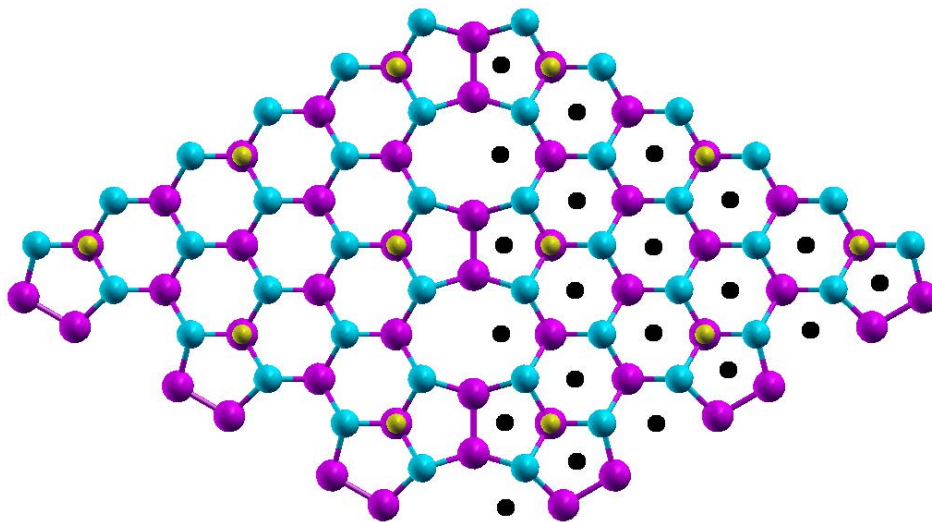


Figure 4.3 Unit cell of Si(111)-7x7 reconstruction in dimmer-atom-stacking-fault (DAS) model

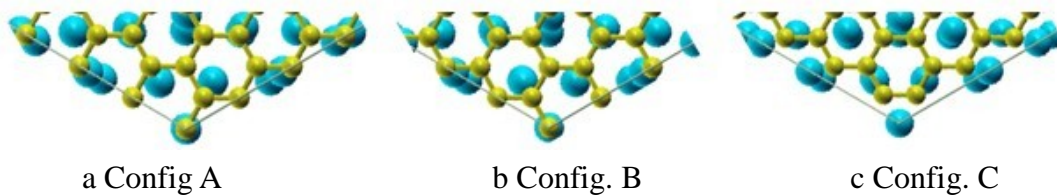


Figure 4.4 Three configurations of graphene on Si(111)-7×7 unit cell

- a A site carbon atom is above the Si at the corner of Si(111)-7×7 unit cell
- b B site carbon atom is above the Si at the corner of Si(111)-7×7 unit cell
- c center of the hexagonal ring is above the Si at the corner of Si(111)-7×7 unit cell

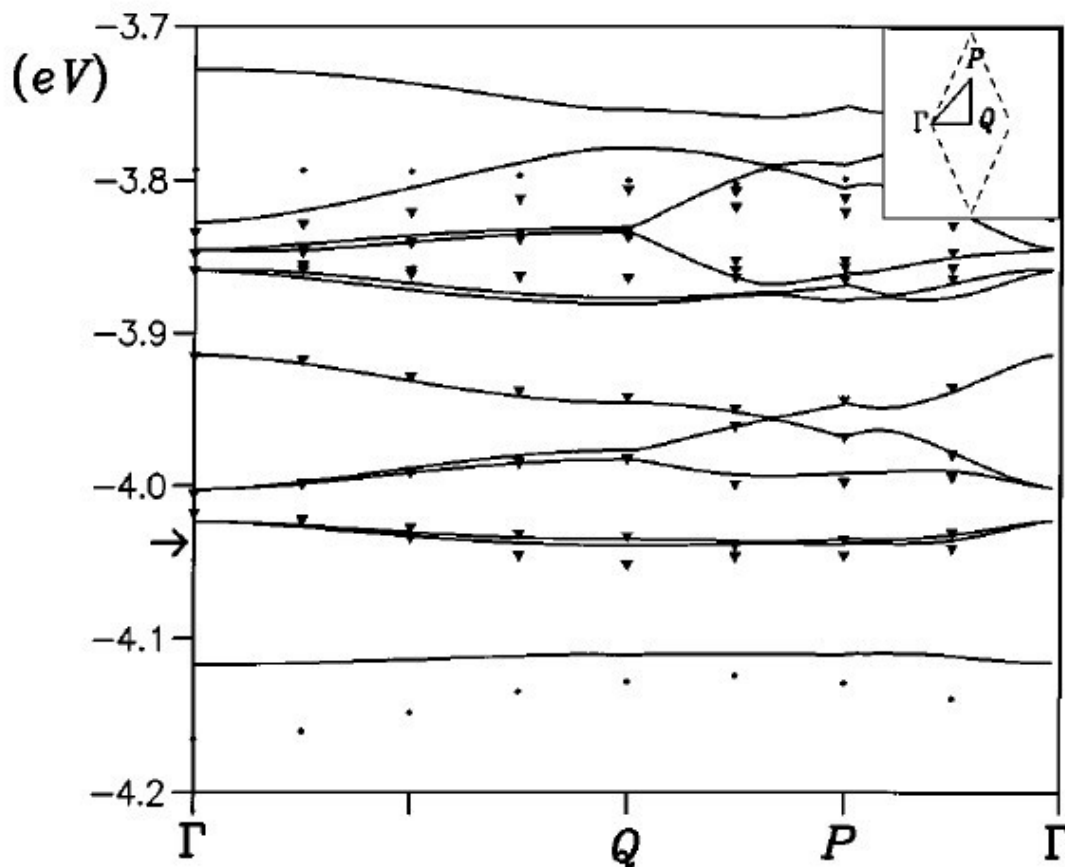


Figure 4.5 Surface band structure along the G-Q, Q-P, and P-G directions of the two-dimensional BZ (Jose Ortega et al⁴⁹.)

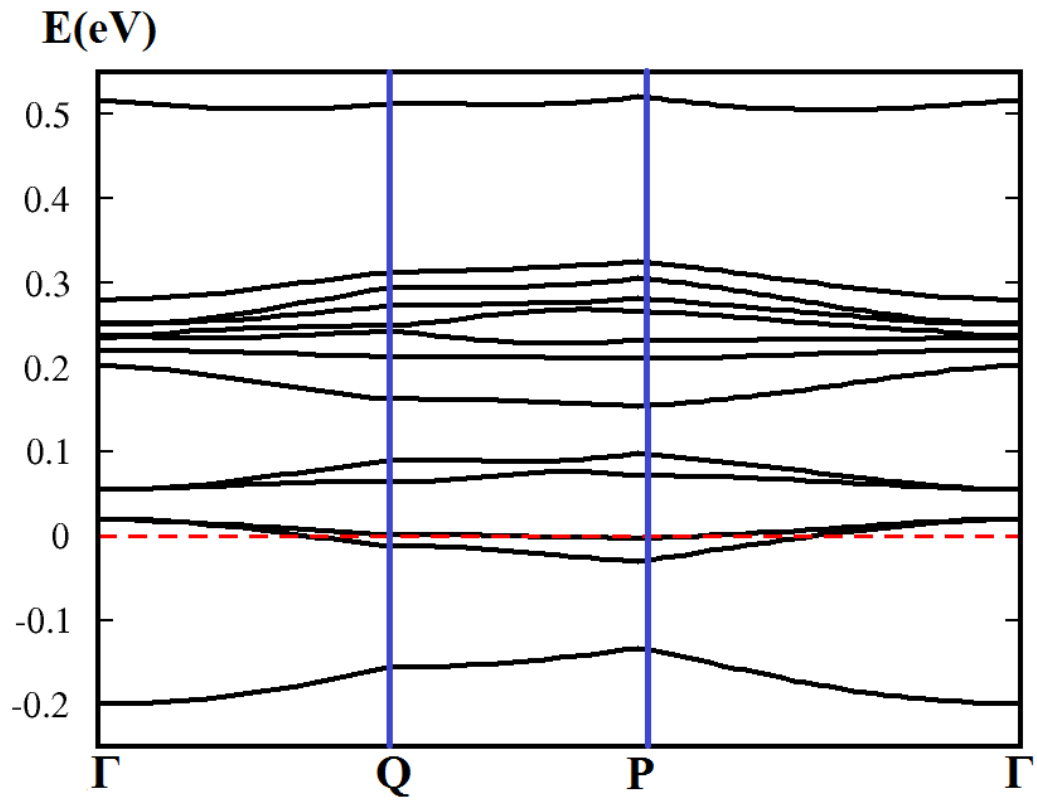
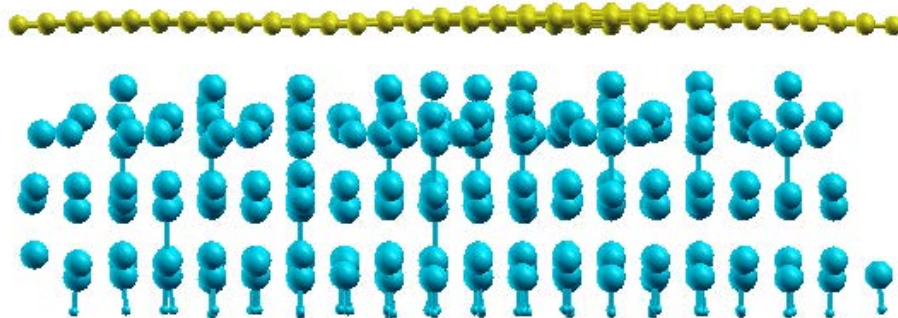
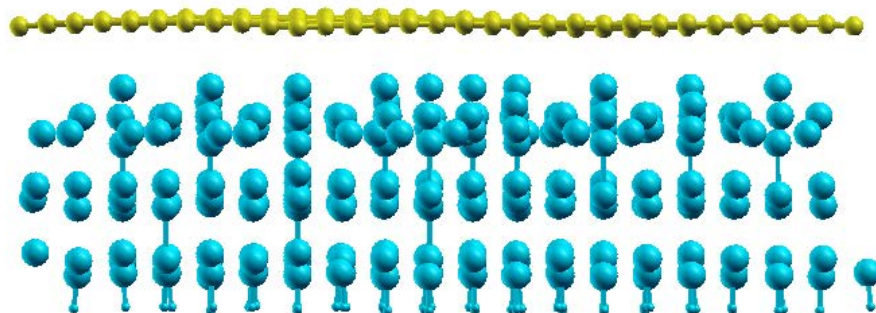


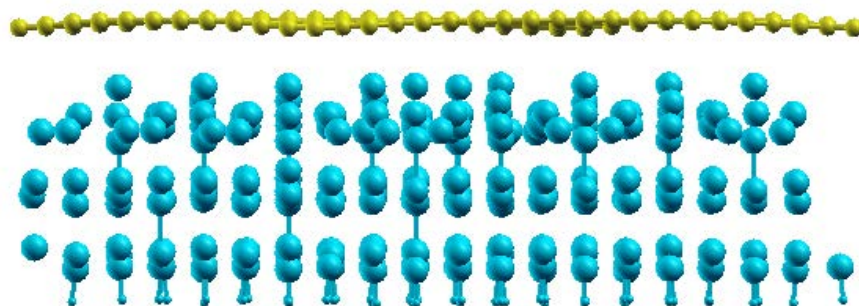
Figure 4.6 Surface band structure bare Si(111)-7x7 surface



a Config A



b Config B



c Config C

Figure 4.7 Optimal structures of graphene on Si(111)-7×7

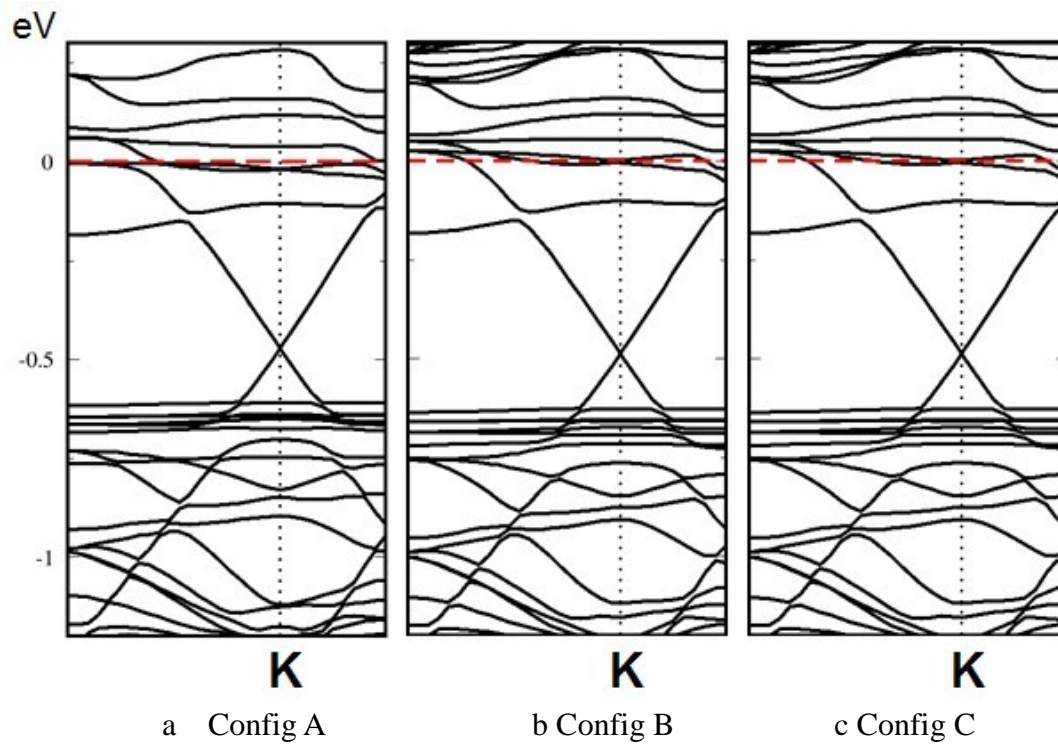
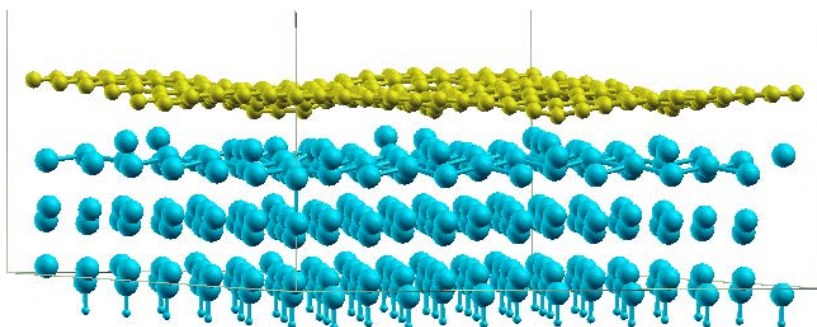
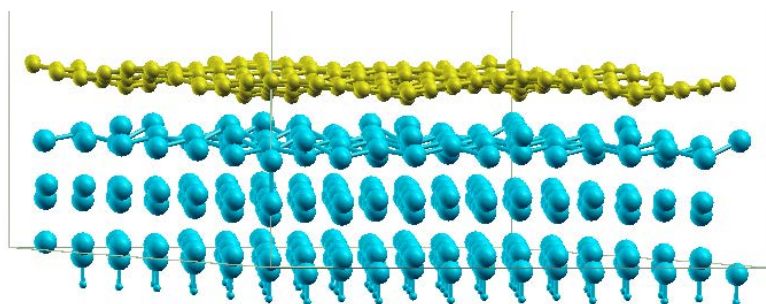


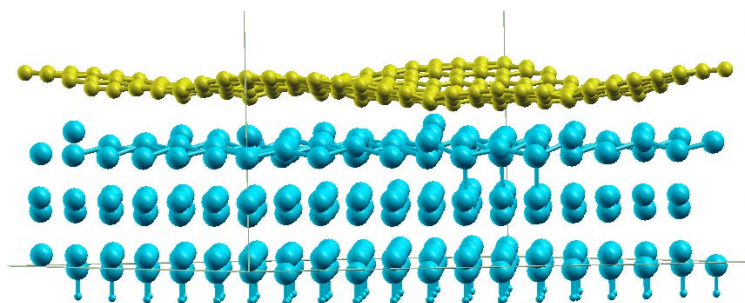
Figure 4.8 Band structures of graphene on Si(111)-7×7



a Config A



b Config. B



c Config. C

Figure 4.9 Optimal structures of graphene on unreconstructed Si(111)

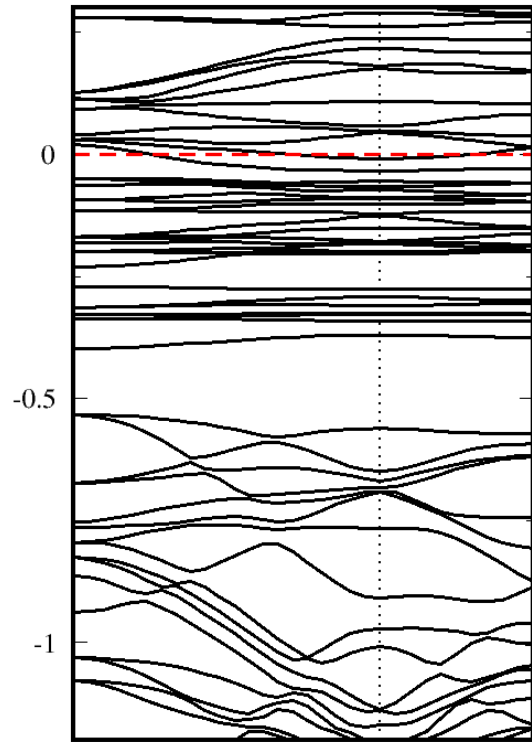


Figure 4.10 Band structures of graphene on unreconstructed Si(111)

Chapter 5 Water on Epitaxial Graphene

5.1 Background

Graphene, as a promising candidate of future nanoelectronic devices for silicon replacement, attracts attentions from physicists, chemists and material engineers. Both in the fabrication process and in the working status, graphene device is always exposed to the environment of air where water molecular is present. Therefore it is very interesting to investigate the influence of water on graphene. Also, graphene has potential application on sensitive gas detector which has been reported⁵⁰. Studies results of water on graphene can greatly extend the applications and functions of gas detector. The recent updates of research include inducing energy gaps in monolayer graphene by water molecule⁵¹, first-principles studies of water adsorptions on graphene on SiO₂⁵², etc.

The water on ideal freestanding graphene has been studied with local density approximation by R. M. Ribeiro et al⁵³. As in Figure 5.1 a low concentration of water is placed on top of ideal single layer of graphene, one water molecule per 2×2 supercell of graphene.

The band structure around K point in Figure 5.2 shows a small band gap (18 meV) is open and is shifted to one side of the K point. The vertical distortion of graphene caused by water breaks the A-B symmetry of graphene thereby inducing the small band gap. The discovery of energy gap induced by adding water molecule is significant but the model they used is too idealized because graphene without any substrate rarely exists and may not be able to describe the real situations in laboratory. Tim O Wehling et al investigate water adsorption on graphene on SiO₂ substrate. They find water adsorbates can shift the substrate's impurity bands and change their hybridization with graphene bands⁵⁴.

These works inspire us to study the influence of water on epitaxial graphene on 6H-SiC, which is closer to experiment and more practical. There have been few attempts to investigate the water on epitaxial graphene on SiC and it is therefore necessary to do so.

5.2 Calculation details

The possible orientations of water and its preferred binding sites were studied by many groups^{55,56}. As in Figure 5.3 five different orientations of water on three high symmetric sites: top of C atom, center of carbon hexagon, and middle point of C-C bond were studied and the binding energies were listed in the table in Figure 5.4. Every orientation

of water has its most energetically favorable site. It can be concluded from the comparison that for a given water orientation, center site a always has the lowest energy. Orientation I circumflex and IV O-down on center site a in Figure 5.5 are expected to have stronger influence effects on epitaxial graphene than other combinations because the dipole moments are orthogonal to the graphene surface and reach their maximal absolute values. We did the calculations for both single circumflex and O-down orientated water molecule on the monolayer epitaxial graphene on both Si and C face 6H-SiC, respectively.

For the Si face 6H-SiC, we use the 2×2 graphene super cell on the $\sqrt{3} \times \sqrt{3}$ 6H-SiC substrate mode. For the C face 6H-SiC, 5×5 graphene on 2×2 super cell of $(2 \times 2)c$ reconstructed SiC stated in Chapter 2 is used. We start with placing water at the equilibrium intermolecular separation R_e in Figure 5.4, which is the average distance between O and graphene surface, with H-O-H angle of 104.4° and let the whole structure relax.

5.3 Results and discussions

Table 5.1 Optimal geometries for circumflex water on graphene/ Si face SiC

Re	H-O-H angle	Ripple
3.19 Å	104.43°	0.006 Å

Table 5.2 Optimal geometries for O-down water on graphene/ Si face SiC

Re	H-O-H angle	Ripple
3.00 Å	106.04°	0.008 Å

Table 5.3 Optimal geometries for circumflex water on graphene/ C face SiC

Re	H-O-H angle	Ripple
3.04 Å	103.69°	0.20 Å

Table 5.4 Optimal geometries for O-down water on graphene/ C face SiC

Re	H-O-H	Ripple
2.95 Å	104.79°	0.20 Å

The optimized Re for the water on Si face SiC are closer to values in Figure 5.5 than C face SiC probably because for the graphene on Si face SiC case, the ripple is small and situation is more like an ideal graphene surface as in Figure 5.5 while in C face, a relatively big ripple width of 0.27 Å makes the difference greater. In fact, the water molecule reduces the ripple by ~0.07 Å for the graphene on C face SiC but does not change ripple width much for Si case. However, the overall trend is that the circumflex water tends to stay closer to the graphene layer and the total energy is lower than O-down

water on both graphene on Si and C face SiC cases. Also, the H-O-H angle for the circumflex water is greater than O-down water by $\sim 1^\circ$ for both cases.

We compute the band structures of graphene/SiC system without the water and after adding the water molecule. The shape of band structures stay similar after placing water on top but a minor shift of Dirac point happens. For graphene on Si face SiC face, circumflex water shifts the Dirac point downward by 3.1% of $E_F - E_D$ value making the graphene more n type doped while O-down water shifts the Dirac point towards the Fermi level by 1.5% of $E_F - E_D$ making the graphene less n type doped. For graphene on C face SiC, similarly, circumflex water shifts the Dirac point downward by 2.8% of $E_F - E_D$ value making the graphene more n type doped while O-down water shifts the Dirac point towards the Fermi level by 3.0% making the graphene less n type doped.

To further analyze the mechanism of the Dirac point shifting, we also calculate the charge density difference by subtracting the charge density of isolated graphene/SiC and isolated water from charge density of the water combined with graphene/SiC system. The plot on the right side of Figure 5.6-5.9 represents

$$N(\text{diff}) = N(\text{water on graphene}) - N(\text{graphene}) - N(\text{water}) \quad (5.1)$$

For the O-down water, the purple isosurface shows that by placing an O-down water molecule on top of graphene, more electrons cumulate above the graphene layer in one spot underneath the O atom. By placing a circumflex water molecule on top of graphene, however, the area above the graphene in the O-H extended line cumulate positive charges, meaning that area loses electrons. Unlike the O-down case, there are two areas instead of one because the 2 H atoms are closer to the surface. The overall effects from the circumflex and O-down water are opposite thereby shifting the Dirac points towards opposite directions. The dipole of the polar water molecule makes the electrons on the graphene surface redistribute and the charge redistribution shifts the Dirac point.

5.4 Conclusion

To conclude, the water on graphene/SiC has a large equilibrium intermolecular separation around 3 Å with graphene surface therefore it has a small interaction with graphene. No strong bond is formed and electronic properties of graphene/SiC are not obviously altered. The intrinsic dipole of polar water molecule induces the redistribution of charges on the graphene surface which shifts the Dirac point.

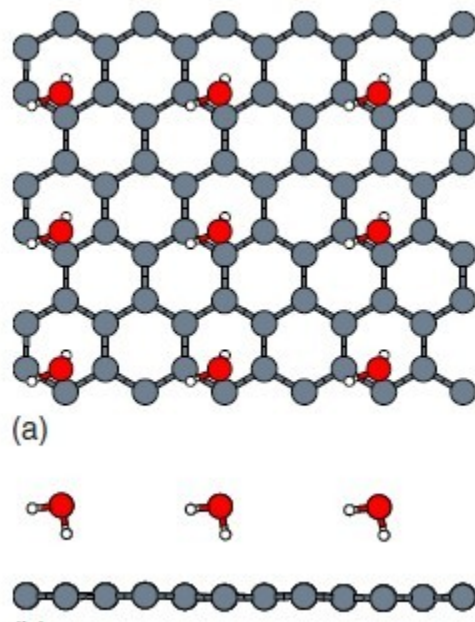


Figure 5.1 Crystal structure of water on freestanding graphene

(R. M. Ribeiro et al⁵⁷)

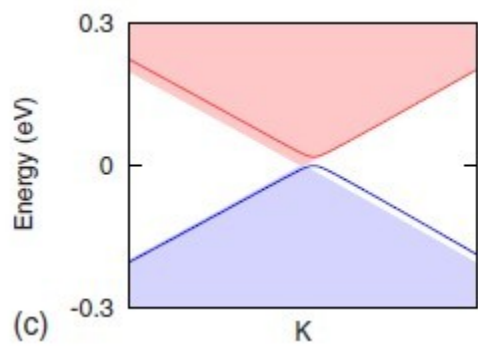


Figure 5.2 Band structure of water on freestanding graphene near Dirac point

(R. M. Ribeiro et al)

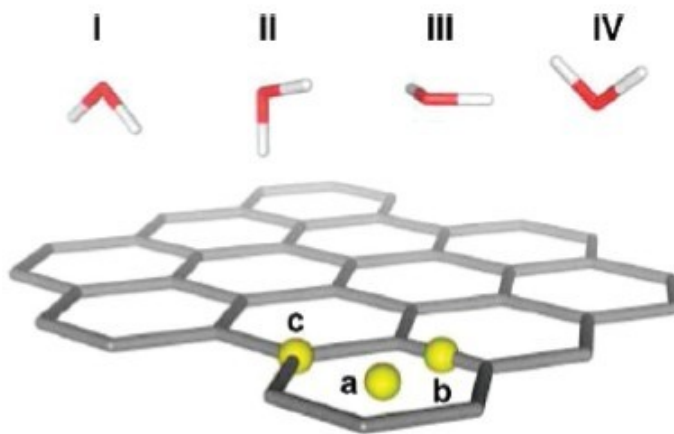


Figure 5.3 Five water orientations and three sites

(Miroslav Rubes et al ⁵⁸)

structure ^a	graphene	
	R_e	E_{int}^b
Ia	3.26	-13.3 (-1.1)
Ib	3.34	-12.0 (-0.6)
Ic	3.32	-12.4 (-0.9)
IIa	3.35	-11.4 (-1.4)
IIb	3.35	-11.9 (-2.0)
IIc	3.35	-12.1 (-2.1)
IIIa	3.12	-10.0 (0.4)
IVa	3.01	-8.7 (-0.1)

Figure 5.4 Equilibrium intermolecular separation R_e and energy for different water on graphene configurations

(Miroslav Rubes et al)

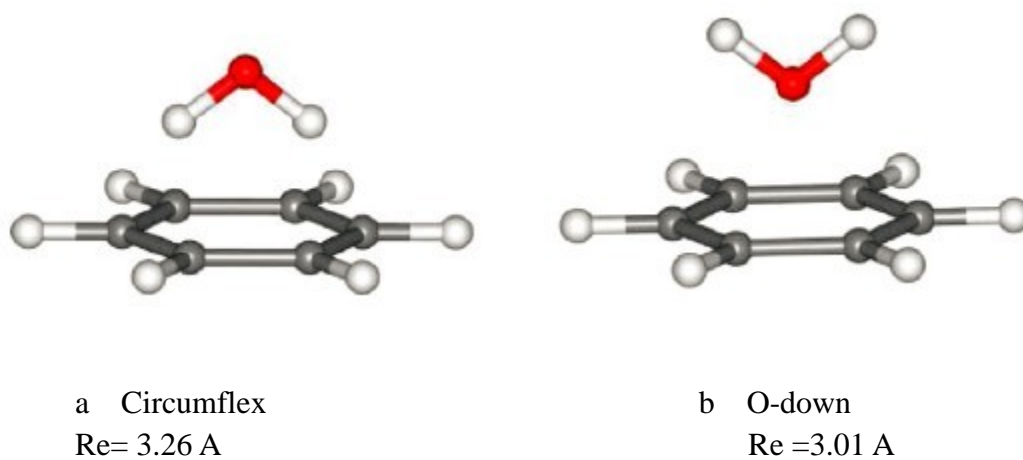


Figure 5.5 Two configurations of water on graphene

(Miroslav Rubes et al)

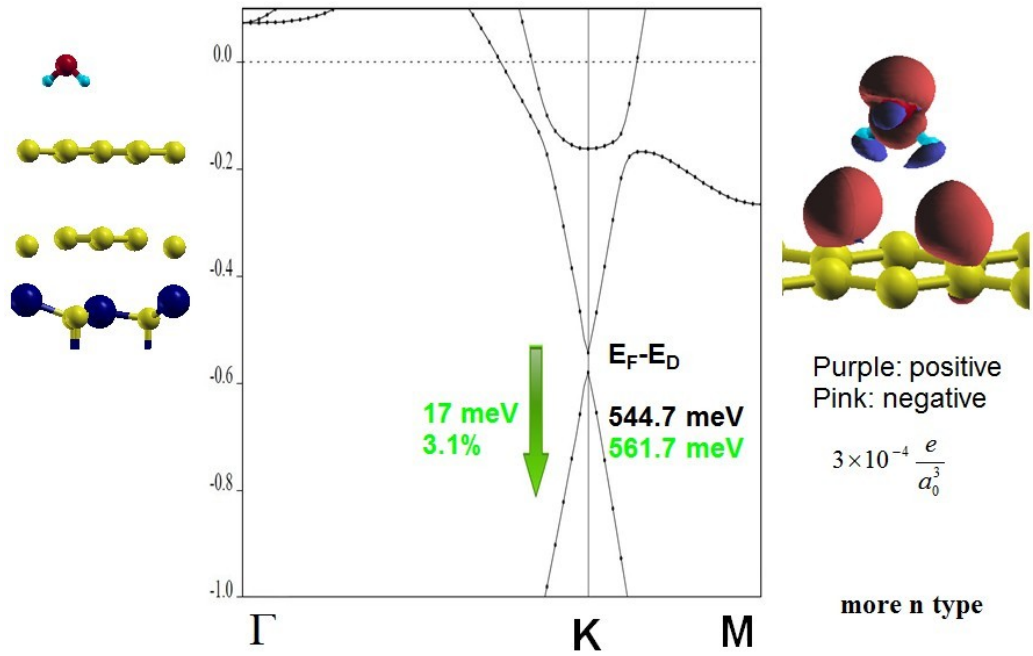


Figure 5.6 Atomic structure, band structure and charge difference for circumflex water on graphene/ Si face SiC

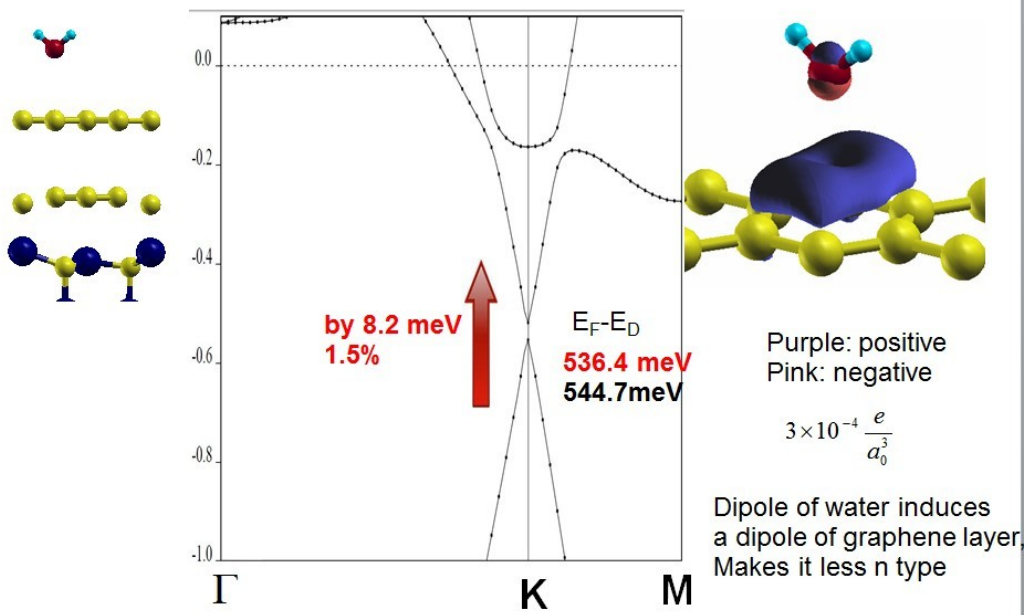


Figure 5.7 Atomic structure, band structure and charge difference for O-down water on graphene/ Si face SiC

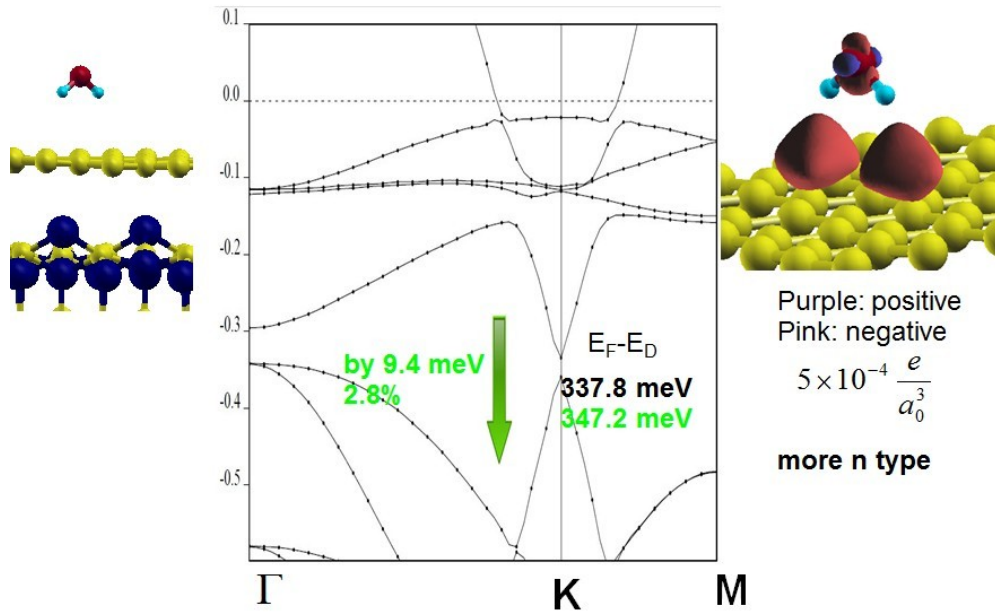


Figure 5.8 Atomic structure, band structure and charge difference for circumflex water on graphene/ C face SiC

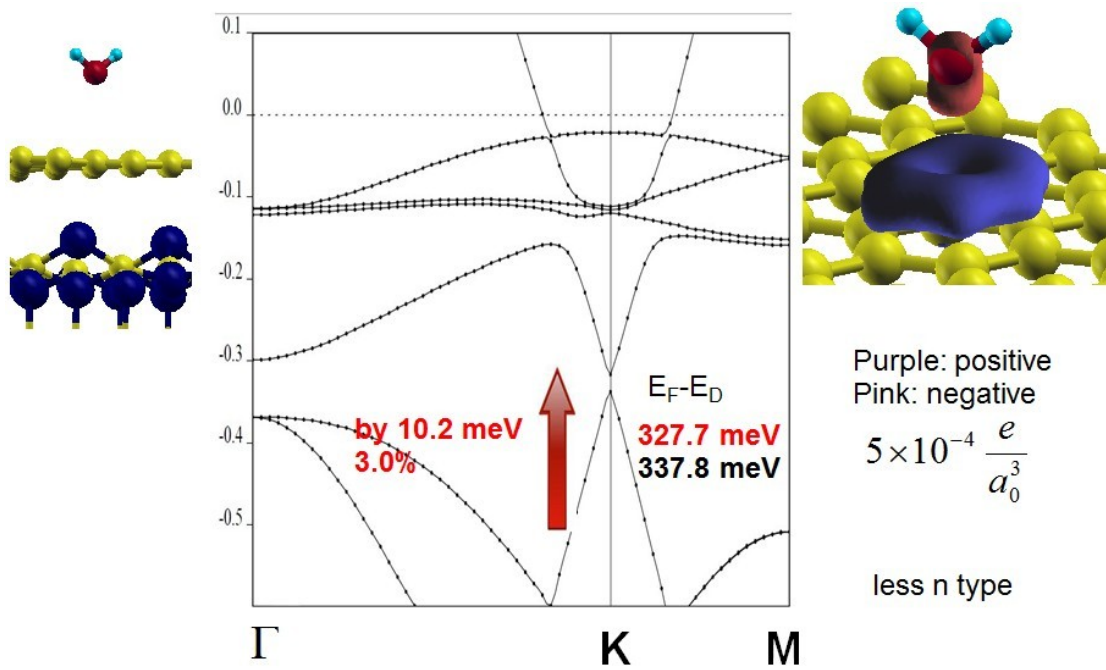


Figure 5.9 Atomic structure, band structure and charge difference for O-down water on graphene/ C face SiC

Chapter 6 Raman spectra in graphene

6.1 Raman spectra applications

The Raman scattering spectroscopy is a technique which can be used to study the vibration modes in crystal. The incident laser light interacts with molecular vibrations, phonons or other excitations in the system, resulting in the energy of the laser photons being shifted up or down. The shift in energy gives information about the vibration modes in the system. Raman spectra have played an important role in studies of properties of graphene since 2004. It has succeeded in distinguishing monolayer from few-layer graphene samples, determining the amount of doping and percentage of disorder, investigating graphene edge's effects, etc. By analyzing the shape and frequency shift of the Raman band, scientists can determine the number of layers of graphene sample and other characteristics on graphene surface. Both Raman frequency and intensity can be computed from DFT using the method as I explained in Chapter 1.1.8.

6.2 Phonon dispersion of graphene

To interpret the Raman shift of graphene, graphene phonon dispersion should be studied because it has essential relationship with it. The primitive cell of graphene contains two

carbon atoms in A and B sites which results in 6 phonon branches as N atoms in a cell have 3N phonon modes. Three of them are acoustic (A) phonon modes and the other three are optic (O) modes. The vibrations can be in-plane (i) or out-of-plane (o), longitudinal (L) or transverse (T) with respect of the C-C bond direction. Figure 6.1 is the calculated phonon dispersion relation of an ideal graphene sheet with all phonon branches marked with vibrational mode. In BZ center Γ , double degenerate optic modes iLO and iTO are Raman active according to Group Theory.

6.3 Raman scattering in graphene

Figure 6.2 shows a Raman spectrum of a graphene edge displaying the main Raman features D, G, G' bands by L.M. Malard et al. Of all the feature bands, G is the most distinguished feature band in the Raman spectrum of monolayer graphene. It is associated with the double degenerate optic modes iLO and iTO in Figure 6.1 with experiment frequency around 1582 cm^{-1} . Although it appears to be one single peak, it is actually made of two peaks superimposed together as each peak is originated from an optic mode. Because of the degeneracy, these two peaks have the same frequency and they end up with a peak with single frequency value. More important, it is the only band originated from a first order Raman scattering process in graphene and the only band which can be

directly computed by DFT so far. Other features like D, D' and G' come from a second order Raman scattering process which involves two phonons and they are hard to calculate from first principles. In experiment, measurement of G' can be analyzed by Lorentzians to determine the number of graphene layers. However, from the computational point of view, G band is our main focus. The G band corresponds to the two degenerate optic modes with frequency of 1582 cm^{-1} . G band is the most prominent features in Raman spectra of monolayer graphene. The other features D, D' and G' originated in second-order Raman scattering which cannot be computed from DFT directly so we focus merely on G peak.

6.4 Raman spectra of monolayer graphene under uniaxial strain

Strain makes atoms in crystal compressed or stretched of equilibrium positions and widely exists in practical situations. Strain can change the properties of graphene, especially the phonon properties. Sometimes, strain is intentionally applied to improve mobility in silicon technology. Recently a few experiments show the characteristics of Raman shift of graphene under uniaxial or biaxial strain. It is therefore necessary to do DFT calculations to understand the strain effect on Raman spectra.

In recent years, T.M.G Mohiuddin et al⁵⁹ have studied the Raman spectrum of graphene as a function of uniaxial strain. They induce the strain up to ~1.3% controllably by depositing a graphene layer on two flexible substrates and bending the substrates. They find from Raman measurement that the doubly degenerate E_{2g} optical mode splits into two bands as in Figure 6.3. A linear fit of the frequency vs. strain plotting in Figure 6.4 demonstrates a linear relation between the magnitude of uniaxial strain applied and the frequency shift of both splitting peaks G⁺ and G⁻. Furthermore, they investigate the polarization dependence of G⁺, G⁻ intensities. They conclude that one splitting peak is polarized along the strain, the other perpendicular. The other group Mingyuan Huang et al,⁶⁰ have done similar studies by supporting graphene on a flexible substrate. They have detected G peak splitting and both bands exhibit significant redshift linearly with strain. In addition, they claimed the polarization dependence of the Raman response can be used for an accurate determination of the crystallographic orientation. Because of significant applications on measuring strain dependence of Raman active phonon, we realize it is necessary to carry out a thorough calculation from first principles to compare and verify experiments. Although in 2009, T.M.G Mohiuddin did first-principles calculations to support their own experiments, those calculations are only limited to coefficient of frequency shift with respect to strain. In addition to this, we have used our own model

independently calculated the complete G band vs. strain and polarization Raman plotting that have never been done before.

6.5 Methodology

Theoretical calculations are performed using Quantum ESPRESSO package based on density functional theory (DFT). LDA is used with a 80 Ry energy cutoff. A vacuum span of ~ 12 Å is used to separate the slabs. We have used a $12 \times 12 \times 1$ Monkhorst-Pack K grid in the Brillouin zone. The convergence is tested to be ensured.

We define zigzag edge as x direction and armchair edge as y direction as in Figure 6.5. The primitive cell we construct contains two C atoms in site A and B as normal. However, instead of hexagonal structure, we choose monoclinic P Bravais lattice because this choice gives us an extra degree of freedom for the strain. We adopt C-C bond length of 1.406 Å as the theoretical value when graphene is under zero strain by minimizing the total energy of the whole structure for the pseudopotential we choose. The corresponding cell vector length is a_0 ,

We define

$$\varepsilon_x = \lambda_x - 1 \quad (6.1)$$

$$\varepsilon_y = \lambda_y - 1 \quad (6.2)$$

Where ε_x and ε_y are the strain in x and y directions, respectively and the following geometric relations in the lattice can be derived.

$$|\mathbf{a}_1| = \lambda_x a_0 \quad (6.3)$$

$$|\mathbf{a}_2| = \frac{1}{2} \sqrt{1 + 3 \left(\frac{\lambda_y}{\lambda_x} \right)^2} |\mathbf{a}_1| \quad (6.4)$$

$$\cos \langle \mathbf{a}, \mathbf{b} \rangle = - \frac{1}{\sqrt{1 + 3 \left(\frac{\lambda_y}{\lambda_x} \right)^2}} \quad (6.4)$$

$$y_B = \frac{\sqrt{3}}{3} \lambda_y a_0 \quad (6.5)$$

Eq(6.3), Eq(6.4) and Eq(6.5) give the length of vectors and the angle between them while y_B is the y coordinate of C in site B. From (6.3) and (6.5) we see that strains on x and y directions be can adjusted by factor λ_x, λ_y independently.

We set ε_x from 0 up to 3% with 0.5% increment. Positive value means graphene is stretched out in x direction. For a given ε_x we optimize the system by adjusting ε_y to ensure graphene has global minimum energy. The optimal ε_y we get is negative meaning minor compressive strain in y direction. However, as the absolute value of ε_y is always smaller than ε_x by one order. The effect of stretch strain in x direction is dominating.

6.6 Linear dependence of G shift with strain

We get the series of Raman plotting in Figure 6.6 with G peaks of increasing strain denoted in different color. G peak splits into G^+ and G^- . It is easily observed that both of them redshift as strain increases. Compared with Figure 6.3 our calculated plotting has similar tendency. To quantify the G peak splitting, we accurately locate the position of G^+ , G^- peaks and plot them with respect to strain in Figure 6.7. Then linear fitting is used to compute the slope. The values of slope are quite different from those in literature because our model differs with experiment setup. We adopt an ideal freestanding graphene layer while in experiment, graphene layer is suspended on the substrate and a conversion associated with substrate Poisson's ratio is needed. Besides, the direction of strain in experiment is unclear thus we are unable to compare the slopes. However, the general tendency of our results is consistent with experiment data: a) a redshift with strain for both G^+ and G^- and b) the G^- slope is steeper than G^+ .

The G splitting has an approximately linear dependence on the strain magnitude in both x and y directions with different slope. The value of G^+ G^- frequency and their slope with strain can be used to determine the magnitude of strain and its orientation.

6.7 Polarization dependence of G peak

Both groups have observed the polarization dependence of the G bands as in Figure 6.7.

In Figure 6.4, if we change the angle theta between incident light and x, the intensity of

G^+ and G^- has a sine function relation with θ but G^+ and G^- has a phase deference is $\pi/2$.

Figure 6.9 shows the polarization dependence. We calculated the G^+ and G^- intensity in the range of theta 0-360° with 1.5% strain in x direction and the results demonstrates the same effect as in Figure 6.9 .This polarization dependency can be used to determine crystallographic orientation with respect to strain.

6.8 Raman spectra of graphene on Si face SiC

All previous calculations in this chapter were performed in the ideal monolayer graphene.

The Raman spectra properties of graphene G peak are studied. It is more interesting to calculate the G peak in epitaxial graphene because that is one of the most important fabrication approaches of graphene in reality.

For this purpose, we have studied the Raman spectrum of graphene on Si face SiC. This kind of phonon calculations require huge CPU time because it involves large number of atoms and phonon modes. The computation of Raman shift of the unstrained 13×13

model is not realistic for us to complete. Therefore we use the well-known $\sqrt{3} \times \sqrt{3}$ model where the electronic properties of graphene are preserved. Even in this simplified mode where atoms number is greatly reduced, it takes several weeks to complete. From Figure 6.10 we clearly see P1 is dominating. Its intensity and FWHM are greater than other peaks by orders of magnitude. Unlike the band structure where only the slope of linear dispersion is altered, the G peak frequency 1111.3 cm^{-1} differs from the experiment value of 1582 cm^{-1} . This is because phonon frequency is very sensitive to the lattice constant. Compared with monolayer graphene under the same 8% strain, P₁ shows same vibrational mode and frequency with G of graphene. The frequency difference is negligible. This confirms that the substrate does not change G peak position. We can infer this rule applies to the real case where epitaxial graphene is unstrained. Besides dominating G peak, we find P₂ with frequency of 643 cm^{-1} is associated with out-of-plane phonon mode of buffer layer. It can be used to detect if epitaxial graphene has a buffer layer. Contributions of P₃ come from both buffer layer and H atoms.

6.9 Conclusion

We have calculated Raman spectra of monolayer graphene as a function of strain from first-principles. G splitting and linear relations with respect of strain is found to be

consistent with experiment. Furthermore, Raman spectra of graphene on Si face SiC is calculated.

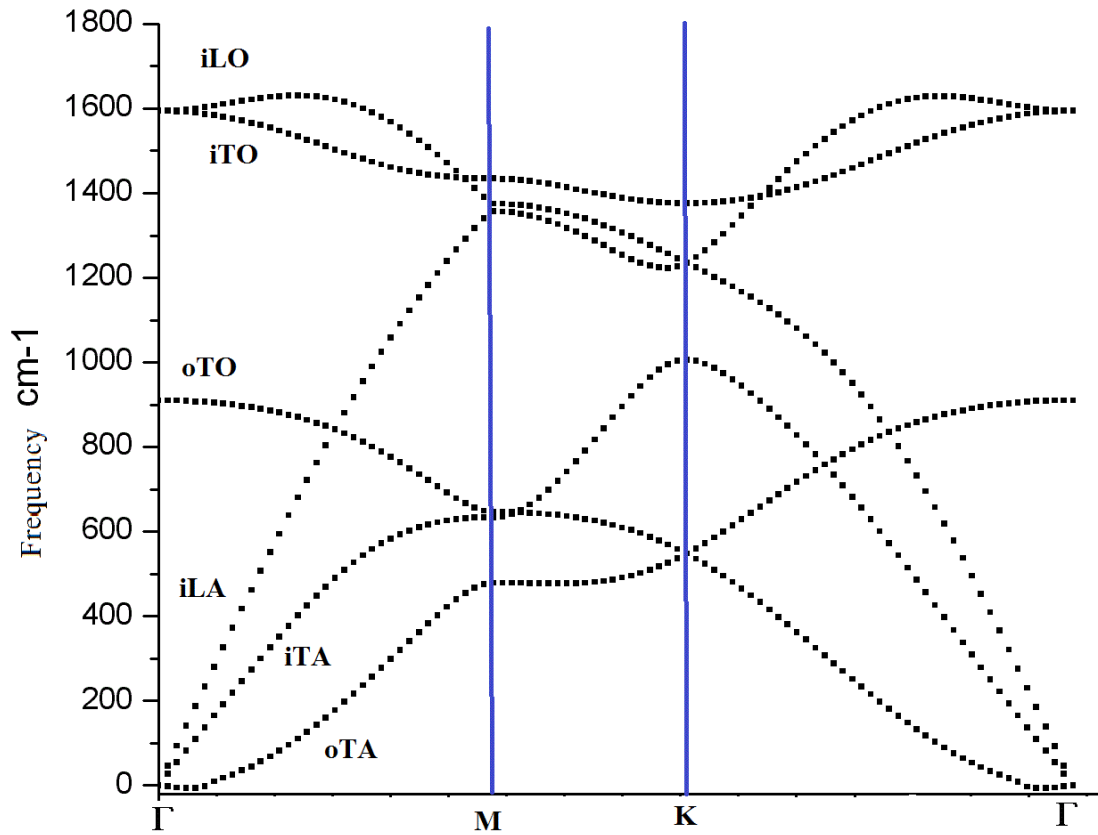


Figure 6.1 Phonon dispersion of monolayer freestanding graphene

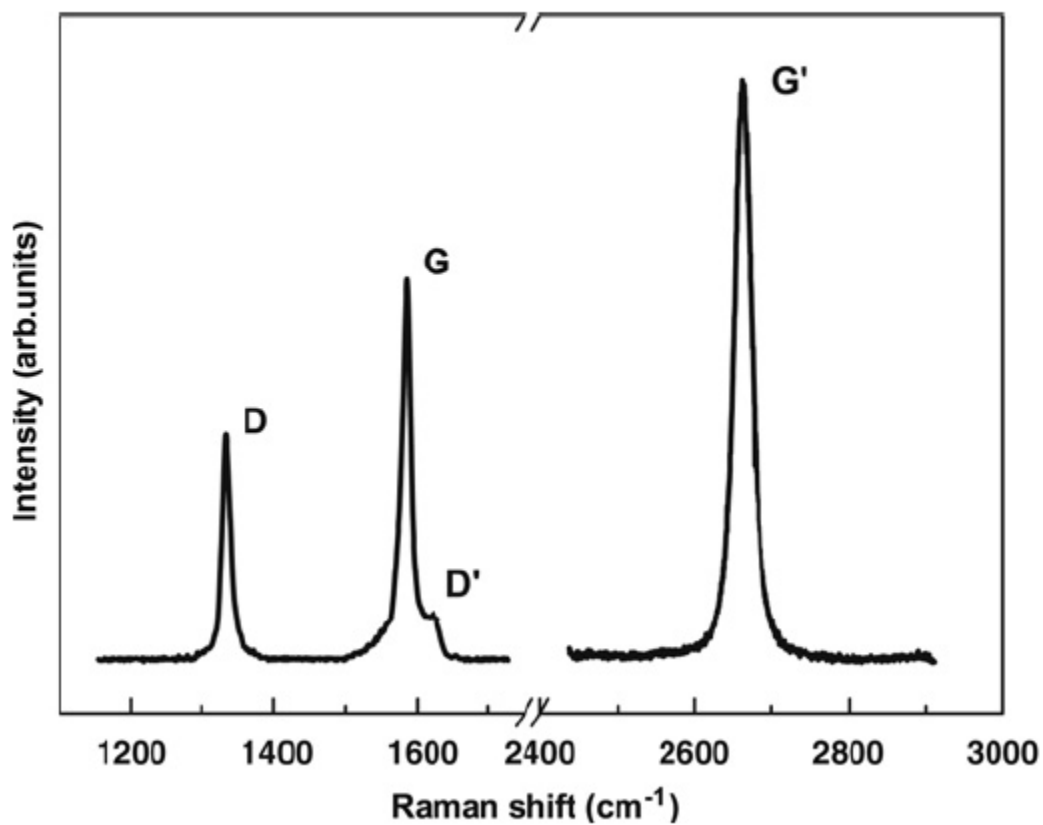


Figure 6.2 Raman spectrum of a graphene edge, showing main Raman features, the D, G and G' bands taken with a laser excitation energy of 2.41 eV

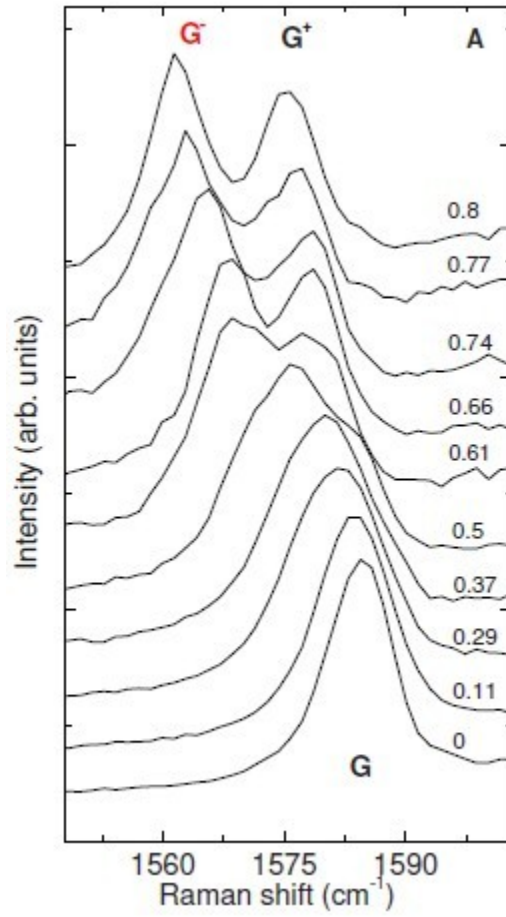


Figure 6.3 G peak as a function of uniaxial strain

(T.M.G Mohiuddin et al⁶¹)

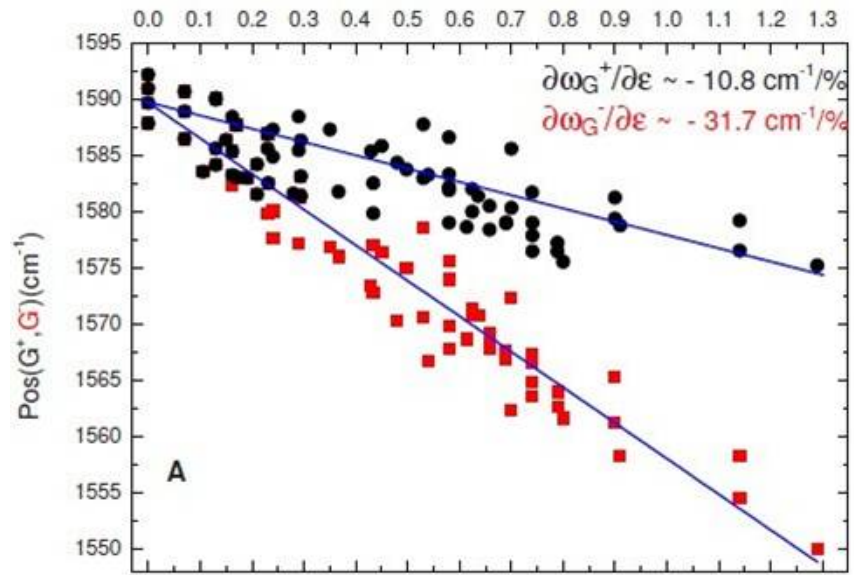


Figure 6.4 Positions of G^+ and G^- in experiment
(T.M.G Mohiuddin et al)

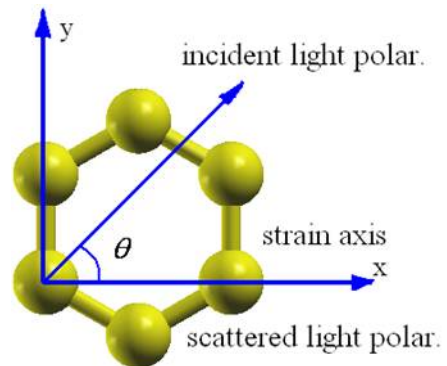


Figure 6.5 Directions of incident scattered light and strain

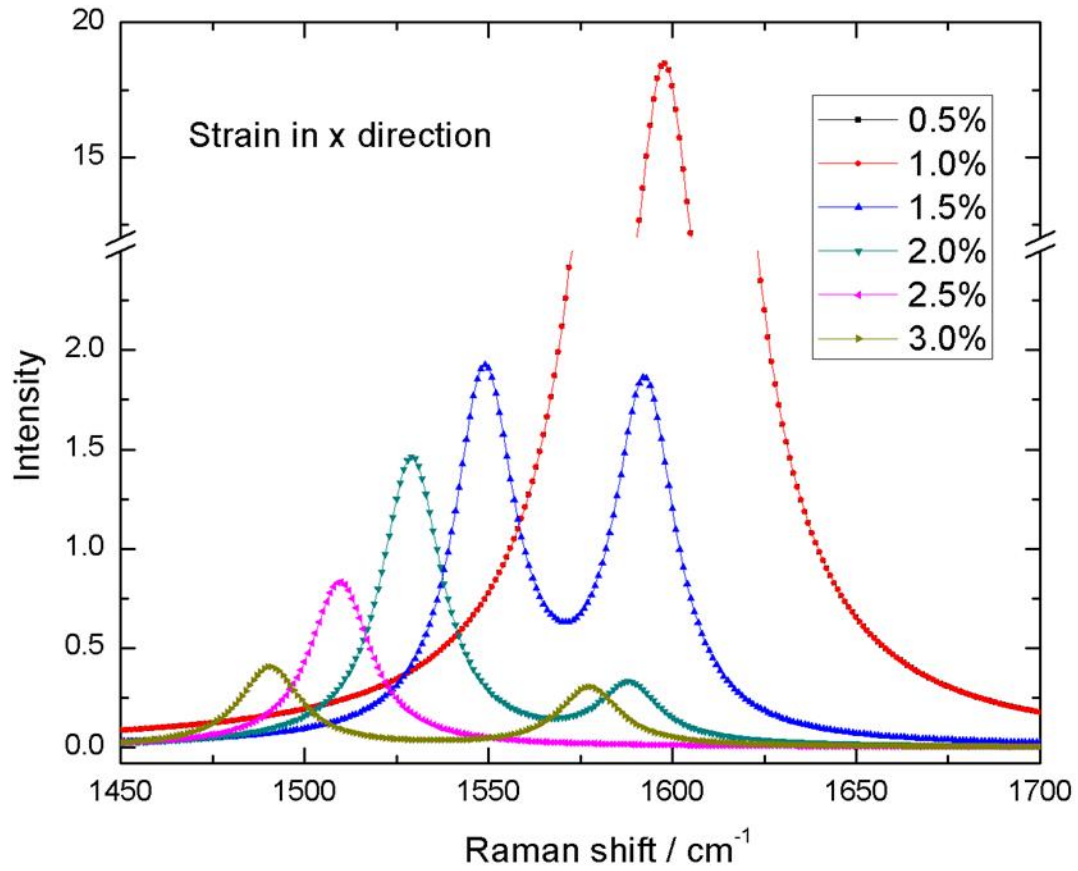
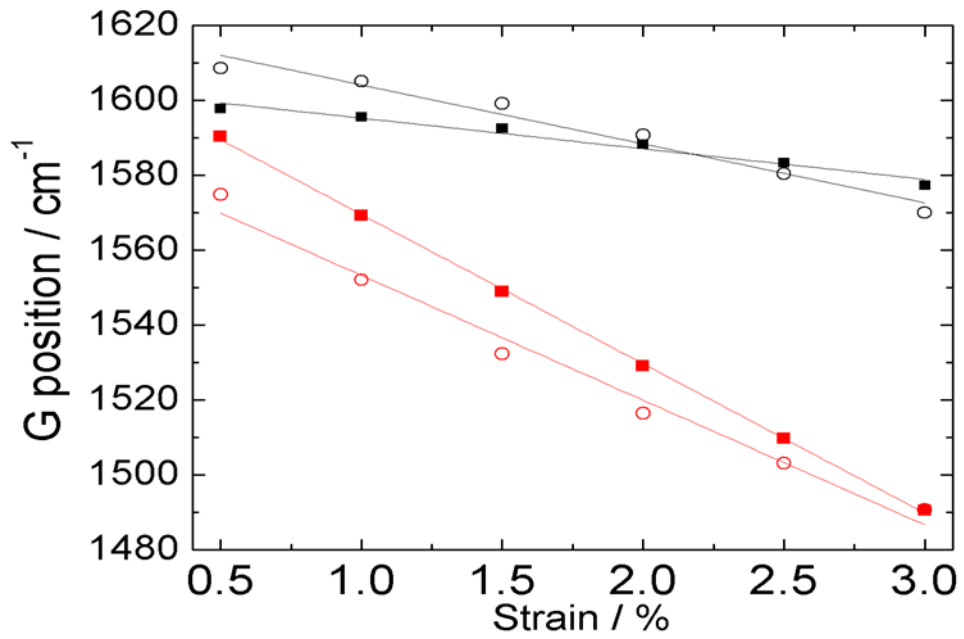


Figure 6.6 G peak as a function of uniaxial strain for monolayer freestanding graphene



■ $\partial\omega G_x^+ / \partial\varepsilon \sim -8.17\text{cm}^{-1} / \%$

○ $\partial\omega G_y^+ / \partial\varepsilon \sim -15.75\text{cm}^{-1} / \%$

■ $\partial\omega G_x^- / \partial\varepsilon \sim -39.88\text{cm}^{-1} / \%$

○ $\partial\omega G_y^- / \partial\varepsilon \sim -33.32\text{cm}^{-1} / \%$

Figure 6.7 Positions of G+ and G- and linear fitting

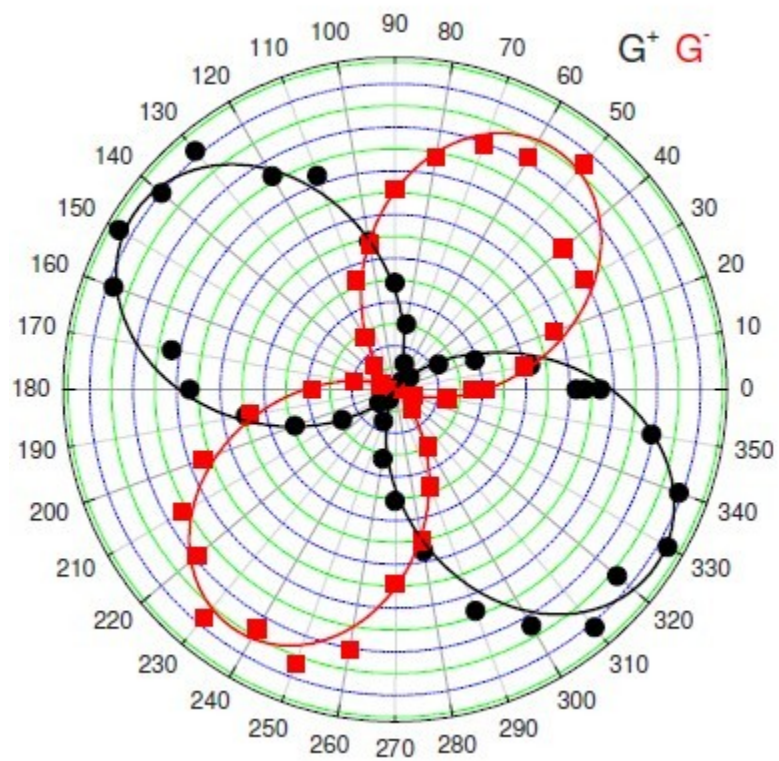


Figure 6.8 Polarization dependence of G peak in experiment

(T.M.G Mohiuddin et al)

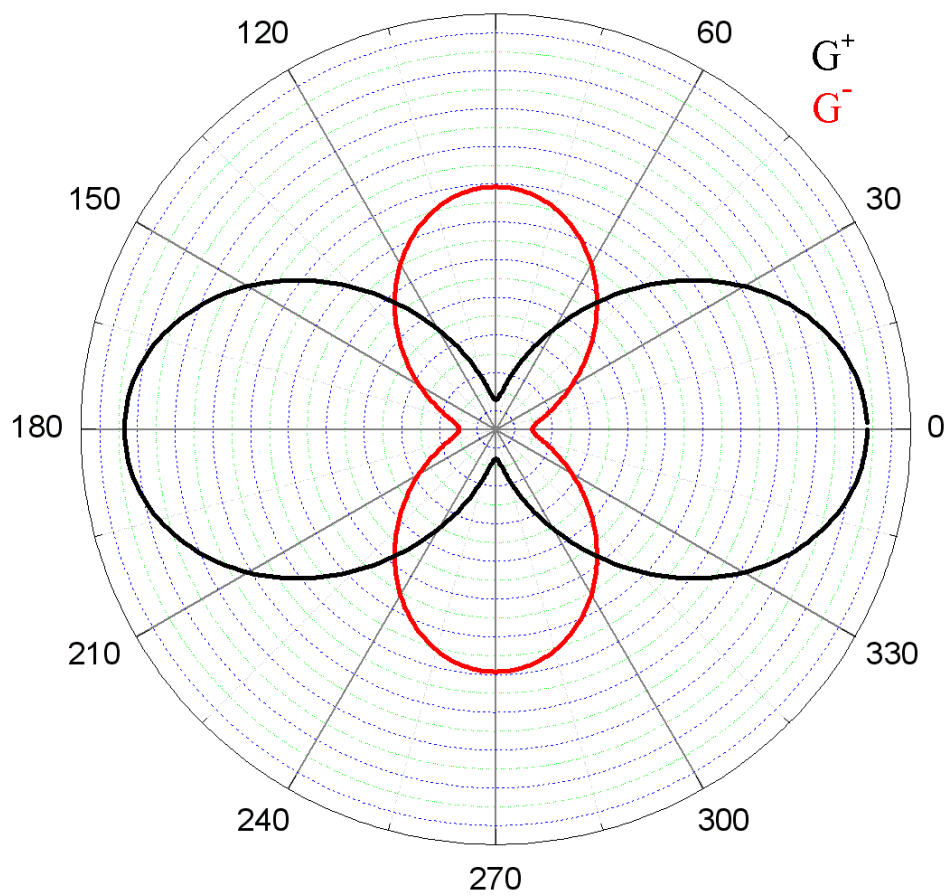


Figure 6.9 Polarization dependence of G peak from first-principles calculation

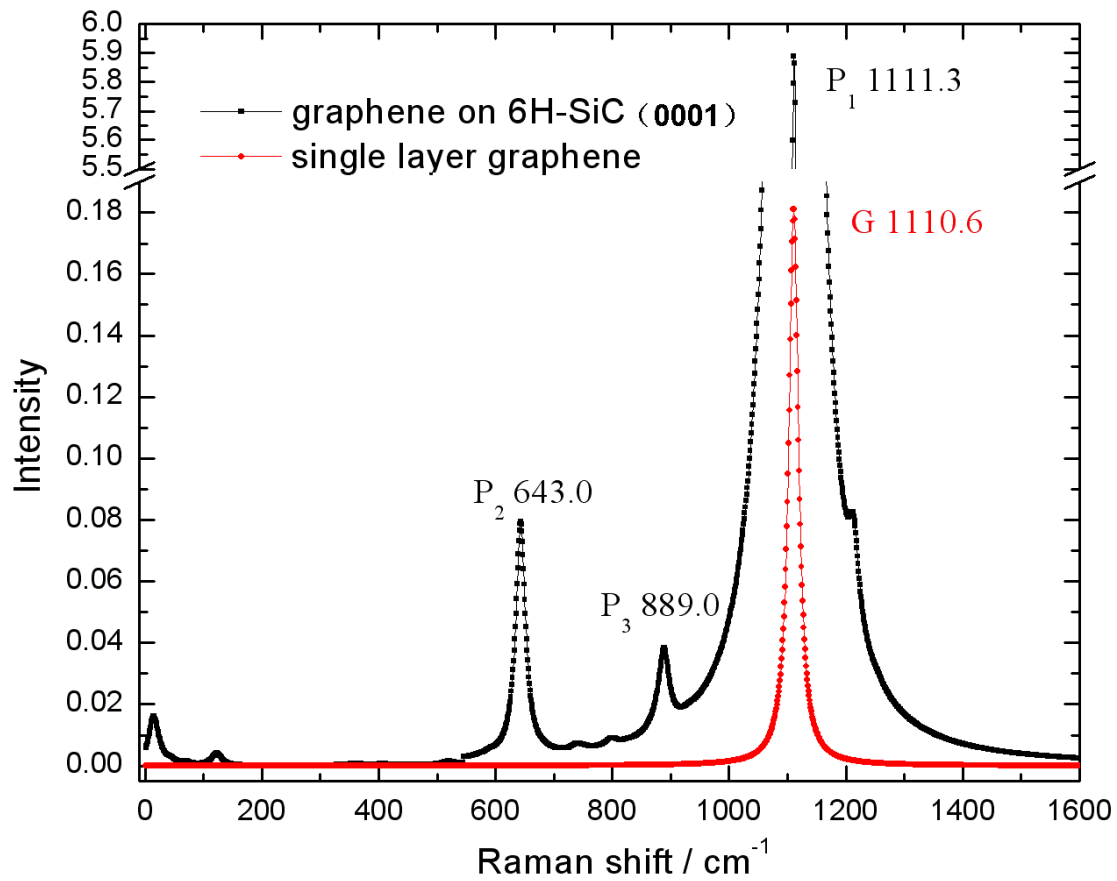


Figure 6.10 Raman spectrum of graphene on Si face 6H-SiC

REFERENCES

- ¹ Spindler, Meyer, and Meerburg, *Annalen der Physik*.
- ² Hohenberg and Kohn, "Inhomogeneous Electron Gas."
- ³ Kohn and Sham, "Self-Consistent Equations Including Exchange and Correlation Effects."
- ⁴ Giannozzi et al., "QUANTUM ESPRESSO."
- ⁵ Castro Neto et al., "The Electronic Properties of Graphene."
- ⁶ Feynman, "Forces in Molecules."
- ⁷ Baroni, de Gironcoli, and Dal Corso, "Phonons and Related Crystal Properties from Density-functional Perturbation Theory."
- ⁸ Bruesch, *Phonons*.
- ⁹ Lazzeri and Mauri, "First-Principles Calculation of Vibrational Raman Spectra in Large Systems."
- ¹⁰ Wallace, "The Band Theory of Graphite."
- ¹¹ Castro Neto et al., "The Electronic Properties of Graphene."
- ¹² Novoselov et al., "Electric field effect in atomically thin carbon films."
- ¹³ Berger et al., "Ultrathin epitaxial graphite."
- ¹⁴ Obraztsov et al., "Chemical vapor deposition of thin graphite films of nanometer thickness."

¹⁵ Gierz et al., “Atomic Hole Doping of Graphene.”

Aristov et al., “Graphene Synthesis on Cubic SiC/Si Wafers. Perspectives for Mass Production of Graphene-Based Electronic Devices.”

¹⁶ Ouerghi et al., “Sharp Interface in Epitaxial Graphene Layers on 3C-SiC(100)/Si(100) Wafers.”

¹⁷ Aristov et al., “Graphene Synthesis on Cubic SiC/Si Wafers. Perspectives for Mass Production of Graphene-Based Electronic Devices.”

¹⁸ Ibid.

¹⁹ Varchon et al., “Electronic Structure of Epitaxial Graphene Layers on SiC.”

²⁰ Ouerghi et al., “Sharp Interface in Epitaxial Graphene Layers on 3C-SiC(100)/Si(100) Wafers.”

²¹ Latil, Meunier, and Henrard, “Massless Fermions in Multilayer Graphitic Systems with Misoriented Layers.”

²² Giannozzi et al., “QUANTUM ESPRESSO.”

²³ Aristov et al., “Graphene Synthesis on Cubic SiC/Si Wafers. Perspectives for Mass Production of Graphene-Based Electronic Devices.”

²⁴ Varchon et al., “Electronic Structure of Epitaxial Graphene Layers on SiC.”

²⁵ Jayasekera et al., “Electronic Properties of the graphene/6H-SiC(0001)[over $\bar{1}$] Interface.”

²⁶ Ouerghi et al., “Sharp Interface in Epitaxial Graphene Layers on 3C-SiC(100)/Si(100)

Wafers”; Aristov et al., “Graphene Synthesis on Cubic SiC/Si Wafers. Perspectives for Mass Production of Graphene-Based Electronic Devices.”

²⁷ Ouerghi et al., “Sharp Interface in Epitaxial Graphene Layers on 3C-SiC(100)/Si(100) Wafers.”

²⁸ Aristov et al., “Graphene Synthesis on Cubic SiC/Si Wafers. Perspectives for Mass Production of Graphene-Based Electronic Devices.”

²⁹ Bermudez and Kaplan, “Preparation and Characterization of Carbon-terminated β -SiC (001) Surfaces.”

³⁰ Käckel, Furthmüller, and Bechstedt, “Stoichiometry and Surface Reconstructions of (001) Surfaces of Silicon Carbide.”

³¹ Baskin and Meyer, “Lattice Constants of Graphite at Low Temperatures.”

³² Powers et al., “Structural Analysis of the β -SiC (100)-c (2×2) Surface Reconstruction by Automated Tensor Low-energy Electron Diffraction.”

³³ Ouerghi et al., “Sharp Interface in Epitaxial Graphene Layers on 3C-SiC(100)/Si(100) Wafers.”

³⁴ Aristov et al., “Graphene Synthesis on Cubic SiC/Si Wafers. Perspectives for Mass Production of Graphene-Based Electronic Devices.”

³⁵ Ouerghi et al., “Sharp Interface in Epitaxial Graphene Layers on 3C-SiC(100)/Si(100) Wafers.”

- ³⁶ Powers et al., “Structural Analysis of the β -SiC (100)-c (2 \times 2) Surface Reconstruction by Automated Tensor Low-energy Electron Diffraction.”
- ³⁷ Novoselov et al., “Electric field effect in atomically thin carbon films.”
- ³⁸ Moon et al., “Top-Gated Graphene Field-Effect Transistors Using Graphene on Si (111) Wafers.”
- ³⁹ Hackley et al., “Graphitic Carbon Growth on Si(111) Using Solid Source Molecular Beam Epitaxy.”
- ⁴⁰ Duraia, Mansurov, and Tokmoldin, “Formation of Graphene by the Thermal Annealing of a Graphite Layer on Silicon Substrate in Vacuum.”
- ⁴¹ Hackley et al., “Graphitic Carbon Growth on Si(111) Using Solid Source Molecular Beam Epitaxy.”
- ⁴² Takayanagi et al., “Structural Analysis of Si (111)-7 \times 7 by UHV-transmission Electron Diffraction and Microscopy.”
- ⁴³ Varchon et al., “Electronic Structure of Epitaxial Graphene Layers on SiC.”
- ⁴⁴ Jayasekera et al., “Electronic Properties of the graphene/6H-SiC(0001[over $\bar{1}$]) Interface.”
- ⁴⁵ Ortega, Flores, and Yeyati, “Electron Correlation Effects in the Si(111)-7 \times 7 Surface.”
- ⁴⁶ Jayasekera et al., “Electronic Properties of the graphene/6H-SiC(0001[over $\bar{1}$]) Interface.”

⁴⁷ Hackley et al., “Graphitic Carbon Growth on Si(111) Using Solid Source Molecular Beam Epitaxy.”

⁴⁸ Takayanagi et al., “Structural Analysis of Si (111)- 7×7 by UHV-transmission Electron Diffraction and Microscopy.”

⁴⁹ Ortega, Flores, and Yeyati, “Electron Correlation Effects in the Si(111)- 7×7 Surface.”

⁵⁰ Schedin et al., “Detection of Individual Gas Molecules Adsorbed on Graphene.”

⁵¹ Ribeiro et al., “Inducing Energy Gaps in Monolayer and Bilayer Graphene.”

⁵² Wehling, Lichtenstein, and Katsnelson, “First-principles Studies of Water Adsorption on Graphene.”

⁵³ Ribeiro et al., “Inducing Energy Gaps in Monolayer and Bilayer Graphene.”

⁵⁴ Wehling, Lichtenstein, and Katsnelson, “First-principles Studies of Water Adsorption on Graphene.”

Wehling, Lichtenstein, and Katsnelson, “First-principles Studies of Water Adsorption on Graphene.”

⁵⁵ Rubeš et al., “Structure and Stability of the Water–Graphite Complexes.”

⁵⁶ Leenaerts, Partoens, and Peeters, “Adsorption of H₂O, NH₃, CO, NO₂, and NO on Graphene.”

⁵⁷ Ribeiro et al., “Inducing Energy Gaps in Monolayer and Bilayer Graphene.”

⁵⁸ Rubeš et al., “Structure and Stability of the Water–Graphite Complexes.”

⁵⁹ Mohiuddin et al., “Uniaxial Strain in Graphene by Raman Spectroscopy.”

⁶⁰ Huang et al., “Phonon softening and crystallographic orientation of strained graphene studied by Raman spectroscopy.”

⁶¹ Mohiuddin et al., “Uniaxial Strain in Graphene by Raman Spectroscopy.”